Multi-Physics Model of a Dielectric Barrier Discharge Flow Control Actuator with Experimental Support

William C. Schneck, III

Dissertation submitted to the Faculty of the

Virginia Polytechnic Institute and State University

in partial fulfillment of the requirements for the degree of

Doctor of Philosophy

in

Mechanical Engineering

Walter F. O'Brien, Chair

William T. Cousins

Clinton L. Dancy

Danesh K. Tafti

Brian Vick

February 8, 2016

Blacksburg, Virginia

Keywords: Dielectric Barrier Discharge, Boundary Layer Flow Control, Multi-Physics Modeling, Shadowgraphy, Spectroscopy, Relative Line Method

Multi-Physics Model of a Dielectric Barrier Discharge Flow Control Actuator with Experimental Support

William C. Schneck, III

(ABSTRACT)

This dissertation presents an experimentally supported multi-physics model of a dielectric barrier discharge boundary layer flow control actuator. The model is independent of empirical data about the specific behavior of the system. This model contributes to the understanding of the specific mechanisms that enable the actuator to induce flow control.

The multi-physics numerical model couples a fluid model, a chemistry model, and an electrostatics model. The chemistry model has been experimentally validated against known spectroscopic techniques, and the fluid model has been experimentally validated against the time-resolved shadowgraphy. The model demonstrates the capability to replicate emergent flow structures near a wall. These structures contribute to momentum transport that enhance the boundary layer's wall attachment and provide for better flow control.

An experiment was designed to validate the model predictions. The spectroscopic results confirmed the model predictions of an electron temperature of $0.282 eV$ and an electron number density of $65.5 \times 10^{-12} kmol/m^3$ matching to within a relative error of 12.4% and 14.8%, respectively. The shadowgraphic results also confirmed the model predicted velocities of flow structures of $3.75 m/s$ with a relative error of 10.9%. The distribution of results from both experimental and model velocity calculations strongly overlap each other.

This validated model provides new and useful information on the effect of Dielectric Barrier Discharge actuators on flow control and performance.

Contents

List of Figures

x

List of Tables

Nomenclature

μ Dynamic viscosity

q Electron charge

k_B Boltzmann constant

m_e Electron mass

ϵ_0 Permittivity of free space

$\epsilon_{dielectric}$ Permittivity of dielectric barrier

$\vec{\vec{I}}$ Identity matrix

x Streamwise coordinate

y Wall normal coordinate

$\vec{x}$ Position vector

ΔL Spatial grid discretization for numerical model

t Time

τ Pulse cycle time

Δt Time discretization for numerical model

D Cylinder diameter

L_x Streamwise length of computational domain

δ infinitesimal deviation in space

u Streamwise velocity component. Compass direction subscripts indicate control volume face values

v Wall normal velocity component. Compass direction subscripts indicate control volume face values

$\vec{v}$ Gas velocity vector

U_∞ Upstream bulk flow speed

Δu Cross-correlation streamwise velocity uncertainty

Δv Cross-correlation wall normal velocity uncertainty

Δn_x Streamwise pixel shift detected by cross-correlation

$\sigma_{\Delta n_x}$ Standard deviation of streamwise pixel shift of accepted cross-correlation peaks

Δn_y Wall normal pixel shift detected by cross-correlation

$\sigma_{\Delta n_y}$ Standard deviation of wall normal pixel shift of accepted cross-correlation peaks

σ_x Standard deviation of streamwise pixel shift detected by cross-correlation

σ_y Standard deviation of wall normal pixel shift detected by cross-correlation

F_s High speed camera frame rate

ΔF_s Frame rate uncertainty

D_{refl} Diameter of the secondary reflector holder

ΔD_{refl} Secondary reflector holder diameter uncertainty

N_{refl} Pixel count across secondary reflector

ΔN_{refl} Secondary reflector pixel count uncertainty

N_{valid} Count of accepted cross-correlation peaks of shadowgraph frames

$N_{samples}$ Number of cross-correlations performed for velocity population

N_{sep} Time step separation count for model cross-correlation

Re Reynold's number

T_{gas} Gas static (thermodynamic) temperature

ρ Gas mass density

e Internal energy

P Static (thermodynamic) pressure

P_e Electron pressure

P_{Ar} Partial pressure of argon

P_{Ar^+} Partial pressure of argon cation

ψ Arbitrary property

$\tau_{x,x}, \tau_{x,y}, \tau_{y,x}, \tau_{y,y}$ Components of the fluid shear stress tensor

$\vec{\vec{\tau}}$ Fluid shear stress tensor

$\vec{f_b}$ Body force on fluid (force/volume)

V Applied voltage

ϕ Electric potential

E_x Streamwise electric field vector component

E_y Wall normal electric field vector component

$\vec{E}$ Electric field vector

$dx_{\hat{E}}$ Differential position vector component parallel to electric field vector

λ_D Debye length

f_{th} Thermalized fraction of energy input

η Plasma impedence

J Current density

n_k Number density of species indexed by 'k'

$n_{[X]}$ Number density of species 'X'(where 'X' can be e.g. N_2 etc.

n_k^{rxn} Number density of species 'k' after reaction chemistry integration over a time step

n_{cation} Total number density of positively charged ionic species

n_{anion} Total number density of negatively charged ionic species

n_{Heavy} Total number density of all species except electrons

χ Mole fraction. Subscripts denote of which species

MW_k Molar weight of species 'k'

$\Delta \bar{e}_{f_k}^0$ Internal energy of formation for species 'k'

$\bar{c}_{v_k}$ Specific heat at constant volume for species 'k' (energy/(temperature-volume))

T_{ref} Reference temperature for tabulated values

$k_{[X]}$ Reaction rate coefficient for mechanism indexed by 'X'

rr_k Total reaction rate for species 'k'

IE_a First ionization energy of argon

T_e Electron temperature

$\vec{v}_e$ Electron velocity

ν_{coll} Electron-heavy species collision frequency

$\langle\sigma_{Heavy}\rangle$ Electron-heavy species collision cross section

I_λ Photon emission density ($\frac{\gamma}{\lambda}$)

λ Wavelength

A Transition probability. Subscripts denote information about the electronic transition

k_{exc} Electron impact excitation rate coefficient of diatomic nitrogen

$k_{N_{2(C)}}^{O_2}$ Diatomic oxygen impact de-excitation of diatomic nitrogen in the $N_{2(C)}$ excited state

$f_v\left(E, T_e\right)$ Electron energy distribution

E Electron energy for integration over energy distribution

$\sigma_{exc}\left(E\right)$ Electron impact excitation cross-section for diatomic nitrogen

E_1 Photon energy emitted by transition from line 1 in relative line spectrum calculations

E_2 Photon energy emitted by transition from line 2 in relative line spectrum calculations

$\frac{I_2}{I_1}$ Ratio of line intensities for relative line spectrum calculations

$\frac{A_1}{A_2}$ Ratio of transition probabilities for relative line spectrum calculations

$\boldsymbol{f}$ Arbitrary process

$\mathcal{F}$ Solution 'rule' for arbitrary process '$\boldsymbol{f}$'

ω	Model under-relaxation value
i	Streamwise grid coordinate index $i = 1, 2, ...I$
j	Wall normal grid coordinate index
k	Species index
m	Alternate species index
p	Index of set of arbitrary processes $p = 1, 2, ...P$
l	Index of time steps for arbitrary processes from time $l = 1, 2, ...L$
$*$	Evaluation of property value as predictor
t	Evaluation of property value at time 't'
$t+1$	Evaluation of property value at time 't' plus one time step
N	Atomic nitrogen
N^+	Nitrogen cation
N_2	Diatomic nitrogen. Additional subscripts indicates excited states and transitions
O	Atomic oxygen
O^+	Oxygen cation
O_2	Diatomic oxygen
O_2^+	Diatomic oxygen cation
Ar	Argon
Ar^+	Argon cation
e^-	Electron

Chapter 1

Introduction

This work is an exploration of the fundamental physics of dielectric barrier discharge flow control. This dissertation covers the development of a first-principles multi-physics model and the validation of this model against experimental data. This introduction will briefly cover the motivations for the work presented, a brief description of the operational principles, the major objectives, the previous work done in the applicable fields, and a summary of the current work.

1.1 Motivation

Within boundary flows a wide variety of speeds, temperatures, and flow conditions exist. These can all be usefully influenced by some form of applied flow control. Possible applications include: low pressure turbines with low Reynolds Numbers, combustor flame control, blade tip leakage, inlets, interturbine ducts, nacelles, nozzles, and vanes. Similarly, further flow control opportunities may exist within other gas flows. Indeed, anywhere boundary layer losses exist, effective flow control reduces these losses [26].

Plasma-based methods are one means of achieving active flow control. A promising type
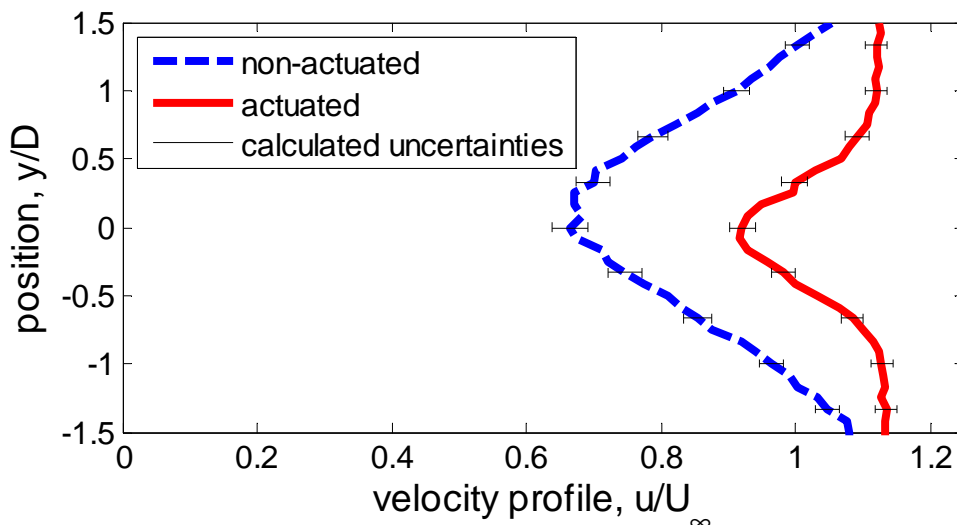
Figure 1: Cylinder wake control [13]

of actuator utilizes a pulsed high voltage DC Dielectric Barrier Discharge (DBD) actuator to create a plasma for control. This actuator generates vorticity which enhances transport of momentum from the free-stream to the boundary layer, thus re-energizing the boundary layer. Previous work ([13, 34, 42, 5, 29, 2, 17, 41] among others) shows experimentally that the technology is promising. An example shown in Figure 1[13], is the aggregate effect on the wake of a right circular cylinder. For a comprehensive discussion by the author of this dissertation of these results shown in Figure 1, see Appendix B.

Applications for flow control exist across a wide range of Reynolds Numbers and Mach Numbers. Current developments in dielectric barrier discharge flow control actuators largely focus on lower values of these, however, efforts to develop the technologies are ongoing throughout the potential application space. Applications of flow control to inlet systems require the actuator to provide sufficient effect to adjust flow at speeds in the middle to high subsonic range. Supersonic inlet control will require sufficient characteristic frequencies to significantly eclipse the flow characteristic frequencies. Flow control within an engine will require a fundamental understanding of the actuator in conditions that can be difficult to replicate or instrument in a laboratory. In order to expand into these and other more difficult flow

domains, many enabling technologies will require further development. One enabling technology will be lightweight, very high frequency power supplies. Further, improved modeling (both high accuracy models and fast, simple models) of the actuators will be required to conduct design studies within these environments.

The motivation for the current work is to develop a first principles understanding of the fluid system. The transient model presented here solves the fluid mechanics along with the electric field and chemical kinetics to provide a deeper physical understanding of what happens within the discharge over the entirety of the pulse cycle. These physical observations and computationally resolved data can be used to improve understanding, and to provide design and implementation guidance.

1.2   Benefits and Principles of Ion Flow Control

Fundamentally, plasma control methods create locally ionized gas that can be manipulated electromagnetically to induce changes in flow conditions. A significant advantage of plasma flow control devices is that they contain no moving parts. This makes mechanical failure highly unlikely. Additionally, unlike methods such as vortex generators, these actuators are flush with the flow surface, and thus avoid the significant increase in skin friction losses associated with flow protrusions. Further, they are active systems, and can be deactivated when their use is not advantageous, thus reducing power consumption. Finally, the actuators themselves are lightweight. Any significant weight growth comes from power supply requirements.

The flow control actuator studied in this work is the dielectric barrier discharge flow control actuator. Fundamentally, it consists of a flush mounted electrode exposed to the flow, with a second electrode embedded within the wall downstream of the flush mounted electrode. The material separating these electrodes needs to be a strong dielectric. This architecture is illustrated in the schematic shown in Figure 2. Conceptually, this makes the actuator appear
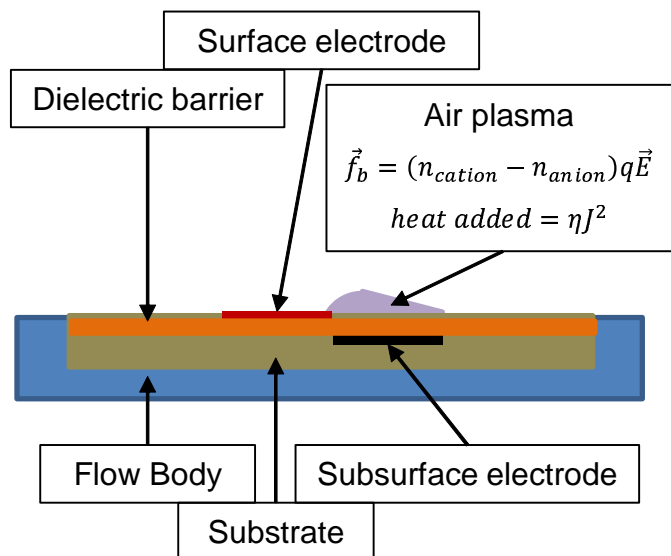
Figure 2: Schematic depiction of the major components of a DBD actuator.

somewhat like a capacitor. This means, to avoid destruction of the dielectric material, a transient voltage must be applied to get current to flow, with a net time averaged electron flux of zero. With a high enough peak voltage, the air will begin to ionize without causing breakdown of the dielectric. Upon ionization, forces can be applied to the ionized region of the flow due to the presence of charged particles in an electric field shown in Equation 1.1 and the gas can be heated due to current flow resulting in resistive power dissipation. These actions can be used to affect the ionized region (shown schematically in purple in Figure 2) to enhance boundary layer attachment.

$$\vec{f_b} = (n_{cation} - n_{anion})\, q\vec{E} \tag{1.1}$$

Research challenges to be addressed by plasma flow control research include that a plasma flow control actuator requires electrical power. Thus, the systems level improvements caused by the actuator must outweigh the costs of the implementation of the actuator and its power supply. Additionally, there are multiple failure modes that challenge reliability, such as dielectric breakdown, power supply failure, or electrode corrosion and erosion. Further,

there may be significant electromagnetic issues if the actuators are used extensively in an unshielded system. This could interfere with other nearby electrical systems. Finally, the power supply brings with it weight growth, especially if the platform lacks a high capacity high voltage power system.

A further research challenge includes locally increased material stresses near the wall, as pressure and shear stress can both be increased due to the increased turbulence of the near-wall gas. Thus, for any flow control technology, balancing the strength of the actuator with potentially degraded part life will be an important trade space to consider. This balance could be addressed by reduced peak actuator voltages and currents, improved materials selection, or any number of possible architectural adjustments that mitigate the wall stresses while permitting more actuator strength.

1.3 Previous Research

Plasma flow control techniques have been actively studied in many flow regimes and situations. These include potential applications in struts, airfoils, inlets, and various low Reynolds number flows [34, 15, 42].

1.3.1 Actuator Types

One type of plasma actuator utilizes surface mounted electrodes to achieve an "ion wind" type actuation. Studies of such actuators have been undertaken by several authors focused mostly on flat plate architectures [39, 35, 21, 22]. These actuators utilize a high voltage DC corona to produce changes in the boundary layer through a body force acting on the momentum of the flow. These have claims of a larger effective region; however, they have demonstrated sensitivity to ambient conditions and to the quality of manufacture.

Another type of plasma actuator utilizes a dielectric barrier discharge (DBD) actuator excited

with a high frequency and high voltage AC power source. These utilize voltages frequently on the order of $10kV$ and frequencies on the order of $10kHz$. Many of these have been modeled through body force terms in the momentum equation as well [20]. They have been studied on many geometries, but have typically been applied at rather low speeds ($U_\infty < 12m/s$) on cylinders [28], and higher speeds ($U_\infty = 30m/s$) on airfoils [2].

A similar type of actuator to the AC-DBD is a DBD actuator that uses a pulsed high voltage DC power supply. These use pulse widths on the order of 10 to 100 ns [38], utilizing pulse frequencies from 100Hz-10kHz [17]. It has been proposed that the physical mechanism, instead of coupling through the momentum of the flow, couples through a propagating pressure wave due to local rapid heating near the actuator [38]. Results on the wake have been demonstrated on cylinders at $Re = 15000$, with a speed $U_\infty = 4.6m/s$ [17]. Further, pulse frequencies near the shedding frequency have been shown to lock in the shedding frequency on to the pulse frequency and increase drag [17]. Bow shock control has been demonstrated with remarkable success [31]. Reattachment using this method has further been demonstrated on airfoils with $U_\infty = 93m/s$ [34]. Further, quiescent studies regarding the induced flow by both AC-DBD and pulsed-DBD actuators have been undertaken [38, 5].

1.3.2   Actuator Modelling

Many plasma actuator models including CFD models exist ([20, 29]). However, these frequently rely on either empirical adjustments or bulk estimates within the plasma. Some higher fidelity models [23] extensively cover the physics of the discharge. However, these models cover limited chemistry with short time windows relative to flow behavior. Some models [36] use similarly limited mechanisms but do solve over the full pulse duration. Other models treat the air as a multi-fluid model ([24, 25], among others) with particle conversion between them, but do not account for speciation. The modelling technique presented in the current work addresses these limitations.

1.3.3 Plasma Diagnostics

Plasma spectroscopy is a means of determining the properties of a plasma by the nature of the emitted light. The emissions result from electron energy transitions, which can be between a free-state and a bound-state, a free-state to another free-state, or within an atom or molecule from a bound-state to another bound-state. These transitions have characteristic wavelengths that manifest themselves as peaks on spectrographs. The relative heights and widths of these peaks provide the relevant information about the plasma [27, 7, 8]. In air, electron number densities can be found by their effect on the emission of the $N_{2(C-B,0-0)}$ emission line in the N_2 second positive spectrum [30]. The electrons contribute to the excitation of the $N_{2(C,0)}$ state, and so by knowing the photon emission rate in this wavelength band, the electron number density can be estimated.

1.4 Objectives

The objectives of this work are to:

- Develop a first-principles numerical model of a dielectric barrier discharge plasma actuator

- Experimentally validate the above model in channel flow

- Use results obtained from the validated model to explore and better understand the governing physics and emergent behaviors of dielectric barrier discharge plasma actuators

1.5 Summary of the Current Work

The current work is organized into 9 chapters. Chapters 1 and 2 cover introductory material and a broad overview of the science. Chapters 3 and 4 discuss the development of the relevant physics, and the creation of the numerical model. Chapter 5 covers the model results. Chapter 6 covers the experimental setup. Chapter 7 cover the results of the experiments. Chapter 8 covers the comparison of the numerical results with the experimental data along with a discussion of the model results. Finally, Chapter 9 discusses the conclusions of the work and recommended follow-on efforts.

Chapter 2

Overview of Research

As stated, the main objective of this research is to create a first-principles model of a Dielectric Barrier Discharge (DBD) flow control actuator. A validated first-principles model provides greater insight into the physical mechanisms of a system, more so than a wholly or partially empirical model. This is due to the estimation that is necessary within the experimental frameworks that generate most most empirical and semi-empirical models models. A first-principles model allows the user to interrogate the physical system inside regions that are frequently obscured by the empirical relationships that govern empirical and semi-empirical models models. This finer resolution of the physics involved permits the user to take a more nuanced look at the physics, and this, in turn, may lead to further improvements to the relevant technology.

2.1   The Physical System

The focus of the work is on the DBD actuator in air. The flow control arises from the application of an electric field to produce fractionally ionized air. This air discharge is subject to energy input and speciation. The subsequent increase in temperature and number density
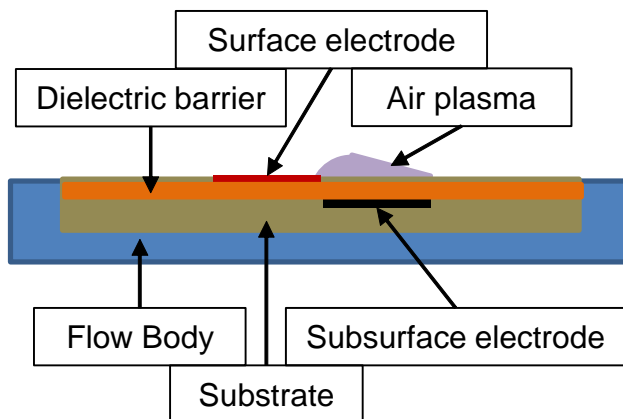
Figure 3: Schematic depiction of the major components of a DBD actuator.

(given by Equation 2.1) creates an increase in pressure. The fluid is also subject to body forces due to the presence of electric fields and charged particles as shown in Equation 2.2. Figure 3 shows the common schematic design of these actuators. This schematic shows the major components of this common design. Commonly, the dielectric barrier is combined with the substrate (and sometimes the flow body itself) into one piece. The electrodes are connected to the high voltage power supply to provide the energy to the air discharge.

$$e^- + N_2 \rightarrow 2e^- + N^+ + N \tag{2.1}$$

$$\vec{f_b} = (n_{cation} - n_{anion})q\vec{E} \tag{2.2}$$

This work models a 2-D channel flow system with uniform inlet conditions and a DBD actuator centered at the midpoint on one wall. This case study allows the investigation of the effect of the actuator on an established boundary layer. A schematic of this physical arrangement can be seen in Figure 4. The velocities are kept low ($u < 10m/s$) to minimize turbulent effects, as they are not modeled within the numerical model presented here.
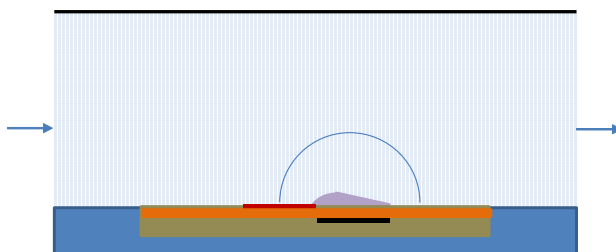
Figure 4: Schematic depiction of the channel flow with a DBD actuator.

2.2 The Modeling Method

The numerical model is a computational approximation of this multi-physics problem. There are three major parts that need to be solved simultaneously: the electric field, the chemical kinetics, and the fluid transport. These will be addressed in turn.

2.2.1 Electric Field

The electric field was modeled quasi-electrostatically. This was deemed acceptable because the current flow rates are relatively low, and as such, the magnetic effects should be small. From here, the electrostatics are comparatively easy to solve given a charge distribution (as a result of the chemical kinetics) and boundary conditions.

2.2.2 Chemical Kinetics

The chemistry of the gas discharge is fundamental to any plasma based flow control. Through the generation of ions, body forces can be applied. Through speciation, larger molecules can be broken down into multiple smaller molecules and atoms, contributing to raising the pressure. Unfortunately, chemical kinetics is a difficult problem to solve. It is modeled as an extensive set of coupled first order differential equations in time, and because these are stiff equations, they must be handled with some care. Discussion of the algorithm used to solve these while preserving physicality follows in Chapter 4.

2.2.3 Transport

Since the objective is to describe physically how a DBD actuator achieves flow control, fluid transport results are necessary. To achieve this, a code was developed to calculate the transport of species and momentum. Due to the multi-physics nature of the problem and associated increase in computational expense, the fluid convective derivatives were constructed as first-order upwinding terms. This code shows the expected effects from the combination of chemistry and electrical forces on the fluid. The field data generated by this code can be used to assess the physical behavior of the device.

2.2.4 Modified Cellular Automata

Modified Cellular Automata is a means of breaking up large, difficult to solve multi-physics models into smaller, more easily solved elements [40]. Modified Cellular Automata is the multi-physics framework selected to combine the three above-mentioned solvers. It works by feeding the results from each model into the next and solving iteratively through small time steps. This advancement method is shown schematically in Figure 5[12]. This framework allows each model to be solved using techniques appropriate to the specific physics at hand, rather than trying to create one solver that handles all of the physics at once. The mathematics of this method proceed in a piecewise fashion. Consequently, the advancing steps (in this case time) must be short enough so that the changes that are occurring in the other physics are small enough to treat as constant over the course of the time step.

2.3 The Experimental Validation

The computational domain was designed to be as simple as possible to facilitate replication in a set of real experiments for validation. A well controlled, yet instrument accessible system is necessary. Two sets of measurements were taken using shadowgraphy and spectroscopy. The
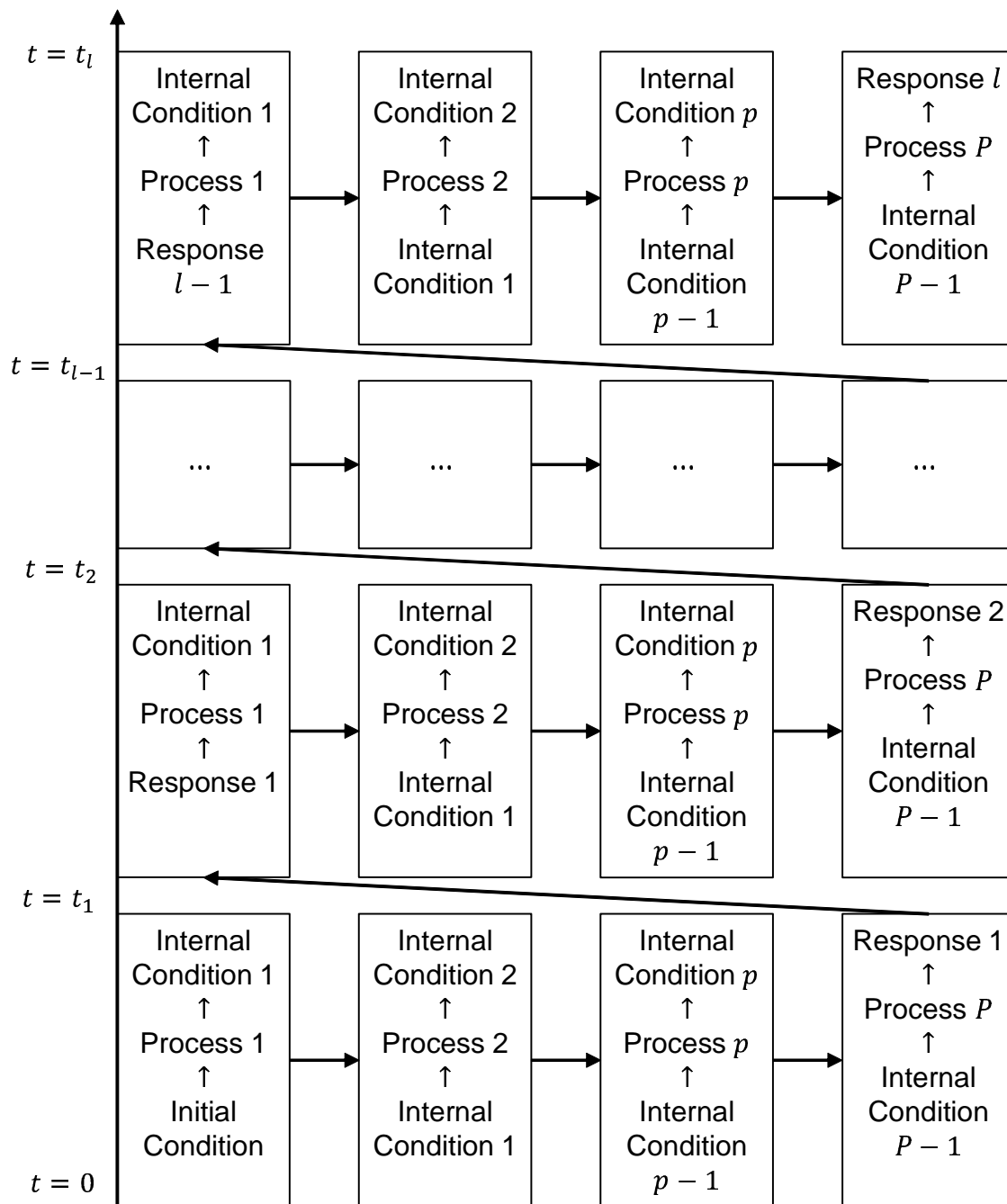
Figure 5: Flowchart depicting the computational process of the modified cellular automata technique.[12]

shadowgraphy measured the motion of large fluid structures, and the spectroscopy measured the electron temperature and number density. The experimental apparatus was designed to maximize transparency to facilitate the taking of spectroscopic and shadowgraphic measurements.

The shadowgraph images will provide validation data regarding the motion of flow structures within the measurement domain. The tracking of these flow structures is done with two dimensional cross-correlations between two time-adjacent frames. This will grant reasonable validation of the transport of flow structures. The process is illustrated in the schematic shown in Figure 6. The image shift computed by the cross correlation between two frames can be converted to a velocity by scaling by pixel size and frame rate.

The spectroscopy gave time-averaged data regarding electron temperature and species number densities, allowing validation of the chemistry. This work compares the electron temperature and number densities from the spectroscopic results with the model results.

The electron temperature is calculated using the relative line method [27] using Equation 2.3. The relative line method utilizes the intensity ratio ($\frac{I_2}{I_1}$) associated with two spectral lines from the same species along with the energies (E_1 and E_2), and the transition probabilities (A) in s^{-1} of the emitted line.

$$T_e = \frac{E_1 - E_2}{\ln\left(\frac{I_2 A_1}{I_1 A_2}\right)} \tag{2.3}$$

The electron number density can be computed from the integrated photon intensity of the $N_{2(C-B,0-0)}$ transition in Equation 2.4 [30]. The transition probabilities, A, can be found from [1], and the number densities of molecular nitrogen and oxygen are computed using an ideal gas equation of state using mole fractions from the 1976 U.S. Standard Atmosphere [6]. The excitation rate coefficient, k_{exc}, can also be found in [30], and is related in Equation 2.5. The excitation cross section, σ_{exc}, can be found in [11], q and m_e are the electron charge and mass respectively, and $f_v (E, T_e)$ is the electron energy distribution function, and for low

14

Raw Image
Schematic

Sub-frame
Extraction

Background
Subtraction

time 1

Secondary
mirror holder

Background
effects

Observed
flow structure

Compute cross-correlated
image shift between two
of these frames to detect
motion of structure

time 2

Flow Direction
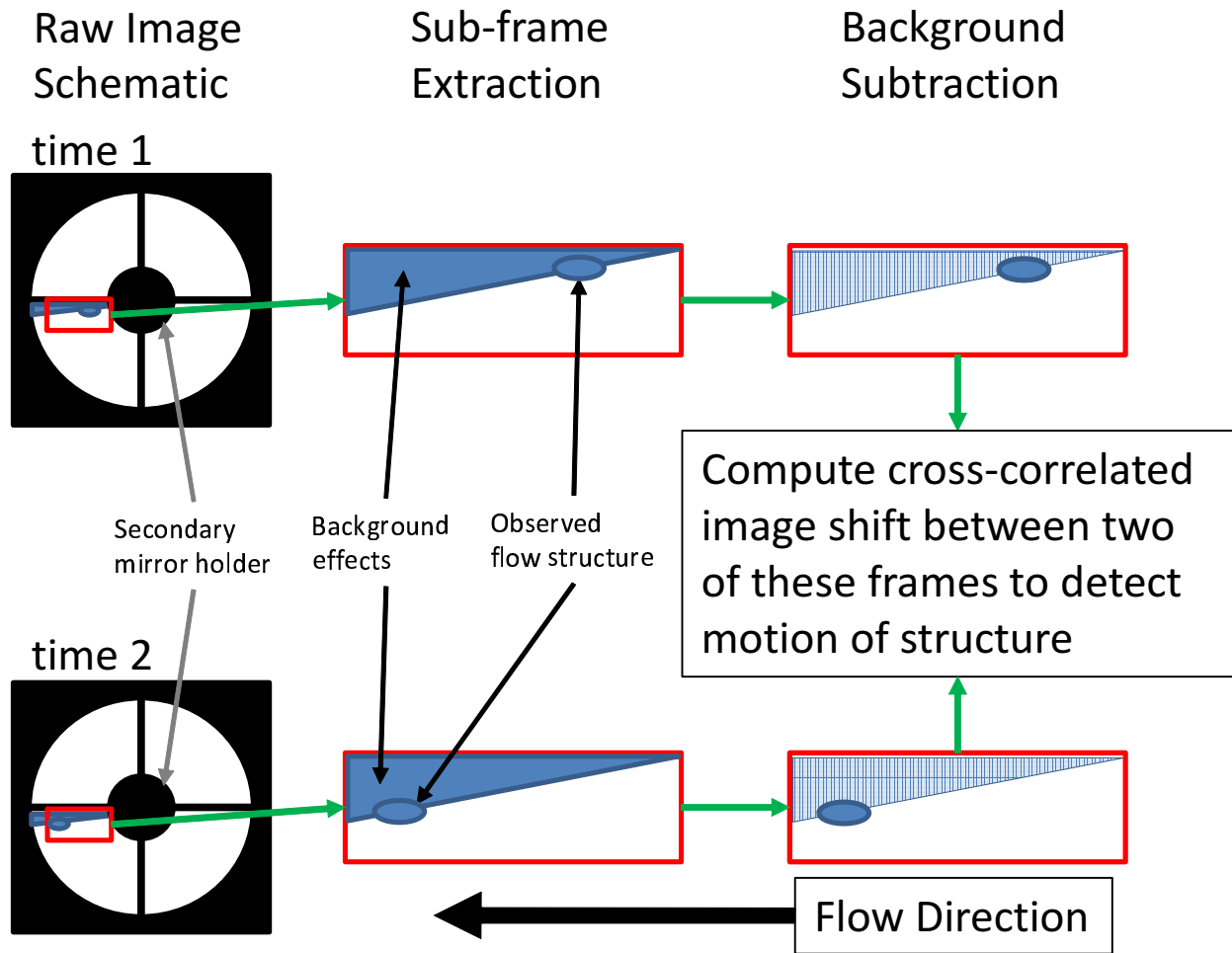
Figure 6: Schematic showing the processing methodology of the shadowgraph results

electron temperatures $(T_e < 1eV)$ is approximated to be Maxwellian.

$$\int\limits_{bandwidth} I_\lambda d\lambda = n_{N_2} n_e k_{exc} \frac{A_{N_2(C-B,0-0)}}{A_{N_2(C-B,0)} + k^{O_2}_{N_2(C)} n_{O_2}} \tag{2.4}$$

$$k_{exc} = 4 * \pi * \sqrt{2} \int\limits_E f_v(E, T_e) \sqrt{\frac{2q}{m_e}} E \sigma_{exc}(E) dE \tag{2.5}$$

Chapter 3

Mathematical Formulation

This chapter covers the mathematical formulation of the physical problem modeled in this work. Included in this are the boundary and initial conditions applied to the model.

3.1   Electric Field

The electric field imposed by the electrodes is the physical cause of the change in the nature of the flow. This section presents how it is modeled to create and interact with the discharge.

3.1.1   Electrostatics

The solution for any electric field is always bound by Gauss' Law (seen in Equation 3.1). To simplify this equation, if one assumes that the current flows are comparatively small [4], magnetic effects and thus, transient effects are negligible in the calculation of the electric field. This allows the model to use the concept of electrostatic potential, which is related to the electric field through Equation 3.2. This can then be substituted into Gauss' Law, resulting in the numerically convenient form of the Poisson equation, shown in Equation 3.3.

$$\nabla \bullet \vec{E} = \frac{q}{\epsilon_0} \left(n_{cation} - n_{anion} - n_e \right) \tag{3.1}$$

$$\vec{E} = -\nabla \phi \tag{3.2}$$

$$\nabla^2 \phi = -\frac{q}{\epsilon_0} \left(n_{cation} - n_{anion} - n_e \right) \tag{3.3}$$

3.1.2 Debye Screening

The Poisson equation (Equation 3.3) requires a modification to the right hand side as the plasma itself is quasi-neutral, meaning that the number of positive charges is equal to the number of negative charges. That said, on very small scales within the discharge, charge separation causes the local electric field to be significantly reduced. The implication of this "screening" is that within the discharge, the electric field cannot drive the interactions with the fluid nearly as strongly.

To avoid having to solve the Poisson equation on a scale that would track individual particles, an approximate distribution of particles is computed to handle the small scale charge separations. The characteristic length that is arrived at is called the Debye length. Note that Debye screening will indicate the maximum amount of screening that the charge distribution can create and that it is a useful quantity to provide a high bound on the reduced effectiveness of the actuator as caused by charge screening. Also of note is that the derivation here of the electron distribution is an approximate solution using local values. Note that in the macro-scale discharge, the distribution of charges is quasi-neutral with no large scale charge separation. The derivation for the Debye length is shown in Equations 3.4 through 3.9. This is adapted from [4], starting with the assumption that the ion mobility is significantly lower than the electron mobility. Thus the ions do not, on the timescales of interest, have a chance

to rearrange themselves. The screening effects are limited to the localized distributions of the electrons.

$$m_e n_e \left(\frac{\partial \vec{v}_e}{\partial t} + \vec{v}_e \bullet \nabla \vec{v}_e \right) = -q n_e \vec{E} + m_e n_e \vec{v}_e \nu_{coll} - \nabla P_e \tag{3.4}$$

$$0 = \frac{d\phi}{dx_{\hat{E}}} - \frac{k_B T_e}{q n_e} \frac{d\,(n_e)}{dx_{\hat{E}}} \tag{3.5}$$

$$n_e = (n_{cation} - n_{anion}) \exp \left(\frac{q\phi}{k_B T_e} \right) \tag{3.6}$$

$$\nabla^2 \phi = \frac{q}{\epsilon_0} (n_{cation} - n_{anion}) \left(\exp \left(\frac{q\phi}{k_B T_e} \right) - 1 \right) \tag{3.7}$$

$$\nabla^2 \phi = \frac{q^2 \phi}{\epsilon_0 k_B T_e} (n_{cation} - n_{anion}) \tag{3.8}$$

$$\lambda_D = \sqrt{\frac{\epsilon_0 k_B T_e}{q^2 (n_{cation} - n_{anion})}} \tag{3.9}$$

Equation 3.4 is the electron momentum balance. Assuming negligible current, the left-hand side of the equation goes to zero, resulting in Equation 3.5. This can be integrated to achieve Equation 3.6. This distribution can be substituted into the Poisson equation (Equation 3.3), which, with some simplification becomes Equation 3.7. A Taylor expansion of the exponential allows a further simplification of the Poisson equation resulting in Equation 3.8. The Debye length for this system is thus defined as shown in Equation 3.9

3.1.3 Electron Temperature

The approximation of the electron temperature, T_e, is based on a collisional view of the plasma [14]. To estimate the electron temperature, electron collisions with heavy particles (the atoms and molecules that make up air) is taken into account. This derivation is shown in Equations 3.10 through 3.15.

$$m_e n_e \left(\frac{\partial \vec{v}_e}{\partial t} + \vec{v}_e \bullet \nabla \vec{v}_e \right) = -q n_e \vec{E} + m_e n_e \vec{v}_e \nu_{coll} - \nabla P_e \tag{3.10}$$

$$0 = -q n_e \vec{E} + m_e n_e \vec{v}_e \nu_{coll} \tag{3.11}$$

$$\nu_{coll} = |\vec{v}_e| n_{Heavy} \langle \sigma_{Heavy} \rangle \tag{3.12}$$

$$q\vec{E} = m_e \vec{v}_e |\vec{v}_e| n_{Heavy} \langle \sigma_{Heavy} \rangle \tag{3.13}$$

$$|\vec{v}_e| = \sqrt{\frac{k_B T_e}{m_e}} \tag{3.14}$$

$$T_e = \frac{q|\vec{E}|}{k_B n_{Heavy} \langle \sigma_{Heavy} \rangle} \tag{3.15}$$

Starting from the electron momentum equation (Equation 3.10), assume that the gradients in electron number density and electron temperature are small. Small gradients in electron temperature indicate gradients in electron velocity are also small, resulting in Equation 3.11. Equation 3.12 is the collision frequency as expected from collisional theory. It can be substituted into Equation 3.11, along with some simplification to result in Equation 3.13. Equation 3.14 shows the relationship of the speed of the electron to the electron temperature. This can be substituted back into Equation 3.13 to result in Equation 3.15. This approximation of the electron temperature can then be utilized throughout the simulation domain.

3.1.4 Boundary Conditions

As with any spatial PDE, boundary (and in this case, interface) conditions have a strong influence on the solution. Physically, the boundary and interface conditions are shown in Table 1. For an electrical dipole (which the actuator can be treated as in the far field), the potential must be zero. The electrodes are treated as perfect conductors, and therefore are imposed as isopotential surfaces, based on a known imposed potential difference as a function of time. Due to the downstream electrode being placed with a dielectric covering,

Table 1: Table of boundary conditions

Boundary	Condition
left	$\phi = 0$
top	$\phi = 0$
right	$\phi = 0$
bottom, $0 < x < \frac{L_x}{2}$	$\phi = 0$
bottom, $\frac{L_x}{2} < x < L_x$	$\epsilon_0 \frac{\partial \phi}{\partial y}\Big|_{y=\delta} = \epsilon_{dielectric} \frac{\partial \phi}{\partial y}\Big|_{y=-\delta}$

the boundary condition downstream of the surface electrode must account for the dielectric covering. This is done by ensuring that the displacement field is equal on each side of the boundary. The displacement field inside the dielectric is evaluated using a solution of the potential field shown in Equation 3.16. The subsurface boundary at the depth of the electrode is treated as a symmetry condition, except for the electrode itself, which is at a fixed potential.

$$\nabla^2 \phi = 0 \tag{3.16}$$

3.2   Chemical Kinetics

For a gas consisting of a collection of neutral particles (such as air), an applied electric field will cause no significant effect on the flow, unless something occurs that results in ionization. For the system of interest here, a set of chemical kinetic equations that are affected by an electric field must be solved in order to calculate the effect of the electric field on the flow.

Table 2: Example subset of reaction mechanisms

$e^- + O_2$	$\rightarrow$	$O + O^+ + 2e^-$	k_1
$O^+ + O$	$\rightarrow$	O_2^+	k_2
$e^- + O^+$	$\rightarrow$	O	k_3
$e^- + O_2^+$	$\rightarrow$	O_2	k_4
$e^- + O$	$\rightarrow$	$O^+ + 2e^-$	k_5
$e^- + O_2$	$\rightarrow$	$O_2^+ + 2e^-$	k_6

Table 3: Reaction rates for mechanism subset

$$
\begin{aligned}
\frac{dn_{O_2}}{dt} &= -k_1 n_{O_2} n_e + k_4 n_{O_2^+} n_e - k_6 n_{O_2} n_e \\
\frac{dn_O}{dt} &= k_1 n_{O_2} n_e - k_2 n_{O^+} n_O + k_3 n_{O^+} n_e - k_5 n_O n_e \\
\frac{dn_{O^+}}{dt} &= k_1 n_{O_2} n_e - k_2 n_{O^+} n_O - k_3 n_{O^+} n_e + k_5 n_O n_e \\
\frac{dn_{O_2^+}}{dt} &= k_2 n_{O^+} n_O - k_4 n_{O_2^+} n_e + k_6 n_{O_2} n_e \\
\frac{dn_e}{dt} &= k_1 n_{O_2} n_e - k_3 n_{O^+} n_e - k_4 n_{O_2^+} n_e + k_5 n_O n_e + k_6 n_{O_2} n_e
\end{aligned}
$$

3.2.1 Mechanisms

Reference [3] presents a set of chemical mechanisms appropriate to an air discharge. These 224 mechanisms are applied to 40 selected species. These species are those of air, and of atomic and molecular species that are readily produced in air. Table 4 contains a listing of each species and their initial distribution. These mechanisms result in a coupled set of 40 first order ODEs in time. A sample subset of mechanisms is provided in Table 2.

The reaction coefficients in the above table are used to compute reaction rates as shown in Table 3. This set of first-order ODEs then must be integrated in time to solve the species distributions.

To initiate the ionization, the set of equations provided in [3] requires an initial source of electrons, which, in this model, is provided by an equilibrium reaction between the atomic argon species and the argon cation species. The mechanism was developed from [9]. The

reaction is shown in Equations 3.17 through 3.19. The equilibrium between Ar and Ar^+ provides the electrons necessary for the chemical kinetic mechanisms. Equation 3.17 shows the equilibrium reaction. Equation 3.18 shows the thermochemical equilibrium condition [9]. Equation 3.19 is the nonlinear algebra equation that must be solved to compute the equilibrium condition.

$$e^- + Ar \quad \rightleftharpoons \quad Ar^+ + 2e^- \tag{3.17}$$

$$IE_a \quad = \quad k_B T_{gas} \ln \left(\frac{P_{Ar^+}}{P} \right) - k_B T_{gas} \ln \left(\frac{P_{Ar}}{P} \right) + k_B T_e \ln \left(\frac{P_{e^-}}{P} \right) \tag{3.18}$$

$$0 \quad = \quad (\chi_{Ar^+})^{\frac{k_B T_{gas}}{IE_a}} \left[\frac{T_e}{T_{gas}} \left(\chi_{\left(cations - anions - n_{Ar^+} \right)} + \frac{n_{(Ar+Ar^+)}}{n_{Heavy}} \chi_{Ar^+} \right) \right]^{\frac{k_B T_e}{IE_a}} \tag{3.19}$$
$$- (1 - \chi_{Ar^+})^{\frac{k_B T_{gas}}{IE_a}} \exp(-1)$$

3.2.2 Initial Conditions

To solve the above differential equations, an initial distribution of species is required. For the system here, the initial distribution is selected to be that of dry air [6]. This initial condition is shown in Table 4.

3.3 Transport

The final required element of the model is the species and momentum transport equations, which computes the flow behaviors of the system.

Table 4: Species initial conditions

species	mol fraction
N_2	.78084
N	0.0
N^+	0.0
$N\left(^2D\right)$	0.0
N_2^+	0.0
$N_2\left(A'^1\Sigma_\mu^-\right)$	0.0
$N_2\left(A^3\Sigma_\mu^+\right)$	0.0
N_2O	0.0
N_2O_5	0.0
N_4^+	0.0
NO	0.0
NO^+	0.0
NO_2	0.0
NO_2^+	0.0
NO_3	0.0
O_2	.20946
O	0.0
O^-	0.0
O^+	0.0
$O\left(^1D\right)$	0.0
O_2^-	0.0
O_2^+	0.0
$O_2\left(a^1\Delta_g\right)$	0.0
O_3	0.0
O_4^+	0.0

species	mol fraction
CO_2	.00038
CO	0.0
CO^+	0.0
CO_2^+	0.0
H_2O	0.0
H	0.0
H^+	0.0
H^-	0.0
H_2	0.0
H_2^+	0.0
H_2O^+	0.0
HNO_3	0.0
HO_2	0.0
OH	0.0
OH^+	0.0
Ar	.00932
Ar^+	0.0

3.3.1   Momentum Transport

The momentum equations solved are set up for two dimensional laminar flow with applied body forces, shown in Equation 3.20. The pressure is computed using the ideal gas equation of state along with Dalton's law of partial pressures as seen in Equation 3.21. The shear stress tensor, due to the need for the allowance of variable density across the flow field, makes the Stokes assumptions [16]. The Stokes assumption for a compressible fluid is shown in Equation 3.22. The assumptions for this formulation are that the fluid is Newtonian and isotropic. Further Stokes' estimate for the second viscosity coefficient is used as $-\frac{2}{3}\mu$.

$$\frac{\partial \rho \vec{v}}{\partial t} + \nabla \bullet (\rho \vec{v} \vec{v}) = -\nabla P + \nabla \bullet \vec{\vec{\tau}} + q\left(n_{cation} - n_{anion}\right)\vec{E} \tag{3.20}$$

$$P = \sum_{k=1}^{all\ species} n_k k_B T_{gas} \tag{3.21}$$

$$\vec{\vec{\tau}} = \mu \left(\nabla \vec{v} + (\nabla \vec{v})' - \frac{2}{3}\vec{\vec{I}}\nabla \bullet \vec{v} \right) \tag{3.22}$$

3.3.2   Species Transport

This model treats species transport as a purely convective mechanic with a source term. The source term is determined from the chemistry shown in Section 3.2. The governing equation is shown in Equation 3.23. With the calculation of the number density distributions, the gas density can be computed using Equation 3.24.

$$\frac{\partial n_k}{\partial t} + \nabla \bullet n_k \vec{v} = \left.\frac{dn_k}{dt}\right|_{reaction} \tag{3.23}$$

$$\rho = \sum_{k=1}^{all\ species} MW_k n_k \qquad (3.24)$$

3.3.3 Energy Transport

The energy transport is approximated as purely convective with a joule-heating term and the work done on the ions as shown in 3.25. The source terms are the resistive heating and the work done on the fluid. Rather than compute the plasma impedance, the resistive heating can alternately be computed as seen in 3.26, through a set of manipulations invoking the assumptions from 3.1.3 and Ohm's Law. This thermal heating is then multiplied against a fractional value indicating how much of the energy is thermalized versus the amount that is lost to radiation [3]. Back calculation of the local gas temperature is achieved through 3.27, derived from material in [18]. The gas properties are from the NIST Chemistry WebBook [32].

$$\frac{\partial \rho e}{\partial t} + \nabla \bullet (\rho e \vec{v}) = f_{th} \eta J^2 + q \left(n_{cations} - n_{anions} \right) \vec{E} \bullet \vec{v} \qquad (3.25)$$

$$\eta J^2 = q n_e \left| \vec{E} \right| \sqrt{\frac{k_B T_e}{m_e}} \qquad (3.26)$$

$$T_{gas} = T_{ref} + \frac{(\rho e) - n_e k_B T_e - \sum\limits_{k=1}^{all\ species} n_k \Delta \bar{e}^o_{f_k}}{\sum\limits_{k=1}^{all\ species} n_k \bar{c}_{v_k}} \qquad (3.27)$$
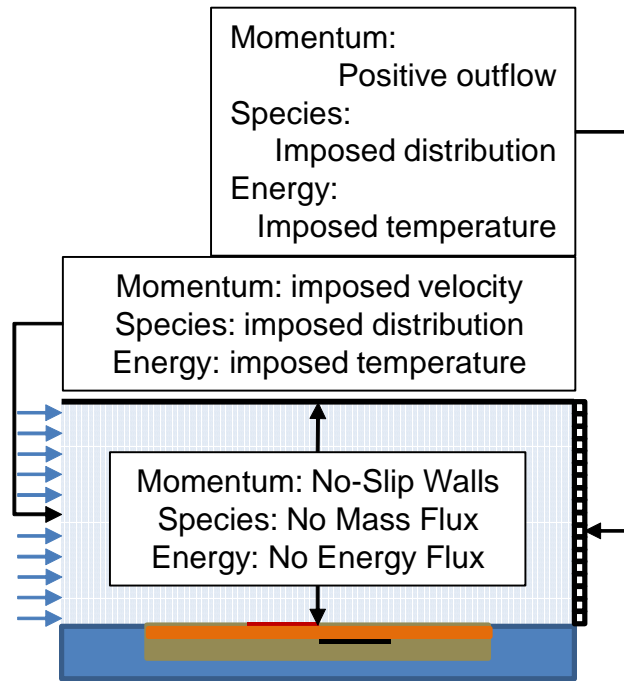
Figure 7: Boundary conditions for the transport equations for the passage flow

3.3.4   Flow Initial and Boundary Conditions

The transient initial conditions for the whole model are the steady-state flow condition with no applied voltage. The mole-fraction boundary conditions for the species transport equations have been shown in Table 4, with a discharge pressure of $101325Pa$.

The boundary conditions for the channel-flow are shown in Figure 7. All flows at a wall have zero velocity, with the inlet having an imposed value. The discharge boundary has imposed pressure and temperature.

Chapter 4

Numerical Model

This chapter covers the construction of the numerical method used to compute the behavior of a DBD flow control actuator. To begin, this chapter will discuss the framework within which the problem will be computed, with specifics on how the physics are computed following afterwards.

4.1 Modified Cellular Automata

The following section has been largely taken from work done in the author's Master's Thesis, [12]

The method of modified cellular automata is a technique that breaks up large, difficult to solve, multi-physics models into smaller, more easily solved mathematical elements. This method requires feeding the result of each single (or reduced multi-) physics "rule" into the next, and advancing through the set of rules with small, appropriately chosen steps (in this case, time). As a result of the breaking up of the physics into smaller rules, solved in a serial, rather than simultaneous, method, the order of the rule employment can have a small impact on the end result. However, it has been shown [40] that as the time step over which each
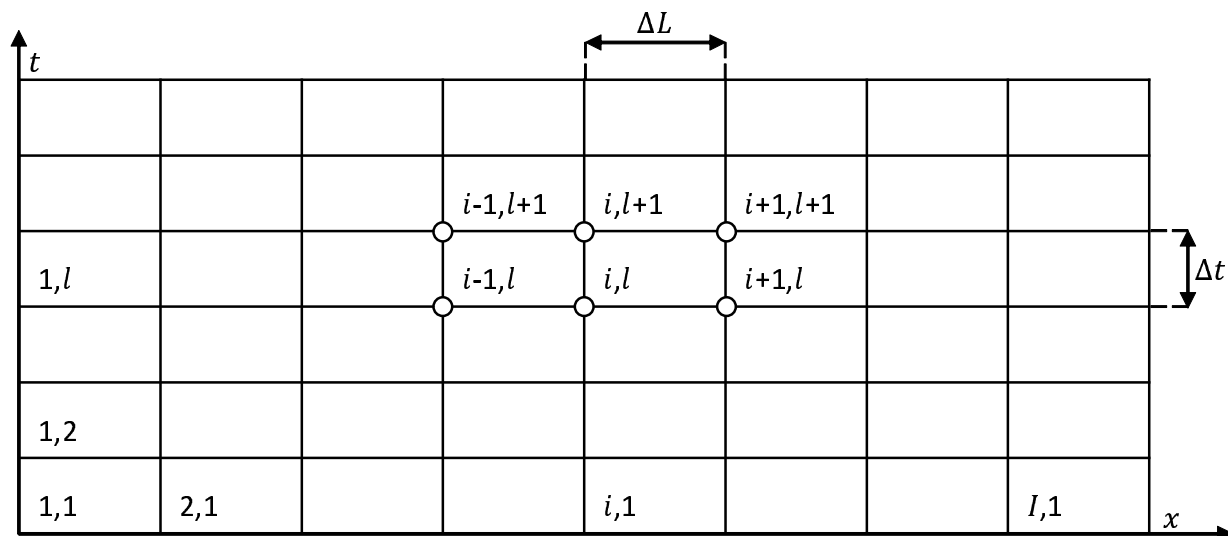
Figure 8: Time and space cellular grid example

rule is solved consecutively gets smaller, the differences in the results are reduced. Further, it was shown for the given examples that the order did not significantly affect the results.

The modified cellular automata method allows the user to draw from many well developed and understood solution methods. Finite difference methods, analytical solutions, and Runge-Kutta solvers are all available for use in this overall technique. After developing the mathematical model, one must then determine the breakdown of the mathematics into its simpler rules for the employment of this method. As an initial step, one must discretize the independent variable dimensions (space and time). Time is already discretized as a result of the cellular approach where the multi-physics are simulated for each major time step, however, smaller time steps may be employed within a specific "rule" for stability or accuracy reasons, as long as these smaller time steps re-synchronize at the selected time step for the modified cellular automata. Space also needs to be discretized based on any requirements regarding the spatial resolution. Similarly, a different spatial grid framework can be used provided the results from the "rule" are transformed back onto the main simulation grid. This discrete grid can conceptually be represented in Figure 8.

The formalism for this method follows here. For a given state variable of interest, ψ, and

each of the physical processes to be modeled, p, a governing equation exists of the form shown in Equation 4.1, and is functional on itself, space, and time. Each of the individual physical processes, $\boldsymbol{f}_p$ can be expressed as Equation 4.2.

$$\frac{\partial \psi}{\partial t} = \sum_{p=1}^{P} \boldsymbol{f}_p \left(\psi, \vec{x}, t\right) \tag{4.1}$$

$$\left.\frac{\partial \psi}{\partial t}\right|_p = \boldsymbol{f}_p \left(\psi, \vec{x}, t\right), \qquad p = 1, 2 \ldots P \tag{4.2}$$

For each of these processes, one must develop a solution technique. Many processes can be analytically solvent when broken down appropriately, however that is not the case within the current body of research. These processes proved reasonably easy to solve using other methods such as backwards Euler, or finite volume methods. Whatever technique is employed, the time-advanced solution of the individual process can be represented as shown in Equation 4.3, where $\boldsymbol{\mathcal{F}}_p$ is the method used to advance the process by one time step.

$$\psi^{l+1} = \boldsymbol{\mathcal{F}}_p \left(\psi^l, \vec{x}, t\right) \tag{4.3}$$

For any multi-physics system, while advancing a single time step, the result of each rule is fed into the next until each rule is used. Thus, for multiple physics, the solution procedure for a single time step advancement is shown in Equation 4.4. For each intermediate process, it produces a result, ψ_p^l that is used as the input to the subsequent "rule" until each physics has been solved. Graphically, this can be seen in Figure 9.

$$
\begin{aligned}
\psi_1^l &= \boldsymbol{\mathcal{F}}_1\left(\psi^l, \vec{x}, t\right) \\
\psi_2^l &= \boldsymbol{\mathcal{F}}_2\left(\psi_1^l, \vec{x}, t\right) \\
&\vdots \\
\psi_p^l &= \boldsymbol{\mathcal{F}}_p\left(\psi_{p-1}^l, \vec{x}, t\right) \\
&\vdots \\
\psi_{P-1}^l &= \boldsymbol{\mathcal{F}}_{P-1}\left(\psi_{P-2}^l, \vec{x}, t\right) \\
\psi^{l+1} = \psi_P^l &= \boldsymbol{\mathcal{F}}_L\left(\psi_{P-1}^l, \vec{x}, t\right)
\end{aligned}
$$

$$(4.4)$$

The multi-physics system studied in the current work has forty-five state variables of interest. These are the electrical potential, the forty-two species number densities, and the x and y momentum. These all interact through the three physics "rules" that were discussed in Chapter 3. The choice of the order of solution is, for each time step, as follows: Solve for the electrical potential (whose negative gradient is the electric field), next integrate the chemical kinetics, and then, solve the species and momentum transport equations. A top level flowchart of the model is shown in Figure 10.

4.2   Electrical Potential

The electrical potential field for a quasi-neutral plasma that exhibits shielding is governed by Equation 4.5, as developed using Equations 3.4 through 3.9. As this is a second order differential equation, it can conveniently be discretized on a uniform grid for a finite-volume approach to second-order accuracy as Equation 4.6. This equation can be made as a line-implicit solution in either direction appropriate for a parallelized alternating direction implicit (parallel ADI) solution method adapted from [37]. The formulations these take are

31
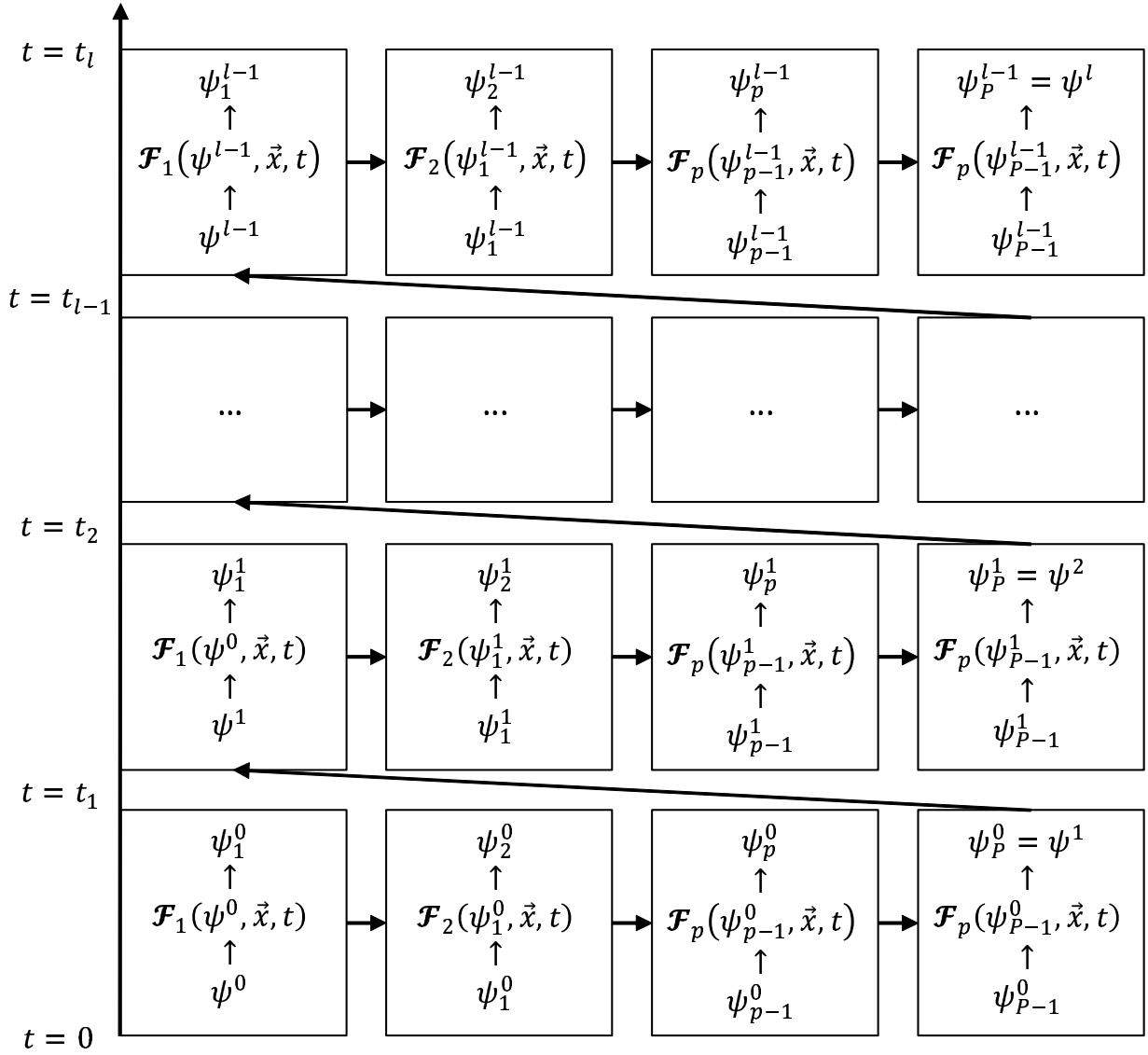
Figure 9: Graphical representation of the modified celluar automata information flow
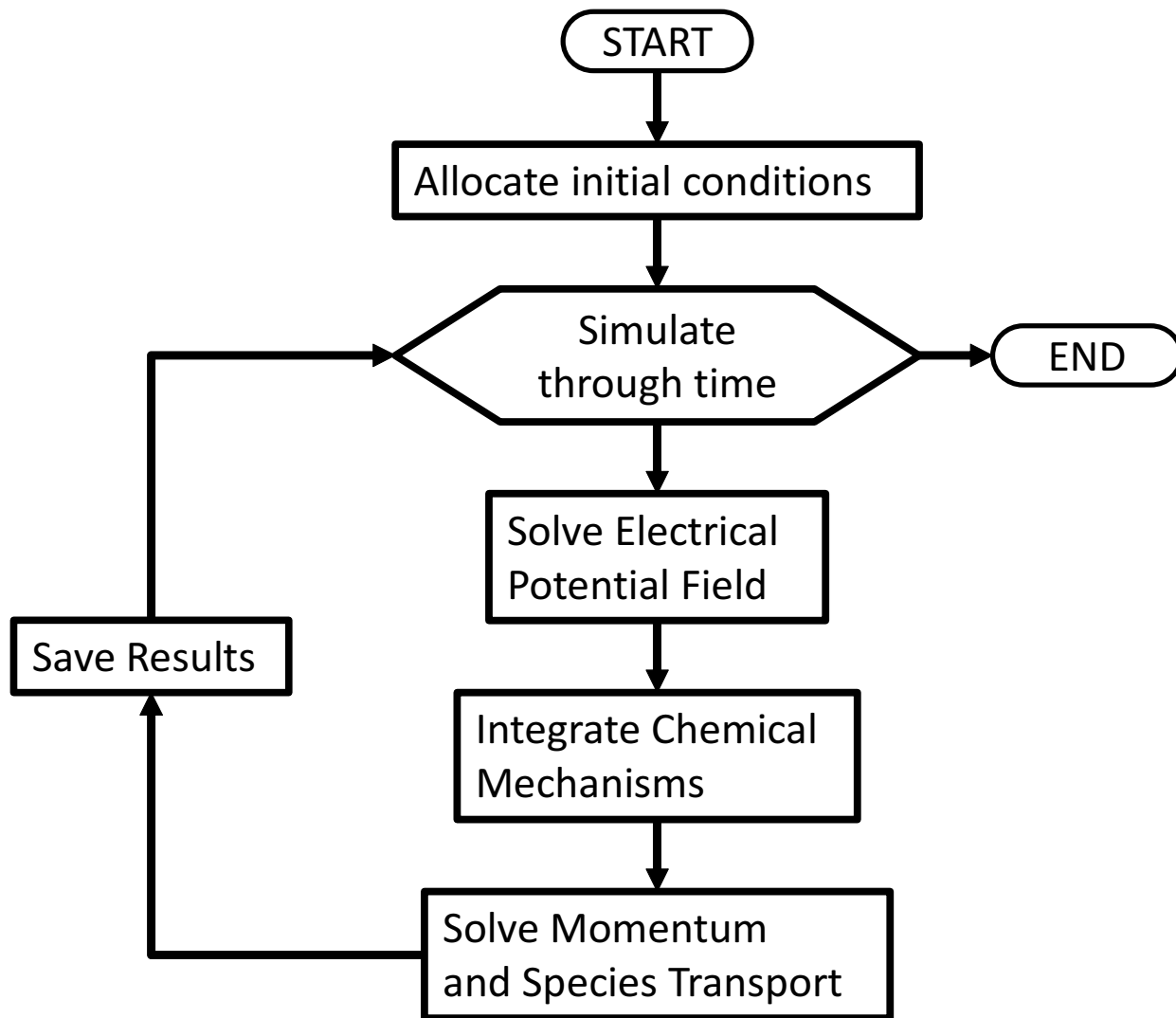
Figure 10: Top level flowchart of numerical simulation code

shown in 4.7 and 4.8. The starred values of number density are the previous iteration's solution at those grid locations.

$$\nabla^2 \phi = \frac{\phi}{\lambda_D^2} \tag{4.5}$$

$$\phi_{i+1,j}^* + \phi_{i-1,j}^* + \phi_{i,j+1}^* + \phi_{i,j-1}^* - 4\phi_{i,j}^{t+1} = \frac{\Delta L^2}{\lambda_D^2}\phi_{i,j}^{t+1} \tag{4.6}$$

$$\phi_{i+1,j}^{t+1} + \phi_{i-1,j}^{t+1} + \phi_{i,j+1}^* + \phi_{i,j-1}^* - 4\phi_{i,j}^{l+1} = \frac{\Delta L^2}{\lambda_D^2}\phi_{i,j}^{t+1} \tag{4.7}$$

$$\phi_{i+1,j}^* + \phi_{i-1,j}^* + \phi_{i,j+1}^{t+1} + \phi_{i,j-1}^{t+1} - 4\phi_{i,j}^{l+1} = \frac{\Delta L^2}{\lambda_D^2}\phi_{i,j}^{t+1} \tag{4.8}$$

Upon solution of the potential field, the electric field components can be computed. These field component calculations are shown in Equations 4.9 and 4.10. These are first order differences that place the calculation of the electric field on the staggered grid such that the components of the electric field are coincident with their momentum counterparts.

$$E_{x_{i,j}}^{t+1} = -\left(\frac{\phi_{i,j}^{t+1} - \phi_{i-1,j}^{t+1}}{\Delta L}\right) \tag{4.9}$$

$$E_{y_{i,j}}^{t+1} = -\left(\frac{\phi_{i,j}^{t+1} - \phi_{i,j-1}^{t+1}}{\Delta L}\right) \tag{4.10}$$

4.3 Chemical Kinetics

With the electric field now known, and the calculation of the electron temperature from Equation 3.15, the chemical kinetics can now be integrated. To integrate the chemical kinetics, a first order, under-relaxed, Euler implicit (predictor-corrector) method was used. Each computational cell was solved independently. An advantage to this cell-by-cell approach to the chemistry integration is that it allows easy parallelization of the algorithm. A flow chart of the chemistry integrator is shown in Figure 11.

This integrator was designed to ensure non-negative results for the individual number densities. This works by a Taylor expansion of the reaction rate around the predicted value, n_k^*, and solving the resulting solution matrix using Gaussian elimination with back substitution (4.11). If any number density is found to be negative, the under-relaxation value, ω, is reduced to a level to result in a positive result, and the results advance to the next iteration to convergence (4.12).

The major components of air are used for nuclear conservation, i.e. the number density of N_2 ensures that the sum total count of nitrogen atoms in all species remains the same over the integrated time step. The same process holds true for O_2 and CO_2. The example for carbon conservation is shown in 4.13. The electrons are used similarly for charge balance, i.e. the sum of all cations minus the sum of all anions must be positive (4.14), and the sum of all cations minus the sum of all anions and electrons must be zero, to further ensure quasi-neutrality (4.15).

$$n_k^{t+1} = n_k^t + rr_k\left(n_k^*\right) + \sum_{m=1}^{all\ species} \frac{rr_k^*}{\partial n_m}\left(n_m^{t+1} - n_m^*\right) \tag{4.11}$$

$$n_k^{t+1} = \omega\left(n_k^{t+1} - n_k^*\right) + n_k^* \tag{4.12}$$
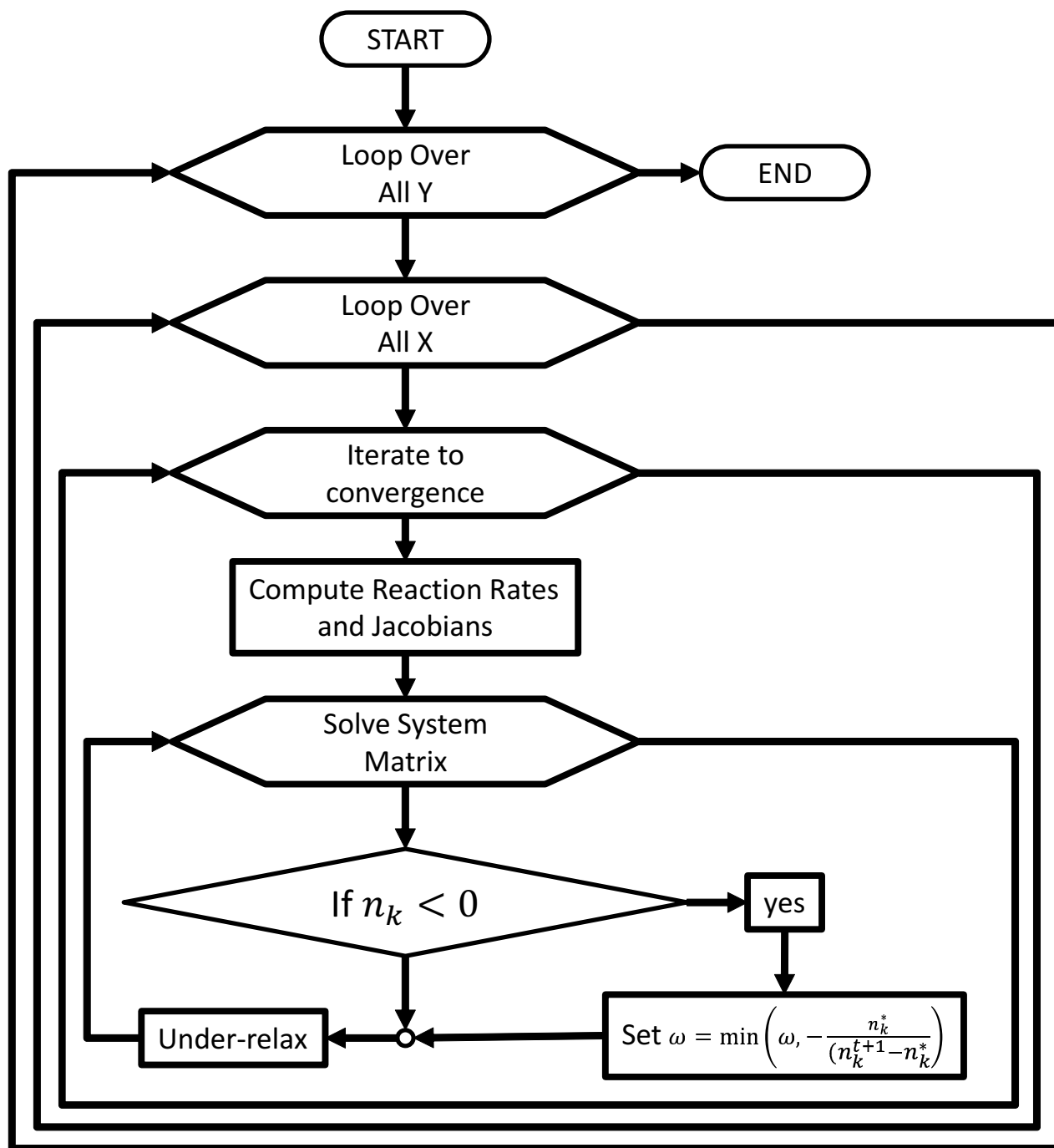
Figure 11: Chemical kinetics integration flow chart

$$n_{CO_2}^{t+1} + n_{CO}^{t+1} + n_{CO_2^+}^{t+1} + n_{CO^+}^{t+1} = n_{CO_2}^t + n_{CO}^t + n_{CO_2^+}^t + n_{CO^+}^t \tag{4.13}$$

$$n_e = \sum n_{cations} - \sum n_{anions} \geq 0 \tag{4.14}$$

$$n_e + \sum n_{anions} + \sum n_{cations} = 0 \tag{4.15}$$

External to the function that computes the reaction rates, the equilibrium reaction described in Equation 3.19 is solved. This nonlinear algebraic equation is solved using a simple bisecting method.

4.4   Transport

As discussed above in Chapter 3, conservation of species and momentum is observed using the Navier-Stokes equations for a compressible Newtonian fluid. This section presents the numerical approximation used for this work. The general approach employs a staggered grid to implement a finite volume discretization technique. A sub-section of the grid to demonstrate this is shown in Figure 12. Within the figure, the species and energy can be seen to be evaluated at the cell centers, whereas the momentum components are evaluated as normal values to the cell faces. The implication is that the control volumes of each flow variable are staggered as well. This is represented in the figure by having each text callout point to the center of the associated control volume. The solid line is associated with species and energy control volumes, the long dashes are associated with the x-momentum control volume, and the short dashes are associated with the y-momentum control volume. The numerical diffusion of the first-order upwinding scheme was deemed to be acceptable because it is computationally inexpensive and stable, but still showcases the relevant physics
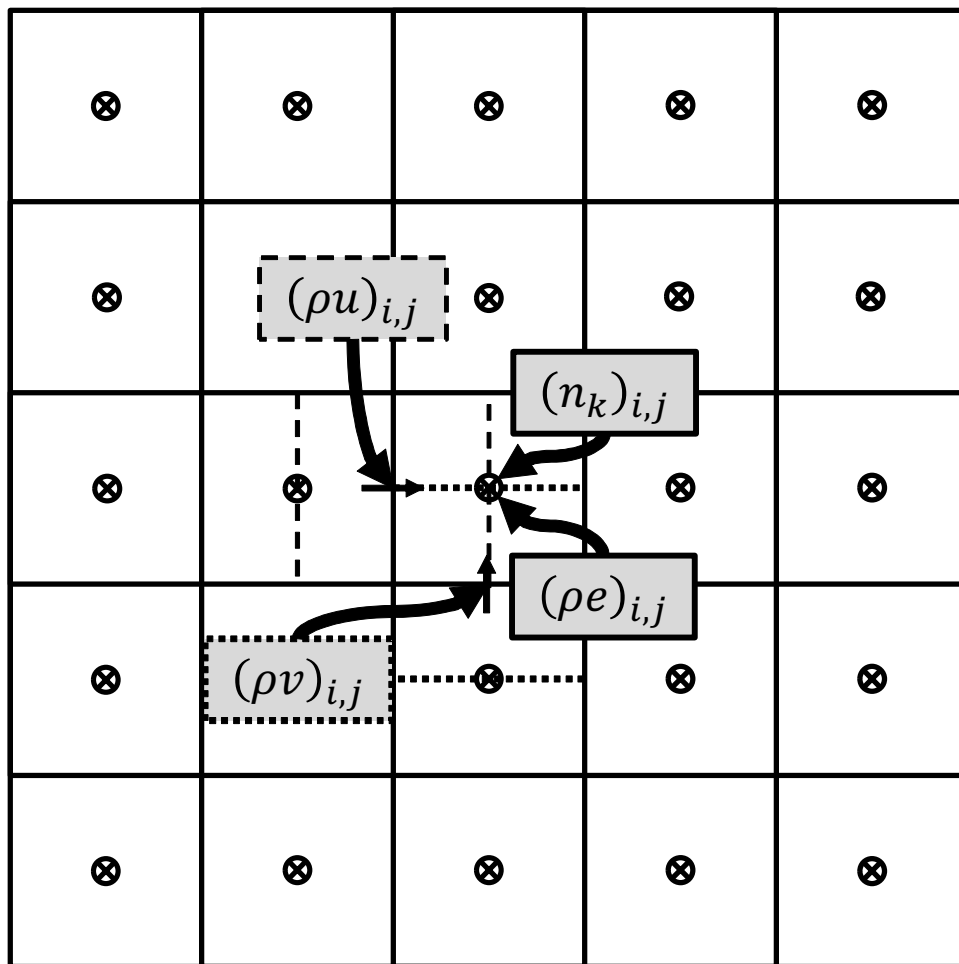
Figure 12: Graphical representation of staggered grid used to discretize transport equations

involved. The added diffusion should produce a conservative underestimate of the amount of flow control produced. A second order model is recommended for future development.

4.4.1 Species Transport

The first of the transport equations to be discretized here are the species transport equations. They are repeated in Equation 4.16. The first term that needs to be handled is the source term on the right hand side. Unlike the mass continuity equation where the source term is always zero, this set of equations requires that the conversion of species via chemistry

is accounted for in the source term. This term is treated as the difference between the time-integrated chemistry results and the previous time step results as shown in Equation 4.17.

$$\frac{\partial n_k}{\partial t} + \nabla \bullet n_k \vec{v} = \frac{dn_k}{dt}\bigg|_{reaction} \tag{4.16}$$

$$\frac{dn_k}{dt}\bigg|_{reaction} = \frac{n_k^{rxn} - n_k^t}{\Delta t} \tag{4.17}$$

Equation 4.16 can be integrated over the cell volume, with an upwinding scheme for the convective flux. This can then be integrated over the time step to give the discretized form of the species conservation equations shown in Equation 4.18. Appropriate forms to solve semi-implicitly using the previously discussed parallel ADI solution technique (employed to solve the electrical potential field) are shown in 4.19 and 4.20. The starred values of number density are the previous iteration's solution at those grid locations.

$$
\begin{aligned}
n_{k_{i,j}}^{t+1} &\left\{ \Delta L + \Delta t \left[\max\left(u_{E_s}, 0\right) - \min\left(u_{W_s}, 0\right) + \max\left(v_{N_s}, 0\right) - \min\left(v_{S_s}, 0\right) \right] \right\} \\
&+ n_{k_{i+1,j}}^* \min\left(u_{E_s}, 0\right) - n_{k_{i-1,j}}^* \max\left(u_{W_s}, 0\right) \\
&+ n_{k_{i,j+1}}^* \min\left(v_{N_s}, 0\right) - n_{k_{i,j-1}}^* \max\left(v_{S_s}, 0\right) \\
&= \Delta L \left(n_{k_{i,j}}^{rxn} \right)
\end{aligned}
\tag{4.18}
$$

$$
\begin{aligned}
n_{k_{i,j}}^{t+1} &\left\{ \Delta L + \Delta t \left[\max\left(u_{E_s}, 0\right) - \min\left(u_{W_s}, 0\right) + \max\left(v_{N_s}, 0\right) - \min\left(v_{S_s}, 0\right) \right] \right\} \\
&+ n_{k_{i+1,j}}^{t+1} \min\left(u_{E_s}, 0\right) - n_{k_{i-1,j}}^{t+1} \max\left(u_{W_s}, 0\right) \\
&+ n_{k_{i,j+1}}^* \min\left(v_{N_s}, 0\right) - n_{k_{i,j-1}}^* \max\left(v_{S_s}, 0\right) \\
&= \Delta L \left(n_{k_{i,j}}^{rxn} \right)
\end{aligned}
\tag{4.19}
$$

$$
\begin{aligned}
n_{k_{i,j}}^{t+1} &\left\{ \Delta L + \Delta t \left[\max\left(u_{E_s}, 0\right) - \min\left(u_{W_s}, 0\right) + \max\left(v_{N_s}, 0\right) - \min\left(v_{S_s}, 0\right) \right] \right\} \\
&+ n_{k_{i+1,j}}^{*} \min\left(u_{E_s}, 0\right) - n_{k_{i-1,j}}^{*} \max\left(u_{W_s}, 0\right) \\
&+ n_{k_{i,j+1}}^{t+1} \min\left(v_{N_s}, 0\right) - n_{k_{i,j-1}}^{t+1} \max\left(v_{S_s}, 0\right) \\
&= \Delta L \left(n_{k_{i,j}}^{rxn} \right)
\end{aligned}
\tag{4.20}
$$

In these equations, it is necessary to compute the face velocities for the species control volume. This is done by dividing the appropriate momentum component (due to the staggered grid) by the arithmetic mean of the densities of the cells that share the face. This can be seen in Equations 4.21 through 4.24. These face velocities are updated each iteration as the simulation works towards convergence. Within the program, these species velocities are retained because they can be reused in some of the differences that exist within the momentum equations.

$$
u_{E_s} = 2\frac{(\rho u)_{i+1,j}}{\rho_{i+1,j} + \rho_{i,j}}
\tag{4.21}
$$

$$
u_{W_s} = 2\frac{(\rho u)_{i,j}}{\rho_{i,j} + \rho_{i-1,j}}
\tag{4.22}
$$

$$
v_{N_s} = 2\frac{(\rho v)_{i,j+1}}{\rho_{i,j+1} + \rho_{i,j}}
\tag{4.23}
$$

$$
v_{S_s} = 2\frac{(\rho u)_{i,j}}{\rho_{i,j} + \rho_{i,j-1}}
\tag{4.24}
$$

4.4.2 X-Momentum Transport

The next equation to be discretized is the x-momentum transport equation. The differential equation for the x-momentum is shown in Equation 4.25. In like fashion with the species

equations, the discretization of this equation begins with the integration over the cell volume and then is integrated over the time step. The differences that need to be approximated within this equation are evaluated with first-order upwinding for the convective terms and second-order central for the viscous terms. The resulting discretized equation is shown in Equation 4.26. Appropriate forms to solve semi-implicitly using the previously discussed parallel ADI solution technique (employed to solve the electrical potential field) are generated in like fashion to Equations 4.19 and 4.20. The starred values of number density are the previous iteration's solution at those grid locations.

$$\frac{\partial \rho u}{\partial t} + \frac{\partial (\rho u u)}{\partial x} + \frac{\partial (\rho u v)}{\partial y} = -\frac{\partial P}{\partial x} + \frac{\partial \tau_{x,x}}{\partial x} + \frac{\partial \tau_{x,y}}{\partial y} + q \left(n_{cation} - n_{anion} \right) E_x \tag{4.25}$$

$$
\begin{aligned}
(\rho u)_{i,j}^{t+1} & \left[\Delta L^2 + \frac{40}{3} \left(\frac{\mu \Delta t}{\rho_{i,j} + \rho_{i-1,j}} \right) \right. \\
& \left. + \Delta L \Delta t \left(\max \left(u_{E_x}, 0 \right) - \min \left(u_{W_x}, 0 \right) + \max \left(v_{N_x}, 0 \right) - \min \left(v_{S_x}, 0 \right) \right) \right] \\
& + (\rho u)_{i-1,j}^{*} \left[-\Delta L \Delta t \max \left(u_{E_x}, 0 \right) - \frac{14}{3} \left(\frac{\mu \Delta t}{\rho_{i-2,j} + \rho_{i-1,j}} \right) \right] \\
& + (\rho u)_{i+1,j}^{*} \left[\Delta L \Delta t \min \left(u_{W_x}, 0 \right) - \frac{14}{3} \left(\frac{\mu \Delta t}{\rho_{i,j} + \rho_{i+1,j}} \right) \right] \\
& + (\rho u)_{i,j-1}^{*} \left[-\Delta L \Delta t \max \left(v_{S_x}, 0 \right) - \frac{14}{3} \left(\frac{\mu \Delta t}{\rho_{i,j-1} + \rho_{i-1,j-1}} \right) \right] \\
& + (\rho u)_{i,j+1}^{*} \left[\Delta L \Delta t \min \left(v_{N_x}, 0 \right) - \frac{14}{3} \left(\frac{\mu \Delta t}{\rho_{i,j+1} + \rho_{i-1,j+1}} \right) \right] \\
& = \Delta L^2 (\rho u)_{i,j}^{t} - \Delta L \Delta t \left(P_{i,j} - P_{i-1,j} \right) + q \left(n_{cations} - n_{anions} \right) E_x \\
& + \left(\frac{4}{3} \right) \mu \Delta t \left(v_{N_s} - v_{S_s} - v_{N_s[i-1,j]} + v_{S_s[i-1,j]} \right)
\end{aligned}
\tag{4.26}
$$

As in the species transport equations, it is necessary to compute the face velocities for the momentum control volume. Expressions for the face values are shown in Equations 4.27 through 4.30. Like the species control volume face velocities, an appropriate average is

taken of the momentum flux divided by an appropriate average of the density at the same location.

$$u_{E_x} = \frac{(\rho u)_{i,j} + (\rho u)_{i+1,j}}{2\rho_{i,j}} \tag{4.27}$$

$$u_{W_x} = \frac{(\rho u)_{i-1,j} + (\rho u)_{i,j}}{2\rho_{i-1,j}} \tag{4.28}$$

$$v_{N_x} = 2\frac{(\rho v)_{i,j+1} + (\rho v)_{i-1,j+1}}{\rho_{i,j+1} + \rho_{i,j} + \rho_{i-1,j+1} + \rho_{i-1,j}} \tag{4.29}$$

$$v_{S_x} = 2\frac{(\rho v)_{i,j} + (\rho v)_{i-1,j}}{\rho_{i,j-1} + \rho_{i,j} + \rho_{i-1,j-1} + \rho_{i-1,j}} \tag{4.30}$$

4.4.3 Y-Momentum Transport

The next equation to be discretized is the y-momentum transport equation. The differential equation for the y-momentum is shown in Equation 4.31. In like fashion with the species equations, the discretization of this equation begins with the integration over the cell volume and then is integrated over the time step. The differences that need to be approximated within this equation are evaluated with first-order upwinding for the convective terms and second-order central for the viscous terms. The resulting discretized equation is shown in Equation 4.32. Appropriate forms to solve semi-implicitly using the previously discussed parallel ADI solution technique are generated in like fashion to Equations 4.19 and 4.20. The starred values of number density are the previous iteration's solution at those grid locations.

$$\frac{\partial \rho v}{\partial t} + \frac{\partial (\rho v u)}{\partial x} + \frac{\partial (\rho v v)}{\partial y} = -\frac{\partial P}{\partial y} + \frac{\partial \tau_{y,x}}{\partial x} + \frac{\partial \tau_{y,y}}{\partial y} + q\left(n_{cation} - n_{anion}\right)E_y \tag{4.31}$$

$$(\rho v)_{i,j}^{t+1} \left[\Delta L^2 + \frac{40}{3} \left(\frac{\mu \Delta t}{\rho_{i,j} + \rho_{i,j-1}} \right) \right.$$

$$\left. + \Delta L \Delta t \left(\max \left(u_{E_y}, 0 \right) - \min \left(u_{W_y}, 0 \right) + \max \left(v_{N_y}, 0 \right) - \min \left(v_{S_y}, 0 \right) \right) \right]$$

$$+ (\rho v)_{i-1,j}^{*} \left[-\Delta L \Delta t \max \left(u_{E_y}, 0 \right) - \frac{14}{3} \left(\frac{\mu \Delta t}{\rho_{i-1,j} + \rho_{i-1,j-1}} \right) \right]$$

$$+ (\rho v)_{i+1,j}^{*} \left[\Delta L \Delta t \min \left(u_{W_y}, 0 \right) - \frac{14}{3} \left(\frac{\mu \Delta t}{\rho_{i+1,j} + \rho_{i+1,j-1}} \right) \right]$$

$$+ (\rho v)_{i,j-1}^{*} \left[-\Delta L \Delta t \max \left(v_{S_y}, 0 \right) - \frac{14}{3} \left(\frac{\mu \Delta t}{\rho_{i,j-1} + \rho_{i,j-2}} \right) \right]$$

$$+ (\rho v)_{i,j+1}^{*} \left[\Delta L \Delta t \min \left(v_{N_y}, 0 \right) - \frac{14}{3} \left(\frac{\mu \Delta t}{\rho_{i,j+1} + \rho_{i,j}} \right) \right]$$

$$= \Delta L^2 \left(\rho v \right)_{i,j}^{t} - \Delta L \Delta t \left(P_{i,j} - P_{i,j-1} \right) + q \left(n_{cations} - n_{anions} \right) E_y$$

$$+ \left(\frac{4}{3} \right) \mu \Delta t \left(u_{E_s} - u_{W_s} - u_{E_s[i,j-1]} + u_{W_s[i,j-1]} \right)$$

(4.32)

In like fashion with the x-momentum transport equation, it is necessary to compute the face velocities for the y-momentum control volume. Expressions for the face values are shown in Equations 4.33 through 4.36. Again, an appropriate average is taken of the momentum flux divided by an appropriate average of the density at the same location.

$$u_{E_y} = 2 \frac{(\rho u)_{i+1,j} + (\rho u)_{i+1,j-1}}{\rho_{i+1,j} + \rho_{i,j} + \rho_{i,j-1} + \rho_{i+1,j-1}} \tag{4.33}$$

$$u_{W_y} = 2 \frac{(\rho u)_{i,j} + (\rho u)_{i,j-1}}{\rho_{i,j} + \rho_{i-1,j} + \rho_{i,j-1} + \rho_{i-1,j-1}} \tag{4.34}$$

$$v_{N_y} = \frac{(\rho v)_{i,j} + (\rho v)_{i,j+1}}{2\rho_{i,j}} \tag{4.35}$$

$$v_{S_y} = \frac{(\rho v)_{i,j} + (\rho v)_{i,j-1}}{2\rho_{i,j-1}} \tag{4.36}$$

43

4.4.4   Energy Transport

The next equation to be discretized is the internal energy transport equation. The differential equation for the internal energy is shown in Equation 4.37. In like fashion with the species equations, the discretization of this equation begins with the integration over the cell volume and then is integrated over the time step. The differences that need to be approximated within this equation are evaluated with first-order upwinding for the convective terms. The resulting discretized equation is shown in Equation 4.38. Appropriate forms to solve semi-implicitly using the previously discussed parallel ADI solution technique are generated in like fashion to Equations 4.19 and 4.20. The starred values of number density are the previous iteration's solution at those grid locations.

$$\frac{\partial \rho e}{\partial t} + \nabla \bullet (\rho e \vec{v}) = f_{th} q n_e \left|E\right| \sqrt{\frac{k_B T_e}{m_e}} + q \left(n_{cations} - n_{anions}\right) \vec{E} \bullet \vec{v} \tag{4.37}$$

$$
\begin{aligned}
(\rho e)_{i,j}^{t+1} & \left[\Delta L + \Delta t \left(\max\left(u_{E_s}, 0\right) - \min\left(u_{W_s}, 0\right) + \max\left(v_{N_s}, 0\right) - \min\left(v_{S_s}, 0\right)\right)\right] \\
& + (\rho e)_{i-1,j}^{*} \left[-\Delta L \Delta t \max\left(u_{E_s}, 0\right)\right] + (\rho e)_{i+1,j}^{*} \left[\Delta L \Delta t \min\left(u_{W_s}, 0\right)\right] \\
& + (\rho e)_{i,j-1}^{*} \left[-\Delta L \Delta t \max\left(v_{S_s}, 0\right)\right] + (\rho e)_{i,j+1}^{*} \left[\Delta L \Delta t \min\left(v_{N_s}, 0\right)\right] \\
& = f_{th} q n_e \left|E\right| \sqrt{\frac{k_B T_e}{m_e}} + q \left(n_{cations} - n_{anions}\right) \left(E_x u_{E_x} + E_y v_{N_y}\right)
\end{aligned}
\tag{4.38}
$$

Chapter 5

Numerical Results

This chapter presents results generated by the numerical model. Calculations were additionally made to facilitate validation against experimental data. The simulation was run for four pulse cycles. Each cycle has an applied pulse that can be seen in Figure 13.

5.1 Converged Initial Condition

With the applied voltage set to zero, the numerical model was converged to a steady condition to provide the initial conditions for the model to run with the proper applied voltage time-trace. Appendix A contains the steady state solutions of x-momentum, y-momentum, static pressure, and total number density for $5.0kg/(m^2 - s)$ inlet mass flux. These contours show that the flow starts as primarily a bulk flow condition, with some local acceleration near the uniform inlet as the boundary layer sets up. The initial boundary layer can be seen in Figure 14. The initial acceleration of the flow near the inlet condition is quite visible in the near-inlet traces, but it quickly establishes itself in a typical boundary layer profile. Outside of the near-inlet region, the x-momentum term is established as a nearly slug flow behavior at nearly the inlet momentum, with the y-momentum components nearly zero. The gas
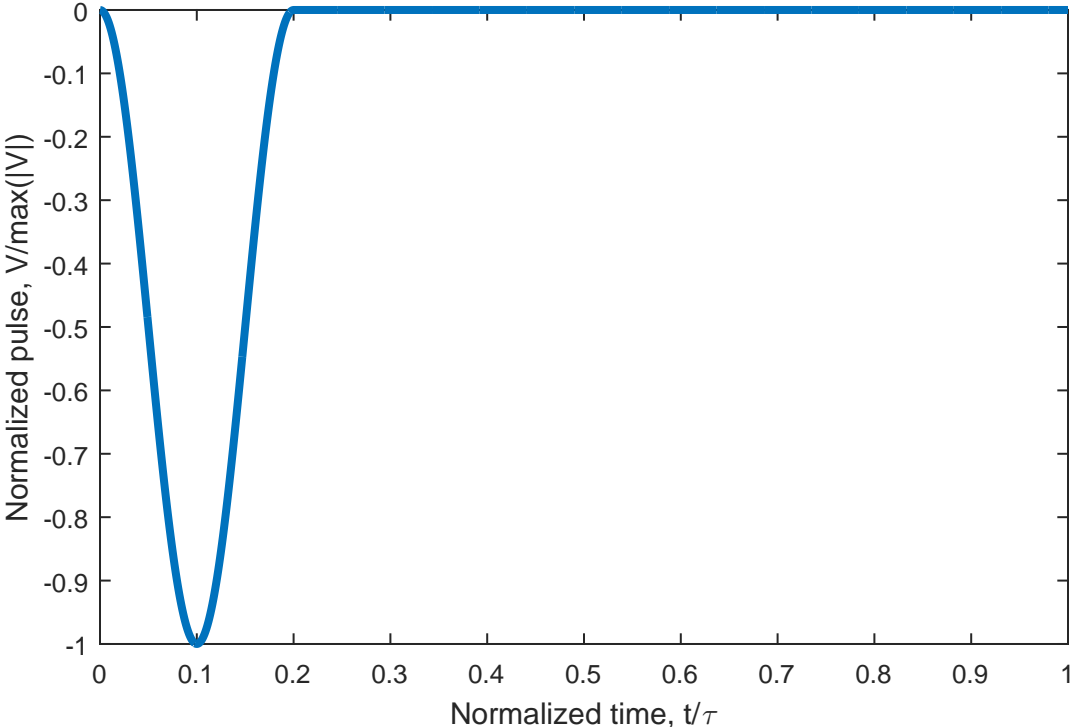
Figure 13: Idealized applied voltage pulse
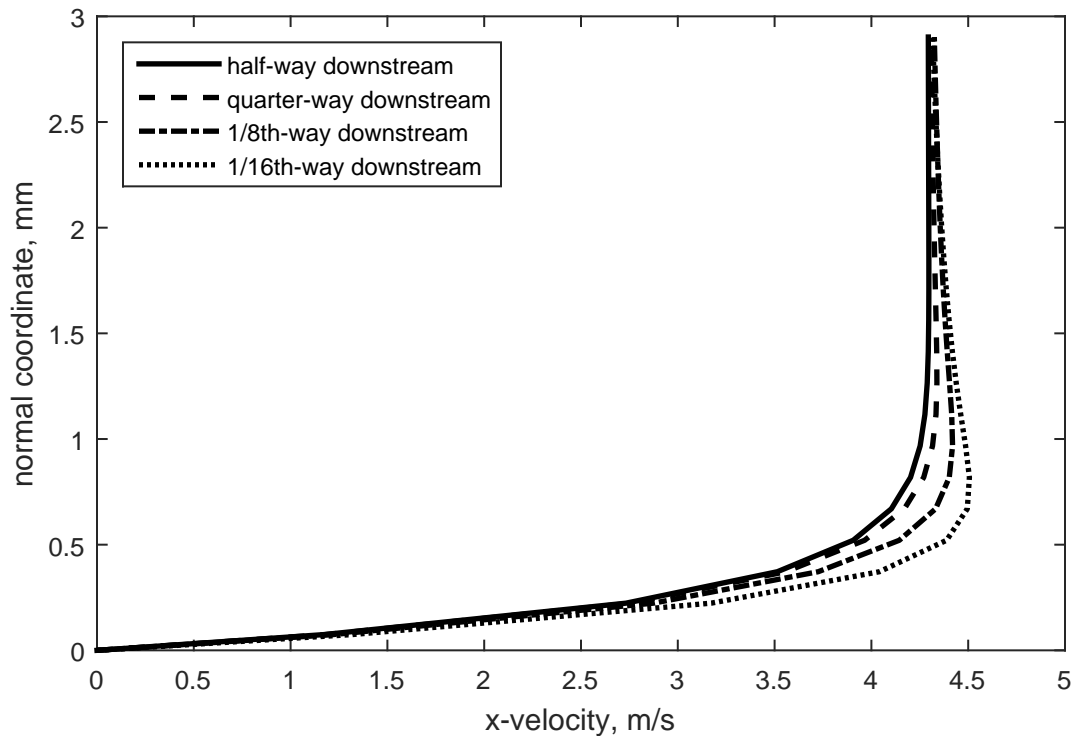
Figure 14: Initial boundary layer for $5.0kg/(m^2 - s)$ inflow

temperature is effectively uniform at $T_{gas} = 300K$, as the speed is low, and the chemistry is inactive for the initial condition calculations.

5.2 Model Results

This section presents the model predictions of the effect of the actuator on the flow. First, an example set of raw predictions are shown, followed by additional post processed results.

5.2.1 Example Raw Results

Presented here are contours predicted by the model of streamwise velocity, wall normal velocity, pressure, temperature, electron number density, and electron temperature. Figure

Figure 15: Example fluid results with captured pressure wave for $5.0 kg/(m^2 - s)$ inflow at $125\mu s$.

15 contains the flow results of x and y momentum, temperature, and pressure. These fluid results show the interaction of the momentum and pressure, with minimal effect in the far f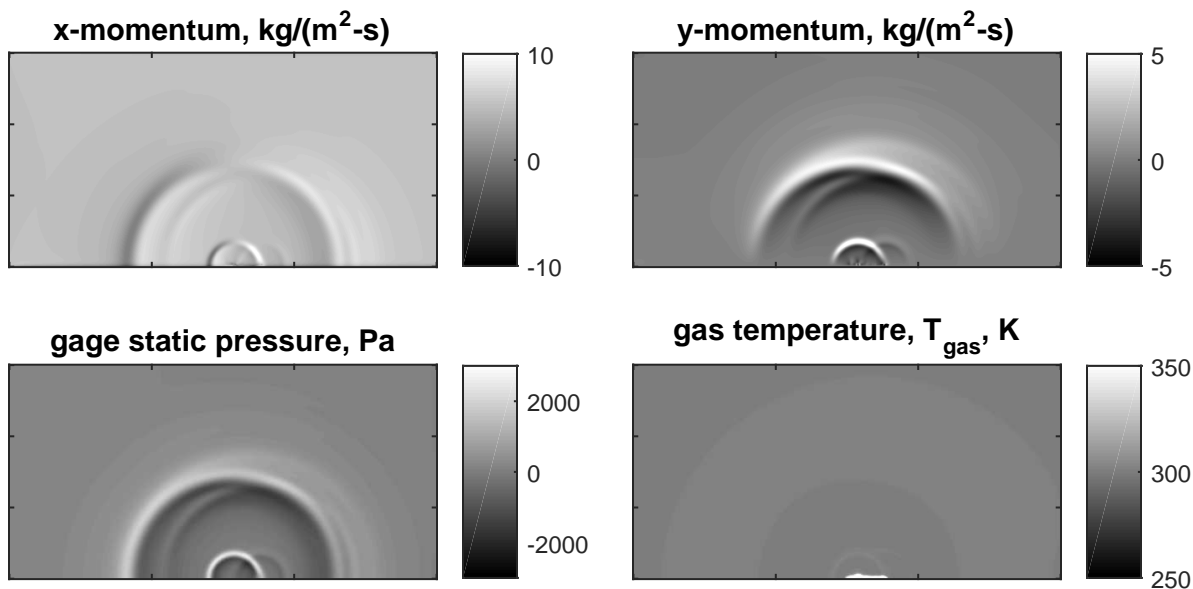ield on temperature, and that the temperature remains elevated by the actuator. These results also depict the acoustic wave that propagates away from the actuator.

Figure 16 illustrates the model predictions of the electron temperature distribution. It shows the effect of the increased energy of the free electrons stays very close to the actuator. The inset axes show the full field whereas the main axes show the electron temperature closer in. Similarly, Figure 17 illustrates the predicted ionization fraction distribution. It shows the effect of the increased population of the free electrons stays very close to the actuator. The inset axes show the full field whereas the main axes show the ionization fraction closer in. These figures do not exhibit significant interaction in terms of the observed acoustic behaviors seen in Figure 15.

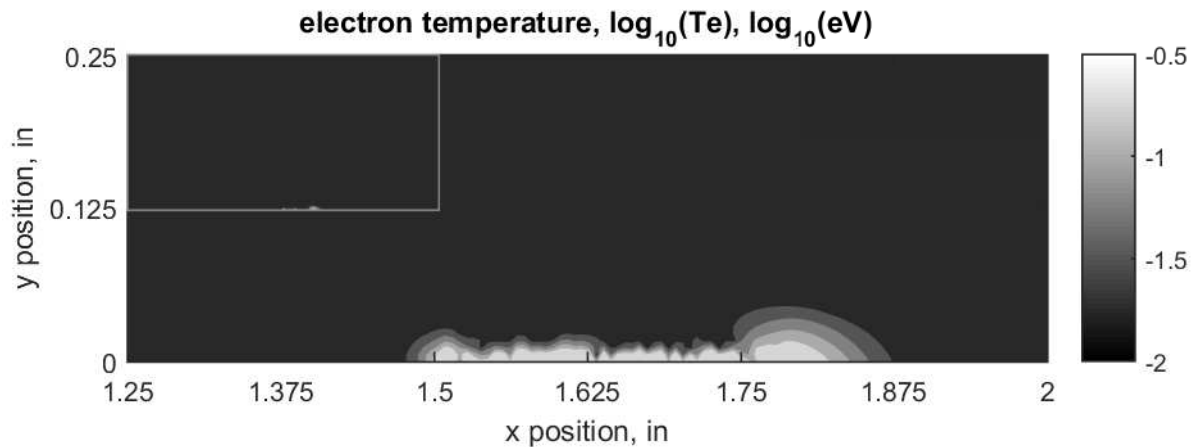**Figure 16:** Example electron temperature results for $5.0 kg/(m^2 - s)$ inflow at $60 \mu s$. The inset axes show the full field whereas the main axes show the electron temperature closer in.

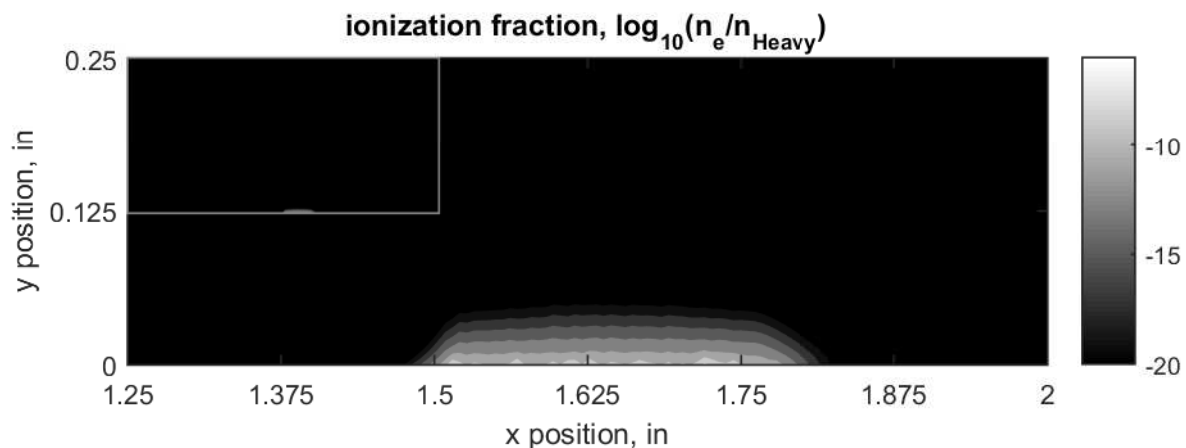**Figure 17:** Example ionization fraction results for $5.0 kg/(m^2 - s)$ inflow at $60 \mu s$. The inset axes show the full field whereas the main axes show the ionization fraction closer in.

49
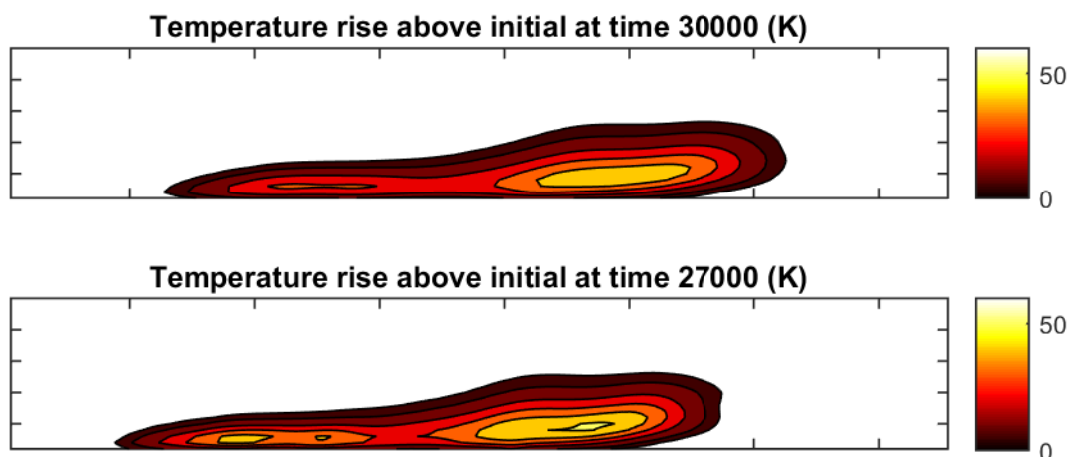
Figure 18: A comparison of computed temperature fields separated by 3000 time steps

5.2.2 Post-Processing Results

To calculate non-acoustic fluid structure movement, two-dimensional cross-correlations of temperature data were taken. Data sets, separated by $N_{sep} = 3000$ time steps ($300\mu s$), give sufficient separation to allow a reasonable measure of the motion. A pair of images can be seen in Figure 18. One can see in these images the motion of two distinct thermal structures coming from the actuator. The temperature data were selected for this analysis because the temperature data is not significantly affected by the acoustic phenomena. In these images, one can note a distinct lack of fronts that would be associated with any acoustic behavior.

Figure 19 shows the histogram of cross-correlated movement in both the x- and y-directions. This histogram shows a mean streamwise shift of $\Delta n_x = 7.56 cells$, and a mean normal shift of $\Delta n_y = 0.1960 cells$. The standard deviations of these are $\sigma_x = 1.749 cells$ and $\sigma_y = 0.508 cells$, respectively. These standard deviations show the variation in large structure convective velocity. The scatter plot shows the relationship between the x- and y- shifts. As the vertical shifts are all one, zero, or negative one, the vertical motion of the structure over the computed time scale is negligible.

The velocity of the fluid structure can be assessed using Equation 5.1 and Equation 5.2,

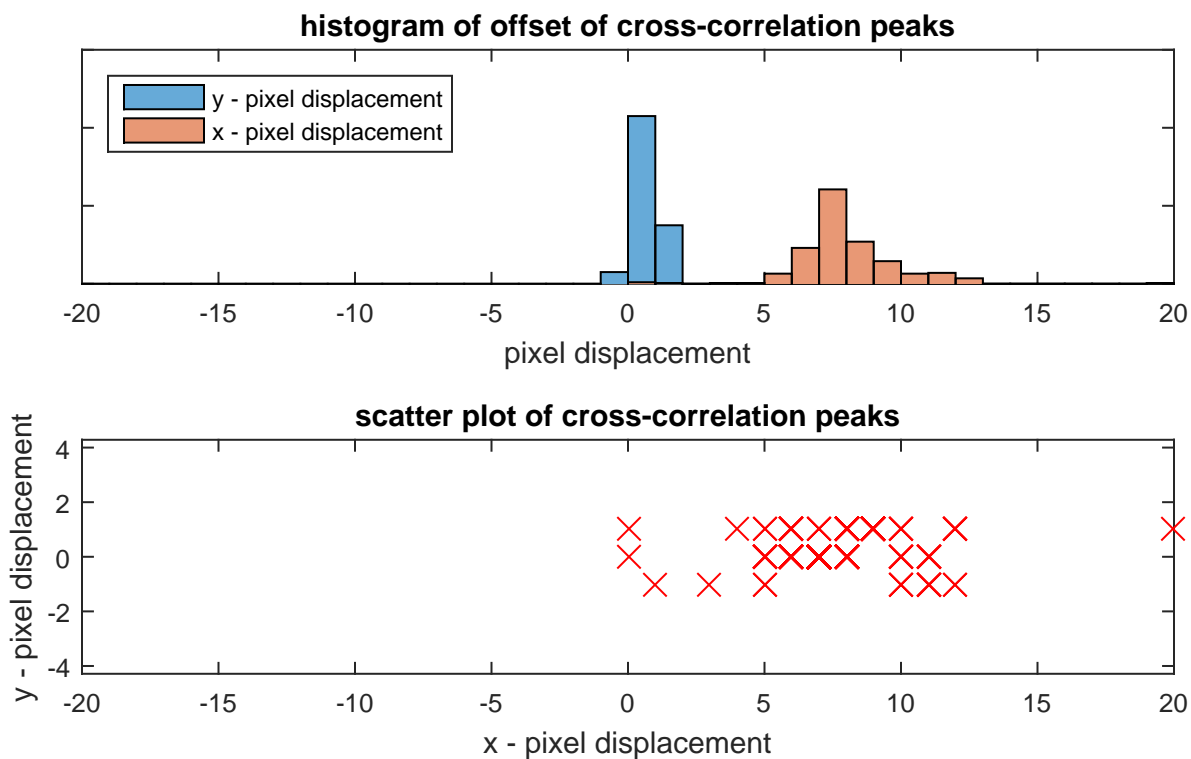**Figure 19:** Histogram and scatter plot of temperature structure motion in x- and y- directions for numerical results

Table 5: Fluid structure motion

	x	y
velocity	3.75 m/s	0.0972 m/s
uncertainty	0.0500 m/s	0.01453 m/s
pct uncertainty	1.333%	14.94%

where $\Delta L = .1488mm$ is the numerical grid size and $\Delta t = 0.1\mu s$ is the simulation time step size. The expected value of the structure velocity from this analysis is, in the streamwise direction, $u = 3.75m/s$, and in the normal direction, $v = 0.0972m/s$. These values will later be compared against experimental values.

$$u = \frac{\Delta n_x \Delta L}{N_{sep} \Delta t} \tag{5.1}$$

$$v = \frac{\Delta n_y \Delta L}{N_{sep} \Delta t} \tag{5.2}$$

The uncertainty of this particular calculation, given the binning associated with the cross-correlation process, is given in Equation 5.3 as adapted from [33], where $N_{samples}$ is the number of cross-correlations performed to get the distribution in Figure 19. This is the same form used in the later processing of the experimental values. The uncertainties determined for the structure velocities are $\Delta u = 0.0500m/s$ in the streamwise direction, and $\Delta v = 0.01453m/s$ in the normal direction. The set of results can be seen in Table 5.

$$\Delta u = \left| \frac{\Delta L}{N_{sep} \Delta t} \frac{\sigma_x}{\sqrt{N_{samples}}} \right| \tag{5.3}$$

Figure 20 shows a histogram of computed electron number densities during the voltage pulse. For each pulse, the number density distribution is similar in shape, with some variation in the number of computational cells involved. This is not unexpected, since minor variations in Debye length will affect the plasma bubble size from pulse to pulse. The electron number
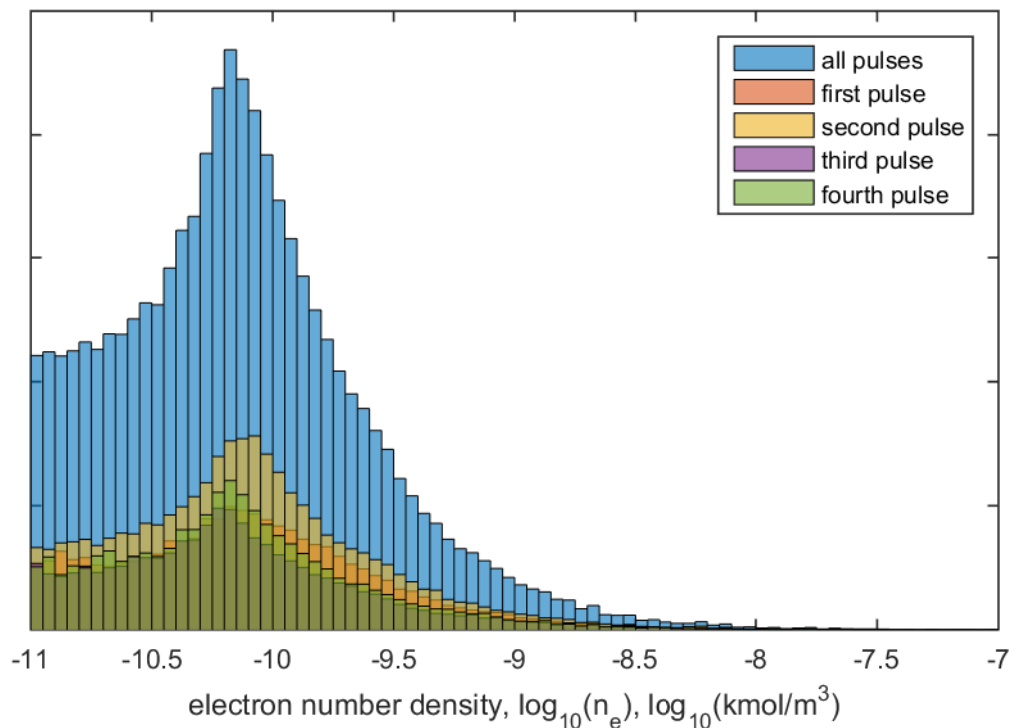
Figure 20: Electron number density histogram over middle 75% of four sequential pulses, and of the combined set. The first and third pulse are very similar to the fourth, and as such are obscured on the histogram

density is cited here as the mode of the distribution. The electron number density over these four pulses is $65.5 \times 10^{-12} kmol/m^3$, and the results for all four pulses can be seen in Table 6. From both the figure and the table, pulse-to-pulse variations can be seen. These variations are caused by hysteresis in the chemistry, meaning the chemistry never fully returns to its initial speciation and distribution.

Figure 21 shows a histogram of computed electron number densities throughout the voltage pulse. The first pulse exhibits much larger counts at lower electron temperatures, as there is no residual shielding from any previous pulse's electrons that had been liberated. Otherwise, the general shape of the histogram is consistent across the pulses. The average electron temperature was computed using a weighted average of the electron number density, as seen in Equation 5.4. The average electron temperature using this method is $0.282eV$, and the

Table 6: Pulse average electron number densities

Pulse index	number density
1	$63.1 \times 10^{-12}\ kmol/m^3$
2	$79.4 \times 10^{-12}\ kmol/m^3$
3	$56.2 \times 10^{-12}\ kmol/m^3$
4	$63.1 \times 10^{-12}\ kmol/m^3$
avg	$65.5 \times 10^{-12}\ kmol/m^3$

Table 7: Pulse average electron temperature

Pulse index	electron temperature
1	$0.236\ eV$
2	$0.257\ eV$
3	$0.350\ eV$
4	$0.285\ eV$
avg	$0.282\ eV$

results for all four pulses can be seen in Table 7.

$$T_{e_{average}} = \frac{\sum\limits_{all\ cells} n_e T_e}{\sum\limits_{all\ cells} n_e} \tag{5.4}$$

The model computes information that allows the determination of the vorticity field, which is useful for determining the quality of the mixing within the flow. Increases in vorticity can be used to enhance flow control. Figure 22 shows the magnitude of the vorticity difference from the initial condition produced by the actuator itself. These differences are computed at a point 75% through each of the four cycles after the applied voltage had settled back to zero. This allows inspection of the persistent structures that exist after the initial acoustic effects have passed. These structures will increase the transport of momentum carrying fluid from further out in the boundary layer down into the lower regions.

This shows that analysis of the results of the model can resolve significant effects that can be difficult to observe experimentally. The model accurately predicts emergent behavior, even
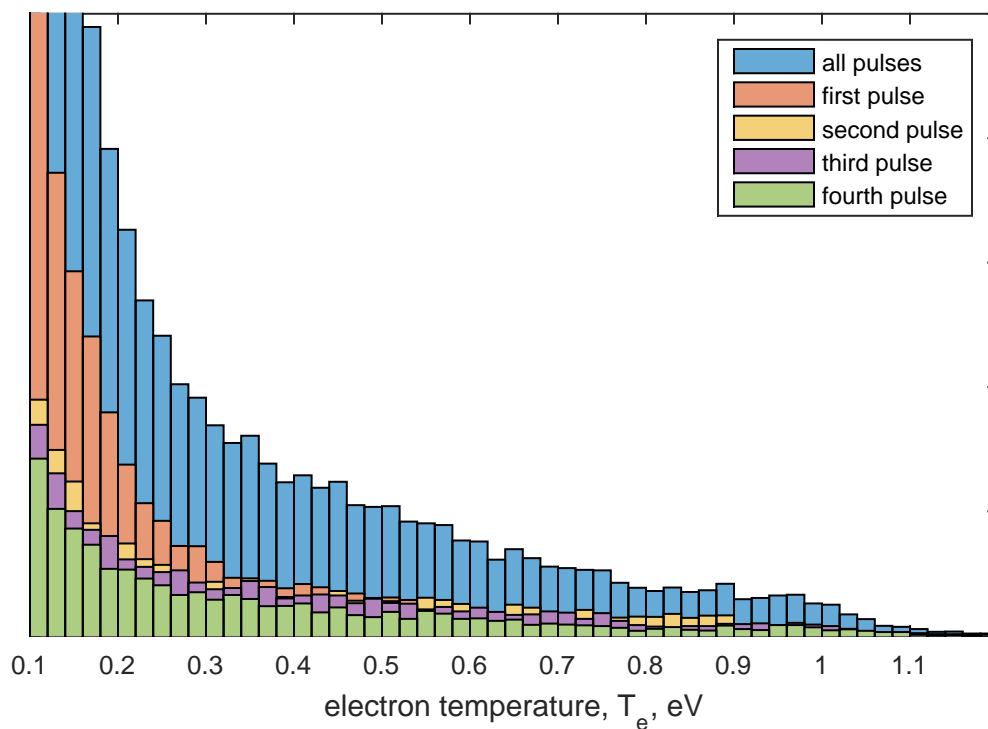
Figure 21: Electron temperature histogram over middle 75% of four sequential pulses, and of the combined set
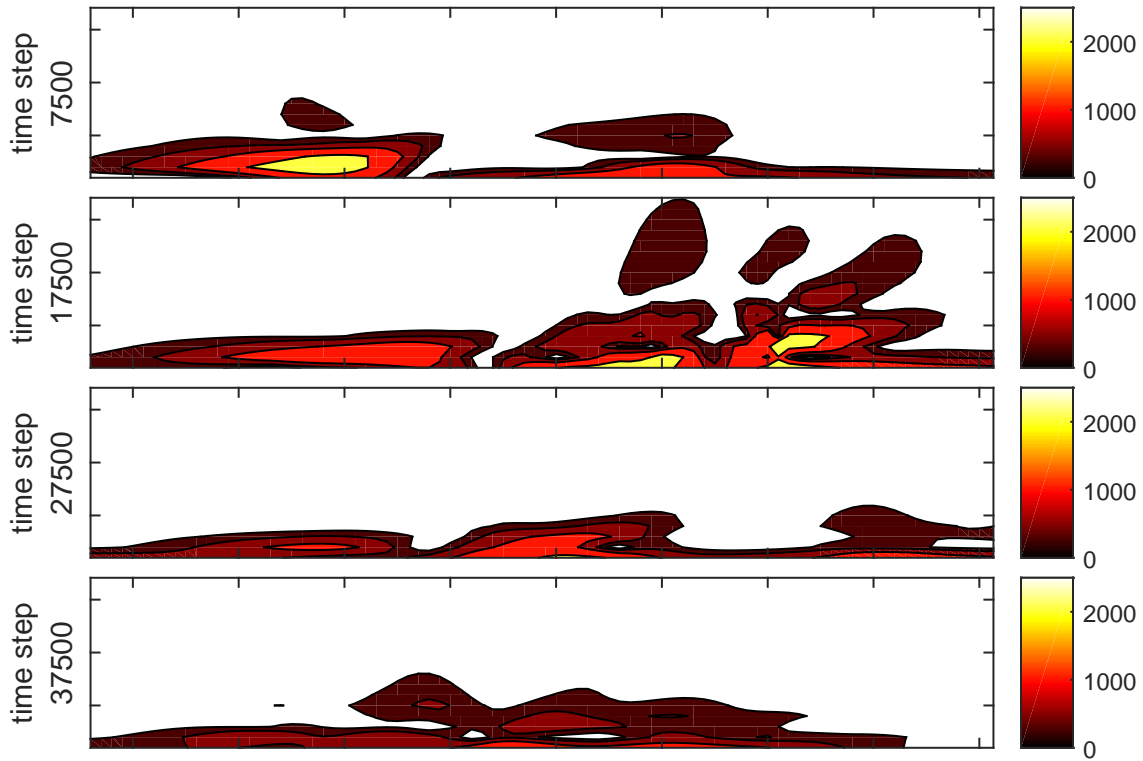
Figure 22: vortical structures produced by each pulse. These contours are vorticity difference from background in units of s^{-1}.

where there is no explicit vorticity source in the governing equations. The coupled physics of the fluid and the plasma employed in the model accurately replicate the perturbation of the boundary layer and the resulting increase in mixing caused by the produced vorticity. The model indicates that the produced vorticity is oriented in the span-wise direction, which will enhance vertical mixing within the boundary layer.

Chapter 6

Experimental Setup

This chapter covers the design of the experiments used to validate the model predictions, which consisted of three major parts. First, the test device consisted of the actuator and the power supply. These parts were used in all experiments. Second, this chapter covers the validation experiments. Finally, the instrumentation used to measure the experiments are discussed.

6.1   Test Device

This section describes the design of the DBD actuator and the power supply used to drive it.

6.1.1   Actuator

The DBD actuator for this experiment is depicted schematically in Figure 23. This is the cross section geometry that was simulated in the numerical model. This actuator design was fabricated using a printed circuit board (PCB) with an FR4 (glass-reinforced epoxy) dielectric. to keep the electrical connections away from the flow control region, the electrode
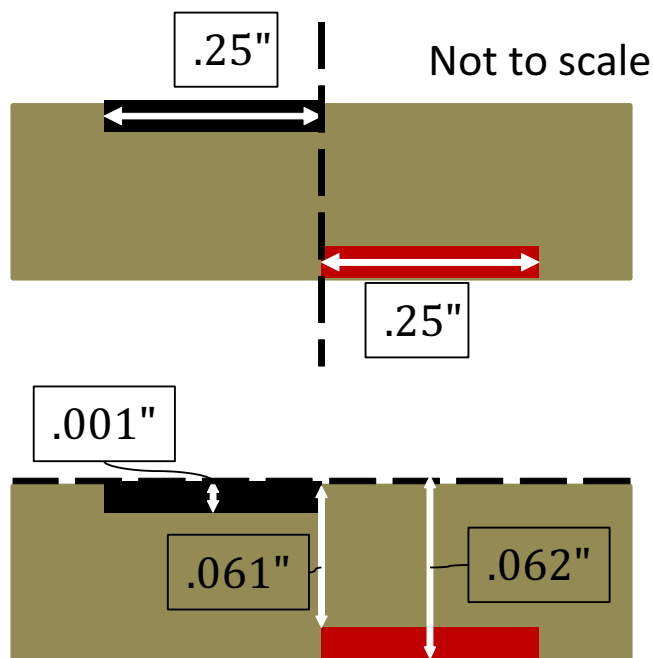
Figure 23: Schematic of the actuator cross-section dimensions at the centerline

connection points were located on the bottom, with internal connections routed to keep the connection points away from the plasma region. A physical specimen of the DBD actuator can be seen in Figures 24 (flow side) and 25 (reverse side).

6.1.2 Power Supply

The power supply for the experiments was built from two automotive capacitive discharge ignition modules. The modules were synchronized using a T-flip flop circuit connected to the desired clock signal generated by the B&K 4030 clock generator. Rectifying diodes were applied prior to the step-up ignition coil. The output of the coil was connected to the actuator. This can be seen schematically in Figure 26. The system created negative voltage pulses. An example measured voltage output trace is shown in Figure 27.
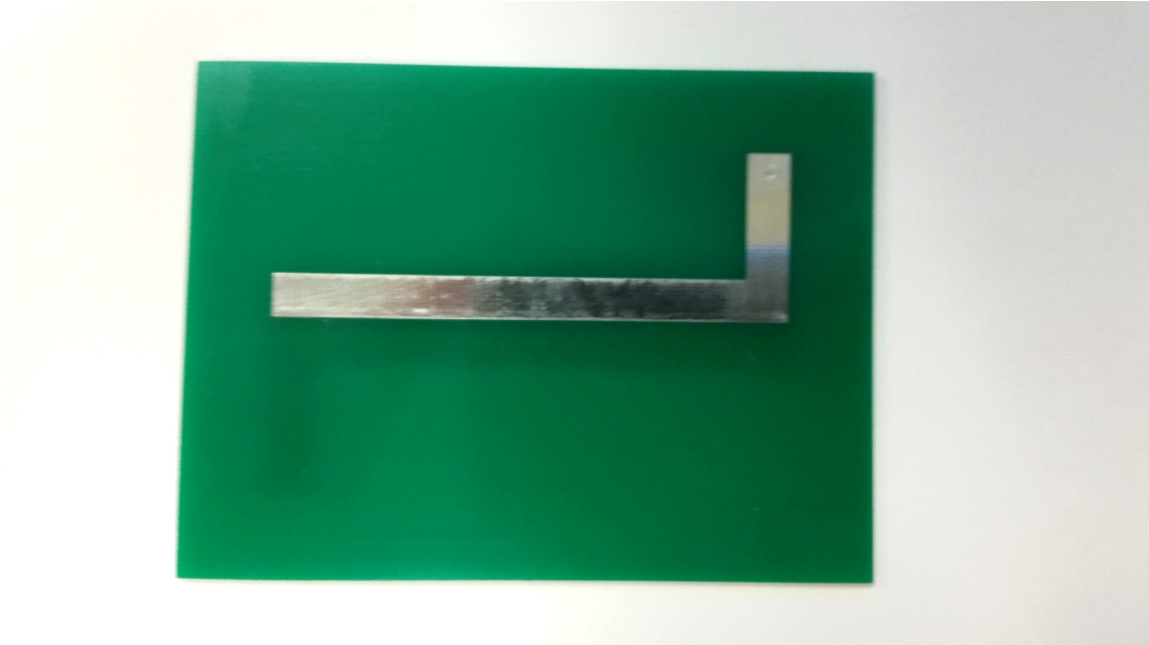
Figure 24: Photograph of the flow side of the PCB actuator (3"x4")
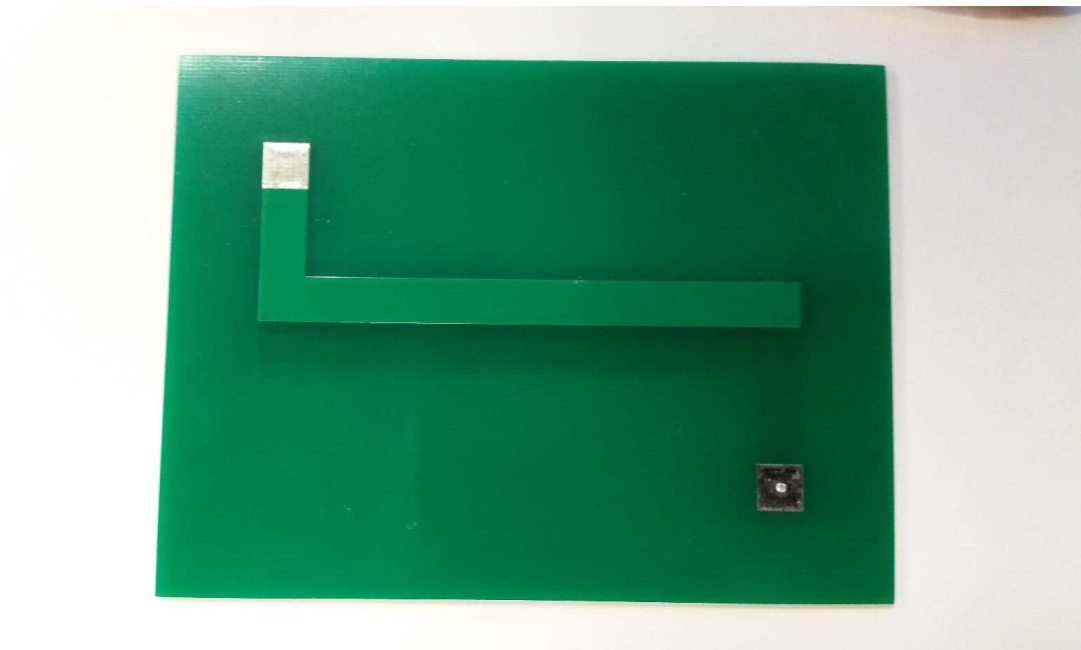
Figure 25: Photograph of the connection side of the PCB actuator (3"x4")

Figure 26: Schematic of the construction of the power supply used to run the actuator
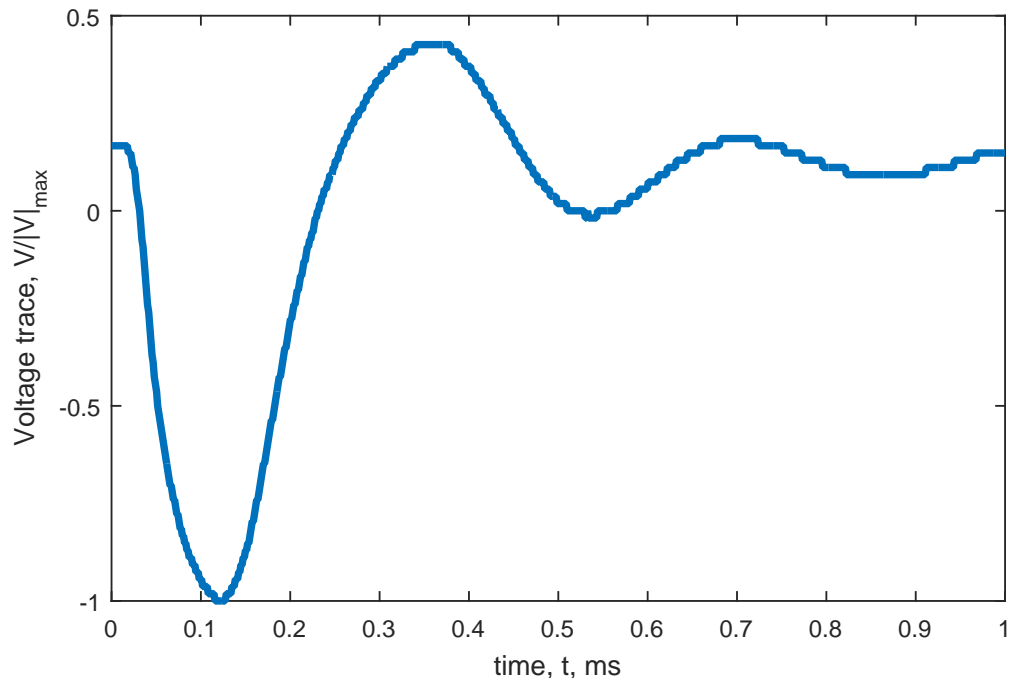
Figure 27: Sample of measured supply output voltage

6.2   Apparatus

This section details the physical apparatus constructed to match the computational model. The experiments demonstrated the effects of the DBD actuator described in Section 6.1 on flow through a passage, as well as the effect of the actuator on the air chemistry.

6.2.1   Flow Passage

The flow passage experiment was designed to observe the effects of the DBD actuator in the presence of flow over its surface. The channel was designed to have the same cross sectional dimensions (3" streamwise direction by 1.5" normal direction) as the computational model, and to have a longer spanwise dimension as a rough approximation to an infinite depth dimension (4"). The semi-infinite assumption was warranted as 4" greatly exceeds the length
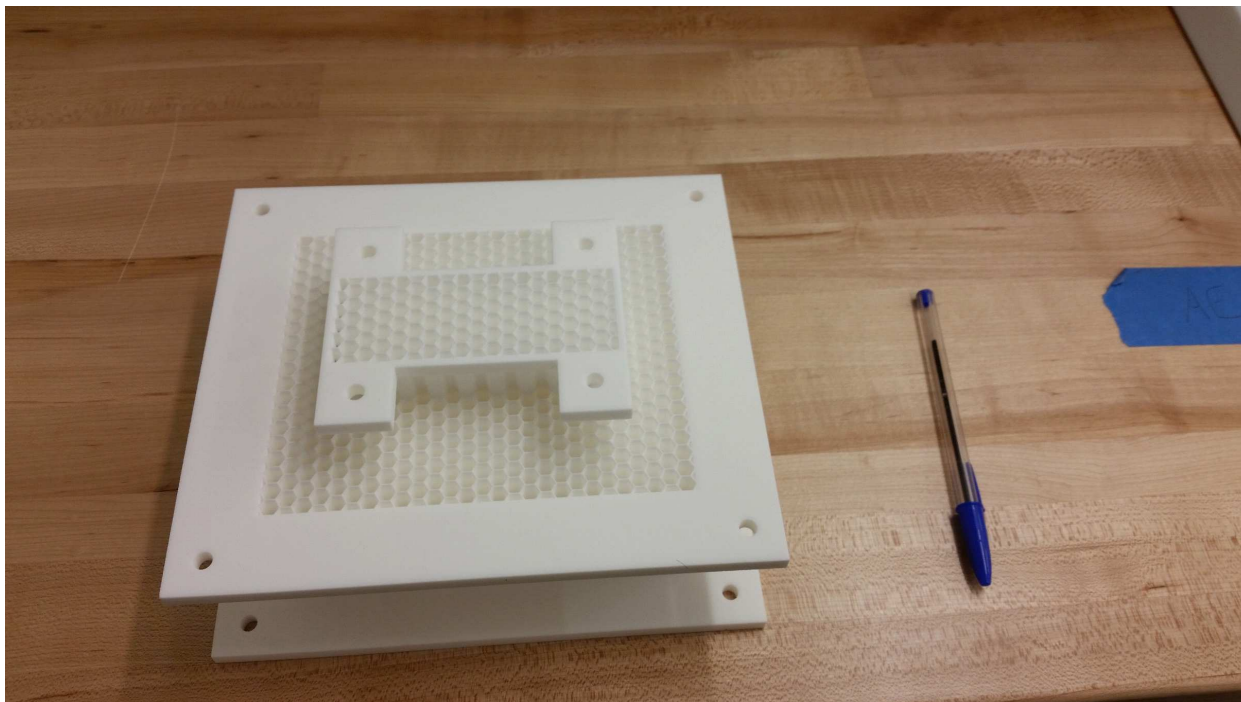
Figure 28: Photograph of the honeycomb (pen for scale)

scales associated with the electric field. The test section itself was attached to a honeycomb (a photograph of which can be seen in Figure 28). The honeycomb was designed to mitigate any downstream flow disruptions from propagating forward into the test section. The honeycomb was also oversized to allow boundary layer air to pass around, rather than be ingested by, the test section. This helped ensure a uniform inflow. In addition to the honeycomb, the inlet to the experiment was an elliptical-to-rectangular converging duct. This ensured that the inflow was subjected to a favorable pressure gradient, thus mitigating possible inflow separations. A photo of this inlet can be seen in Figure 29. An enshrouding cast acrylic transparency section separated the inlet from the test section and the honeycomb. This transparent section was designed to allow the optical measurements to be made. This acrylic spacer had a few penetrations outside of the optical path to allow for power to the electrodes, along with the requisite hosing for the static pressure measurement. The full assembly of this experiment can be seen in Figure 30. A $5hp$ shop-vac vacuum was used to draw air through the test apparatus.
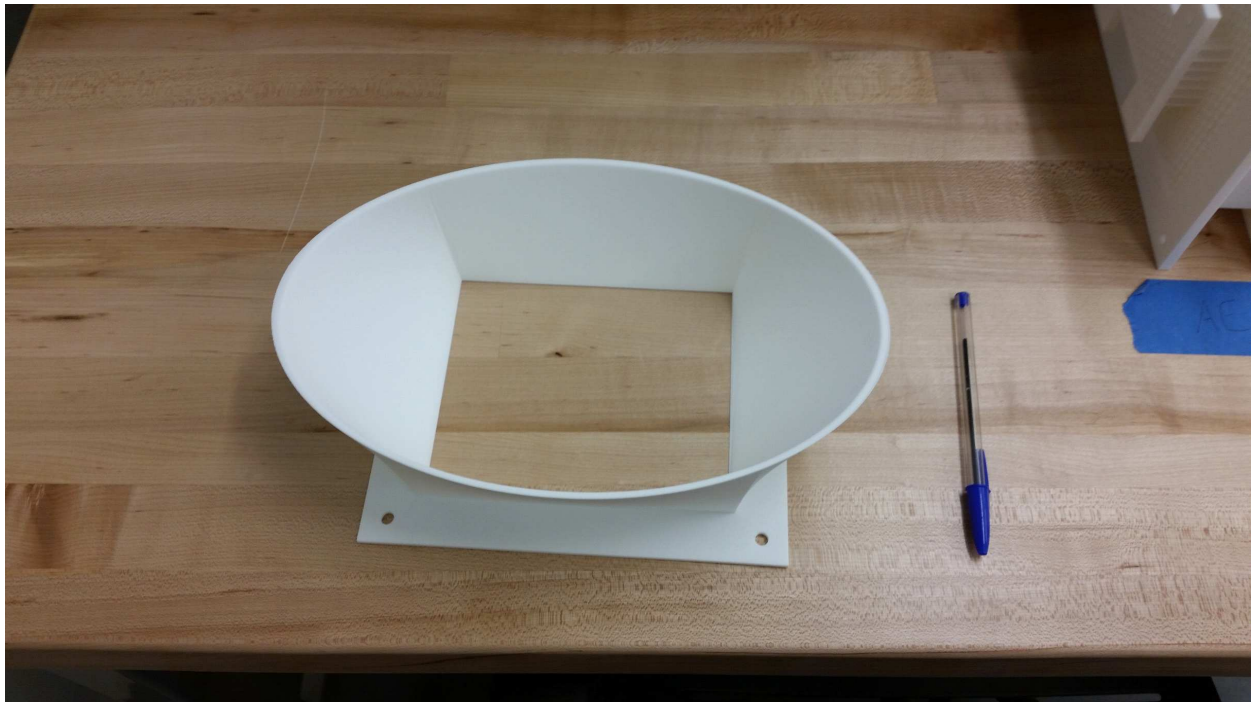
Figure 29: Photograph of the inlet duct (pen for scale)
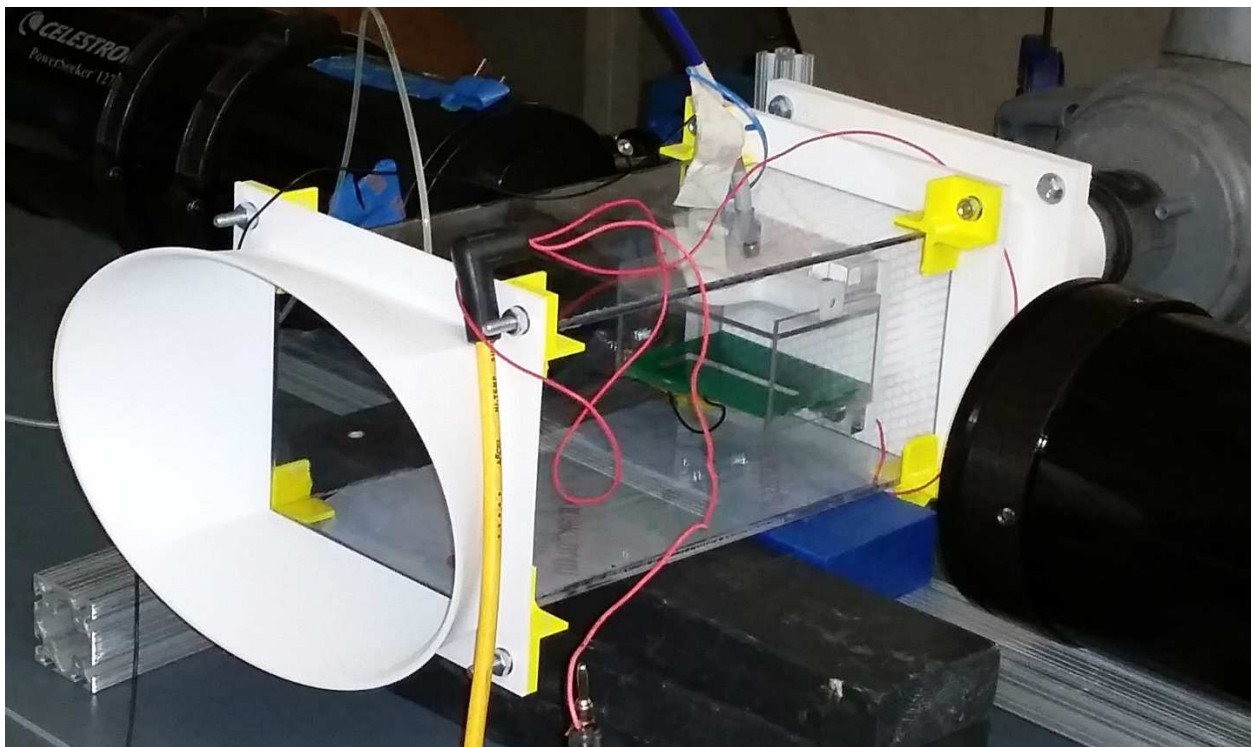
Figure 30: Photograph of the assembled channel-flow experiment

6.2.2   Dark Chamber Spectroscopy

In order to measure the emission spectrum of the discharge, the tests were conducted and experimental data collected in a darkened laboratory. This allowed the spectrometer to more readily reduce ambient light and get a more precise spectrum. Given the dimness of the emission, the spectrometer was set to take data over a 10 second period. The peaks of the spectrum were used to compute electron number densities and electron temperature. Due to the minimal hydrogen content of the air, the relative line method and $N_{2(C-B,0-0)}$ peak intensity metrics were used to compute the electron number densities and electron temperature. A photograph of the spectrometer setup can be seen in Figure 31. In order to accurately observe the plasma, the fiber-optic head of the spectrometer was held in place looking down on the plasma by the plastic structure seen in the figure.

6.3   Instrumentation

This section discusses the several pieces of instrumentation used in the experiments. The basic usage of each follows. The spectrometer was used to confirm the chemical calculations. The shadowgraph was used to confirm the predictions of the numerical model with respect to the flow structure velocity observed in the experiments. A static pressure tap near the inlet of the test section is used to set the flow conditions of the experiment.

6.3.1   Spectrometer

The spectrometer used was an Ocean Optics LIBS2500Plus Laser-induced Breakdown Spectrometer with HR2000+ modules installed. It has a precision of $\pm 0.1nm$ and a spectral range of $200 - 980nm$. The dark noise of the system is $\pm 12counts$. The window of interest for the spectra collected is between $275nm$ and $425nm$. The spectrometer can be seen in Figure 32. Additionally, the associated Mikropack Specline software package was used to
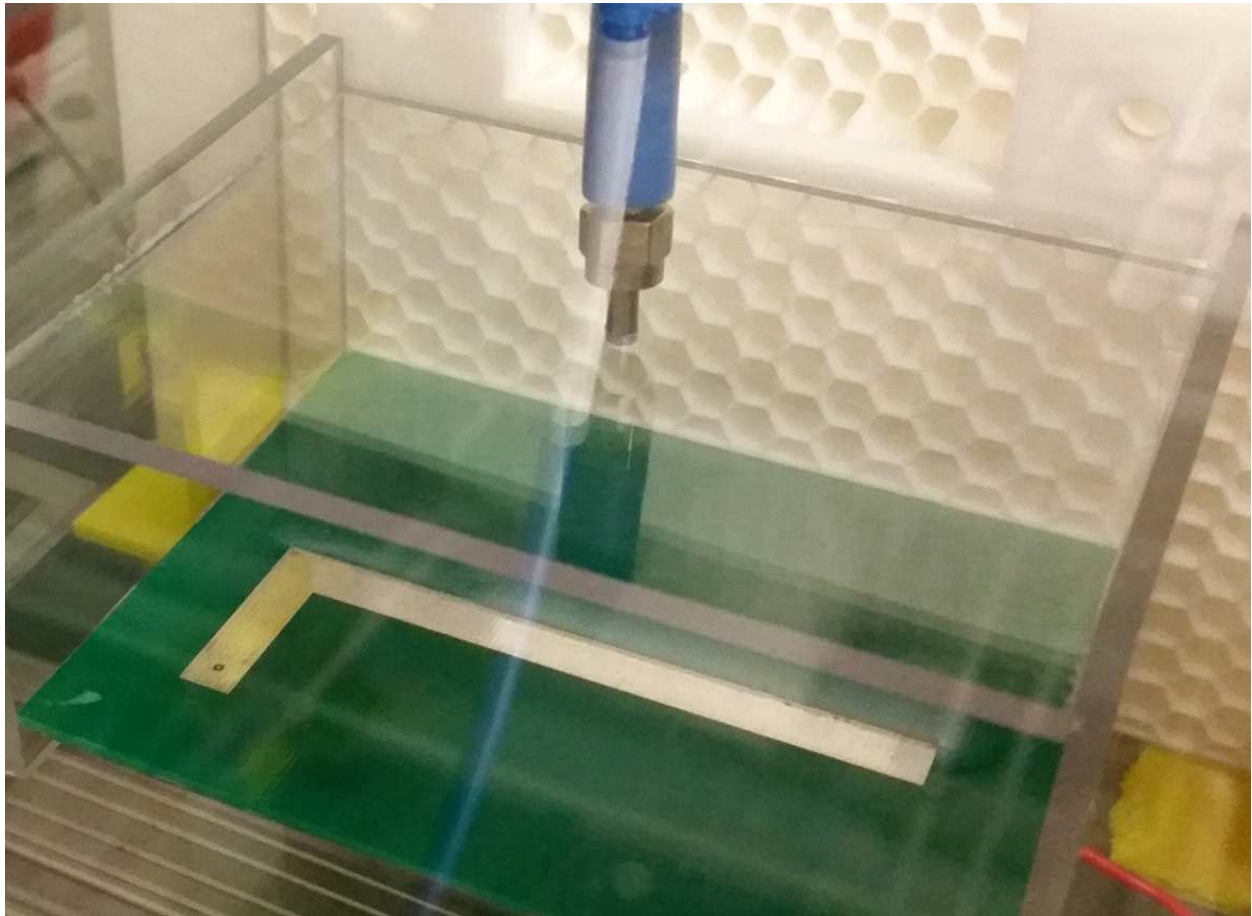
Figure 31: Photograph of the spectrometer fiber optic mounted to a test actuator
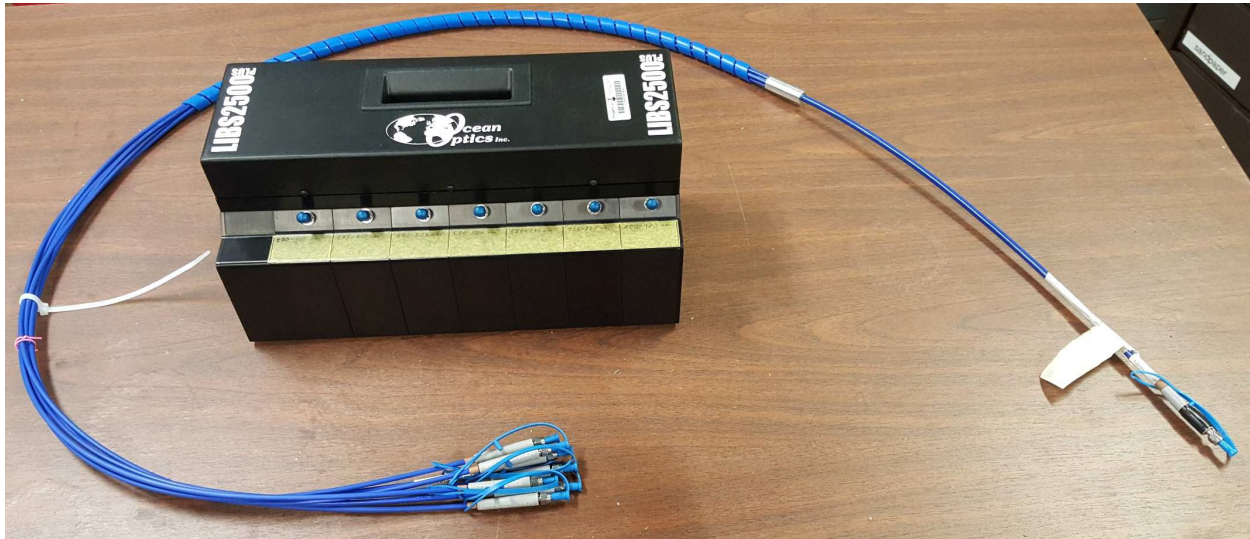
Figure 32: Image of the Ocean Optics LIBS2500Plus spectrometer

analyze the raw spectral data to determine the constituencies in each peak.

6.3.2   Shadowgraphy

The shadowgraph experiment requires an optical assembly consisting of a light source, optics
to collimate the light, optics to focus the light after it passes through the flow, and a high
speed camera to record the shadowgraphed images. A schematic of this system can be seen
in Figure 33. In order to get a field of view large enough, the collimation and focusing optics
were both selected as Celestron 127EQ PowerSeeker telescopes. These provide a 12.7cm
(5in) diameter field of view, thus imaging the whole flow area. They were aligned using a
section of 8020 rail, with finer positioning done with shim material. The light source was
selected as a bright flashlight, which was assembled into a PVC housing with a pinhole that
enabled it to approximate the required point light source. The PVC housing was attached to
the focuser of the collimating telescope. The camera selected was a Edgertronic High Speed
Camera. It had a maximum resolution of 1008x1264 at 500 frames per second. This setting
was used for all the data acquisition. The camera was adapted to connect to the focusing
telescope using a Nikon T-ring adapter. The camera was setup with a pre-filled trigger of

Light refracting flow structures inside test section

telescope as receiver

telescope as light collimator

Edertronic High Speed Camera

Flat plate

Light source
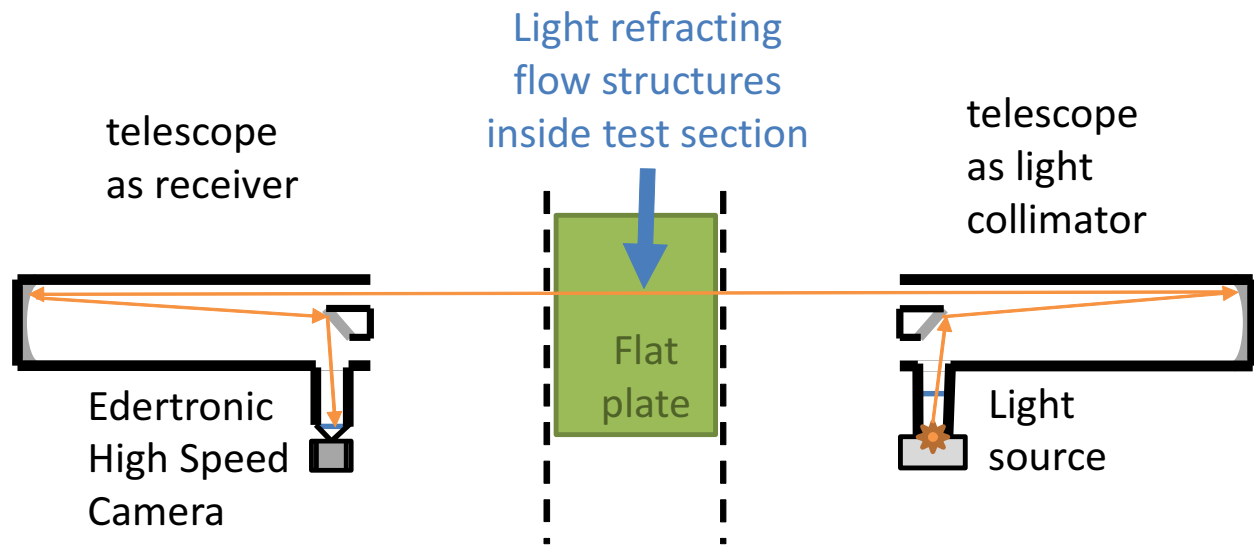
Figure 33: Schematic of the shadowgraph setup

0.25 seconds. This provides 0.25 seconds of no actuation for reference in post processing.

6.3.3   Additional Instrumentation

The high voltage probe used to measure the actuator applied voltage was a Tektronix P6015A. It was connected to a Tektronix TPS2024B oscilloscope, from which the voltage traces could be saved. An example output from this combination was seen in Figure 27.

The manometer used to measure the inlet static pressure was a Dwyer Model 400. This u-tube manometer was selected to avoid interference from the power supply on an electronic manometer. It had $0.005 in - H_2O$ instrument resolution. Unfortunately, at low pressures, the data returned from this instrument had significant uncertainties in estimation of flow speed, thus these measurements will only be used in characterizing the approximate inflow.

Table 8: Shadowgraph Test Conditions

Variac Setting	*Inlet Pressure*
80%	$-0.1in - H_2O$
60%	$-0.06in - H_2O$
40%	$-0.035in - H_2O$
20%	$-0.01in - H_2O$
10%	$-0.005in - H_2O$

6.4 Test Conditions

The flow tests were conducted at various power-settings on the vacuum. These were selected to match to inlet static pressure values in Table 8. The camera took shadowgraph images at $497Frames/second$ with an ISO gain of 1600. The B&K 4030 clock generator output a fixed clock signal from a $1kHz$ crystal to minimize clock drift. This clock signal controlled the power supply.

The spectroscopy was conducted on three runs each on the actuator at 10% intervals on the variac setting. Run indicies 1 through 21 were removed as they were used for setup and targeting, and 38 was removed due to a spectrometer malfunction. The remaining sets were conducted with a power supply clock of $1kHz$, and with spectrometer integration times set to $10s$, as noted in Table 9. Further analysis of the results beyond the scope of this work was conducted in [19].

Table 9: Spectroscopy Test Conditions

Run Index	*Variac Setting*
22	0%
23	80%
24	80%
25	80%
26	50%
27	50%
28	50%
29	40%
30	40%
31	40%
32	30%
33	30%
34	30%
35	20%
36	20%
37	20%
39	10%
40	10%
41	10%
42	60%
43	60%
44	60%
45	70%
46	70%
47	70%

Chapter 7

Experimental Results

The experimental measurements validated both the fluid and chemistry computational models. The high-speed camera produced shadowgraphs that were used to determine the flow behaviors. The spectrometer produced spectral data that was post-processed to compute time-averaged electron temperatures and number densities. An image of the discharge can be seen in Figure 34. The plasma is very uniform, with some periodic "hot spots" along the actuator that coincide with ridges in the substrate that resulted from the manufacturing process. This indicates that the 2-D modeling approximation is acceptable.

7.1 Fluids: Shadowgraphy

The shadowgraphs taken in the experiments were post-processed to mitigate noise in the image through time averaged background subtraction. Example raw frames from the data can be seen in Figure 35, with the left frame showing no actuation and the right frame showing actuation. The frame with the actuation shows the heated near-wall flow from the actuator. This heated air provided the change in index of refraction that allowed it to be imaged. The frames were post processed and then cross-correlated to quantify the motion
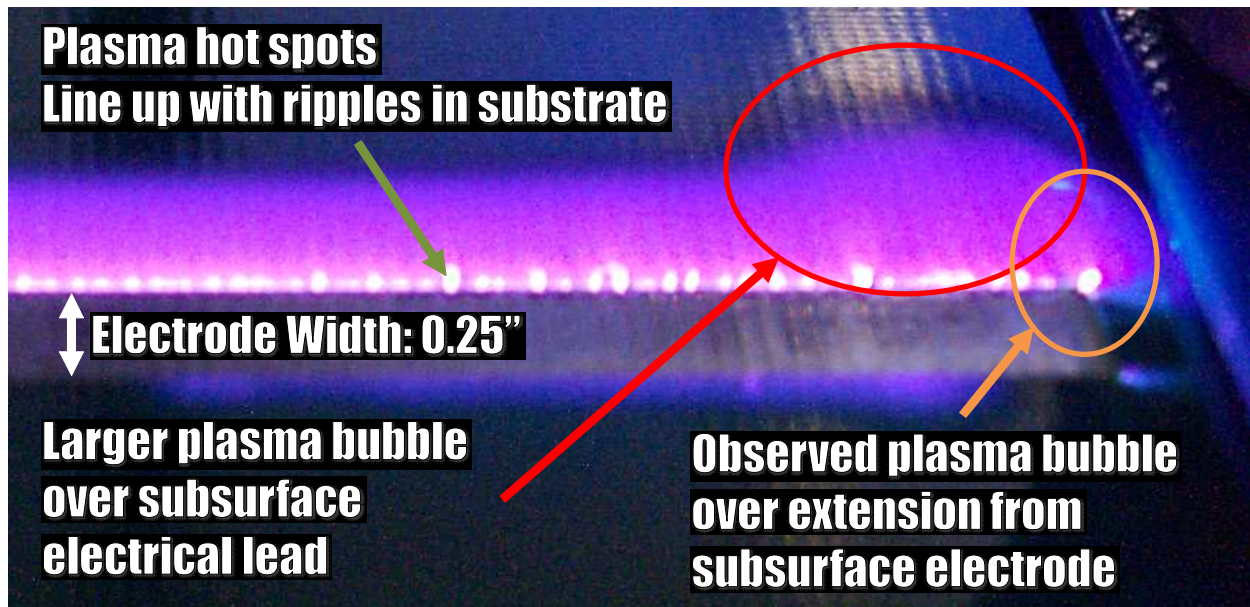
Figure 34: Long exposure photograph of actuator in operation. The plasma is very uniform, with some periodic "hot spots" along the actuator that coincide with ridges in the substrate that resulted from the manufacturing process.

of the refracting fluid structures.

The post processing followed a multi-step approach. First, the region of interest was selected, and a sub-frame was extracted. This extraction is also shown in Figure 35. Then, the pre-trigger sub-frames were averaged to provide a mean frame to be subtracted from the later sub-frames. This enabled the subtraction of the background image with no actuation and provided a set of raw differences that better illustrated the changes that resulted from the actuator. This basic background subtraction can be seen in Figure 36, which clearly shows the actuator's effect on the flow.

In order to track structures that were created by the actuator, the "background" effect on the air was subtracted from the post-actuation subframes as well. This was done by taking the mean of all frames after the starting vortex has passed out of frame and subtracting it from each of those same frames. Two time-adjacent frames are shown in Figure 37. The green, red, and orange arrows show an estimated transport of light-refracting flow structures. Further processing quantified the actual relative motion of the structure.
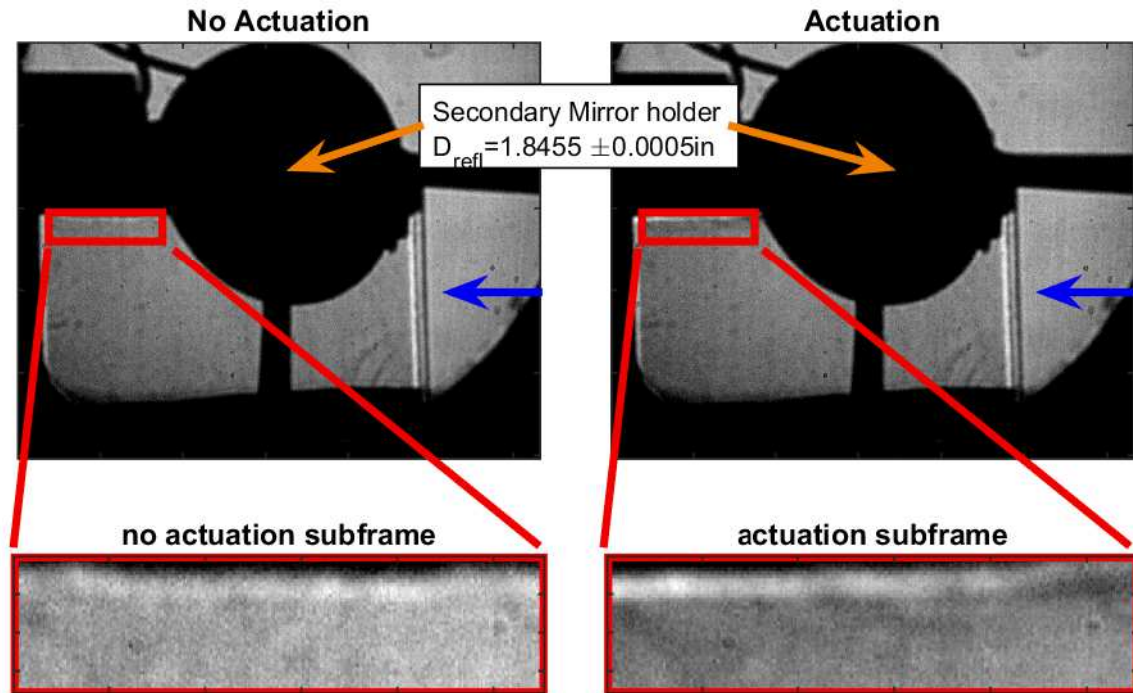
Figure 35: Raw images from shadowgraph imagery, with the left frames showing no actuation and the right frames showing actuation, and the blue arrows indicating flow direction
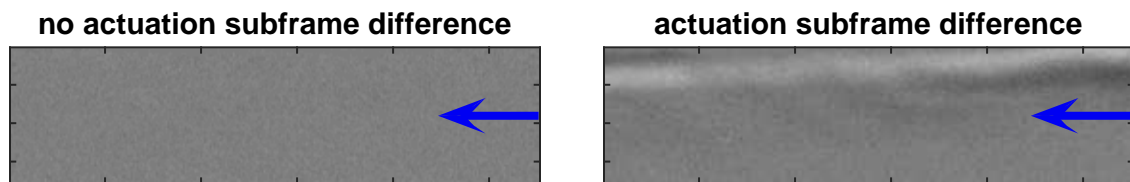
Figure 36: Shadowgraph images with the pre-actuation background subtracted out. The blue arrow indicates the flow direction

73
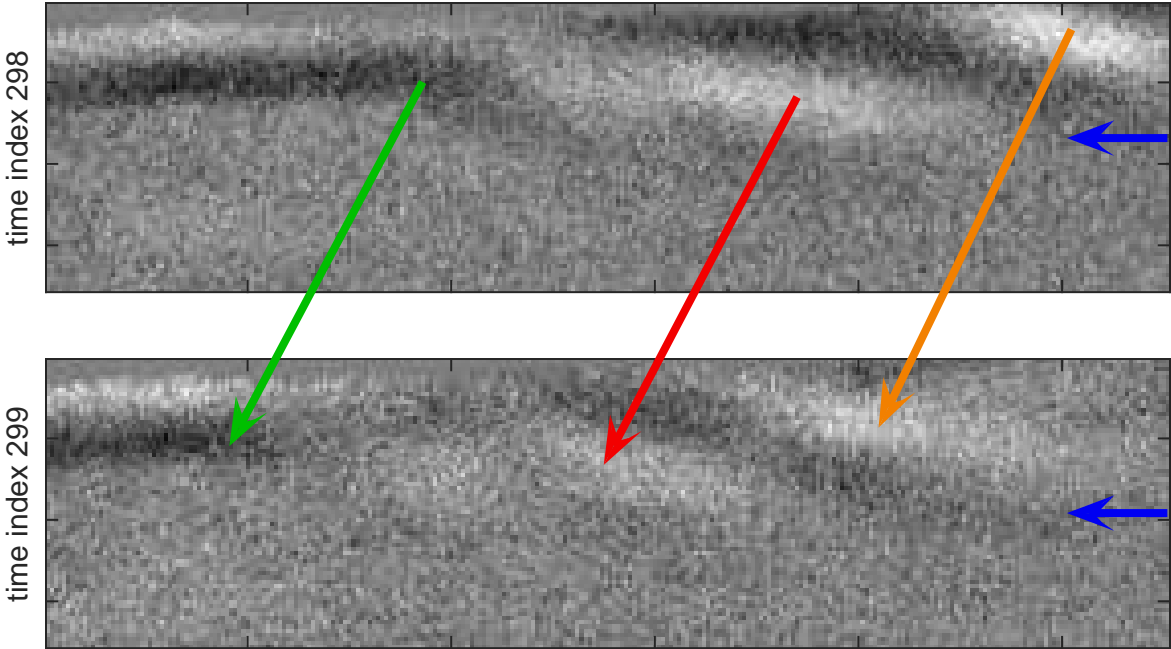
Figure 37: Time-adjacent shadowgraph images with the baseline actuation effect removed. The green, red, and orange arrows show approximate structure motion, and the blue arrows indicate flow direction
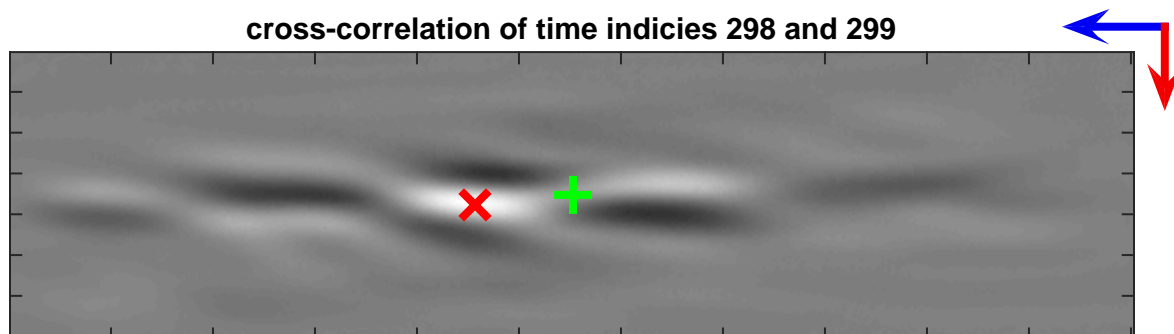
Figure 38: Time-adjacent shadowgraph images cross-correlated, with the maximum marked by the red 'x', and the zero-shift center marked by the green '+'. The blue arrow indicates the direction of a positive shift in the streamwise direction, and the red arrow indicates the direction of a positive shift in the wall normal direction relative to the green '+'.

A more precise method of determining the motion of the flow structures in the images is the 2D cross-correlation. Figure 38 shows the resulting cross-correlation matrix of two time-adjacent frames. The maximum value of the cross-correlation is off-center in both directions. The deviation from center shows the number of pixels that the flow structures moved.

This procedure was repeated over all adjacent frames. Some frames showed weak responses that gave spurious results. These were detected as outliers or very weak cross-correlation peaks and removed from the data set. This final set of deviations were grouped to give a statistical view of the fluid is motion. Figure 39 shows the histogram of results for the a shadowgraph video of the flow with an inlet static pressure of $-0.005in - H_2O$). Figure 40 shows the histogram and scatter for the case with an inlet static pressure of $-0.01 - in - H_2O$. Figure 41 shows the the histogram and scatter for the case with an inlet static pressure of $-0.035 - in - H_2O$. These results were processed into velocity data in Table 10. As the speed increases, the scatter in results increases. At higher speeds, the results become unusable because the structures are frequently not captured in sequential frames.

The frame rate and resolution were used to convert these pixel shifts to velocities. The camera recorded the highest maximum-resolution sample rate of $F_s = 498 \pm 1$ frames per second. The resolution was determined by counting the number of pixels the images had across a structure
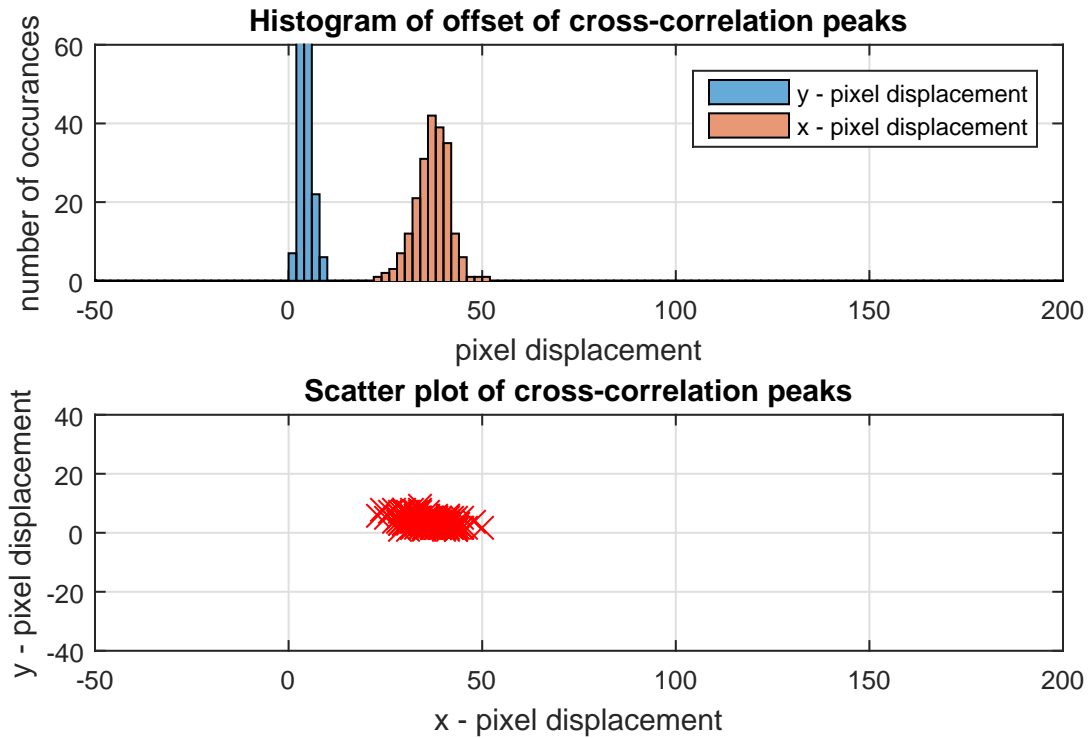
Figure 39: Histogram and scatter plot of 2-D cross correlation of shadowgraph frames with their preceding frame with the variac set to 10%
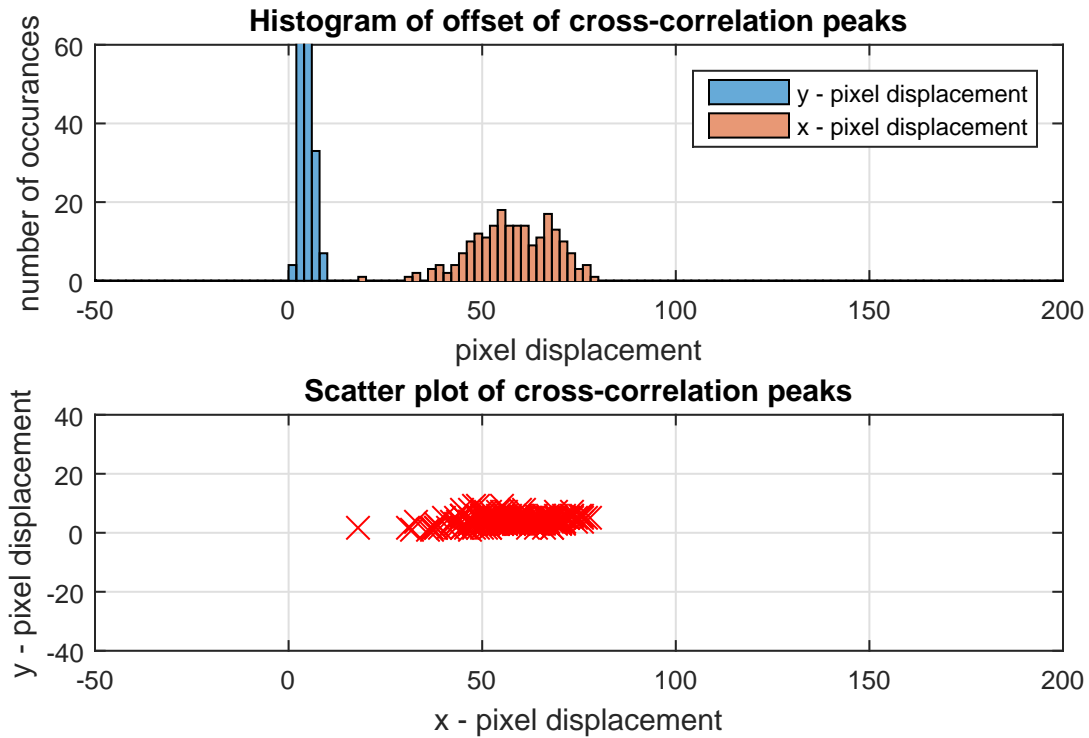
Figure 40: Histogram and scatter plot of 2-D cross correlation of shadowgraph frames with their preceding frame with the variac set to 20%
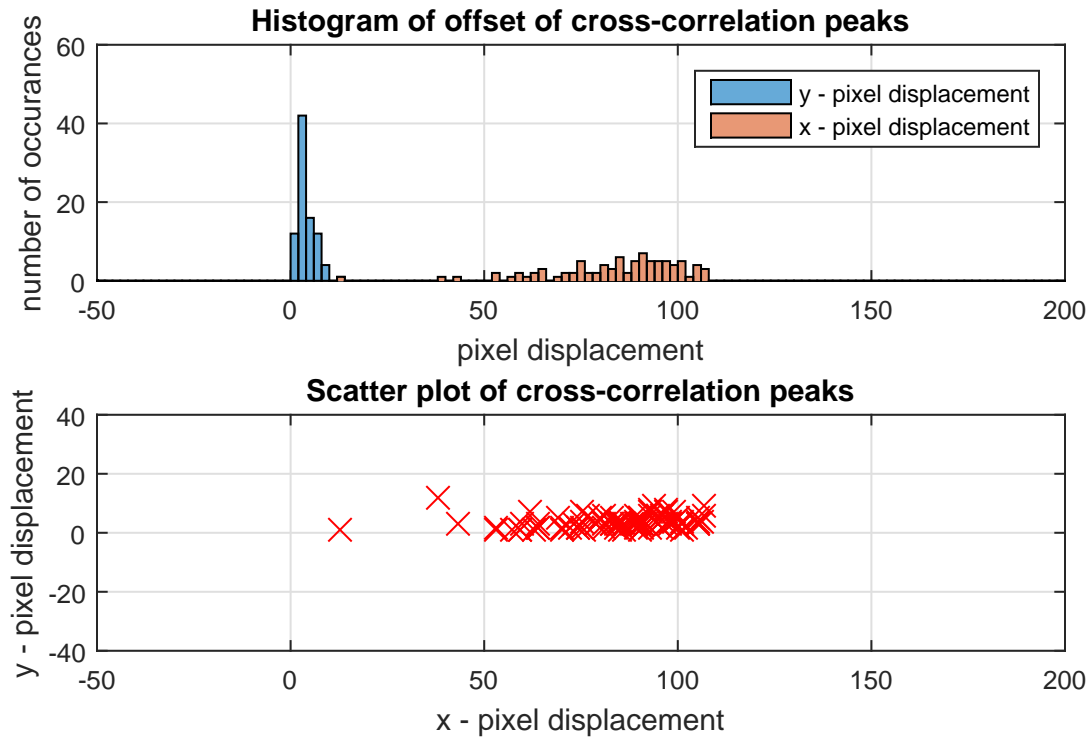
Figure 41: Histogram and scatter plot of 2-D cross correlation of shadowgraph frames with their preceding frame with the variac set to 40%

of known size. The diameter of the secondary reflector holder was $D_{refl} = 1.8455 \pm 0.0005in$ in diameter, and is easily the largest, most easily identified structure in the image. The image was $N_{refl} = 577 \pm 10 pixels$ across. The calculation of the velocity represented by a given cross-correlation peak shift is shown in Equations 7.1 and 7.2.

$$u = F_s \Delta n_x \frac{D_{refl}}{N_{refl}} \tag{7.1}$$

$$v = F_s \Delta n_y \frac{D_{refl}}{N_{refl}} \tag{7.2}$$

The uncertainty of the velocity components was computed for each valid cross-correlation peak offset using Equations 7.3 and 7.4. In these equations, ΔF_s is the above stated frame rate uncertainty, ΔD_{refl} is the above stated uncertainty in the diameter of the secondary reflector, ΔN_{refl} is the above state uncertainty in the number of pixels imaged across the secondary reflector, and $\sigma_{\Delta n_x}/\sqrt{N_{valid}}$ and $\sigma_{\Delta n_y}/\sqrt{N_{valid}}$ are the standard deviations of the accepted cross-correlation peaks divided by the square root of the number of accepted cross-correlation peaks. The uncertainty of the pixel motion treated each cross-correlated image pair as an independent test, and thus this formulation was used [33].

$$\Delta u = \sqrt{\left(\frac{\partial u}{\partial \Delta n_x} \frac{\sigma_{\Delta n_x}}{\sqrt{N_{valid}}}\right)^2 + \left(\frac{\partial u}{\partial F_s} \Delta F_s\right)^2 + \left(\frac{\partial u}{\partial D_{refl}} \Delta D_{refl}\right)^2 + \left(\frac{\partial u}{\partial N_{refl}} \Delta N_{refl}\right)^2} \tag{7.3}$$

$$\Delta v = \sqrt{\left(\frac{\partial v}{\partial \Delta n_y} \frac{\sigma_{\Delta n_y}}{\sqrt{N_{valid}}}\right)^2 + \left(\frac{\partial v}{\partial F_s} \Delta F_s\right)^2 + \left(\frac{\partial v}{\partial D_{refl}} \Delta D_{refl}\right)^2 + \left(\frac{\partial v}{\partial N_{refl}} \Delta N_{refl}\right)^2} \tag{7.4}$$

Table 10 contains a summary of the computed results from the shadowgraph images. As expected, the measured pressure has a high relative uncertainty due to the low speed of

Table 10: Summary of shadowgraph test results

Variac pct	Quantity	Units	Value	Uncertainty	Unc. pct
all	F_s	$frames/sec$	498	± 1	0.201%
all	D_{refl}	in	1.8455	± 0.0005	0.0271%
all	N_{refl}	$pixels$	577	± 10	1.733%
10%	P	$in - H_2O$	-0.005	± 0.005	100.0%
10%	u	m/s	1.485	± 0.0286	1.926%
10%	v	m/s	0.1505	± 0.00587	3.90%
20%	P	$in - H_2O$	-0.010	± 0.005	50.0%
20%	u	m/s	2.32	± 0.0500	2.16%
20%	v	m/s	0.1707	± 0.00708	4.15%
40%	P	$in - H_2O$	-0.035	± 0.005	14.29%
40%	u	m/s	3.38	± 0.0946	2.80%
40%	v	m/s	0.1470	± 0.01195	8.13%

the flow. This value is not directly used in any calculations, but it is acceptable as an order-of-magnitude characterization of the current flow condition of the test article. The calculated uncertainties on the velocities are mostly between $2-5\%$, with the exception of the highest speed normal velocity component. This is due to the lower count of accepted cross-correlation peak offsets.

7.2   Chemistry: Spectroscopy

The spectra were processed using the relative line method and an absolute intensity transition method to compute electron temperatures and number densities. An example spectrum can be seen in Figure 42. The peaks of the N_2 second positive set of transitions are readily identified.

These data were used with the formulation in Equation 2.3 to compute the electron temperature. The transitions used to compute the electron temperatures were the $N_{2(B-C,0-0)}$ transition at a wavelength of $336.9nm$ and the $N_{2(B-C,0-1)}$ transition at a wavelength of $315.7nm$. The intensity values were integrated over a bandwidth of $\pm 2nm$ for both peaks.
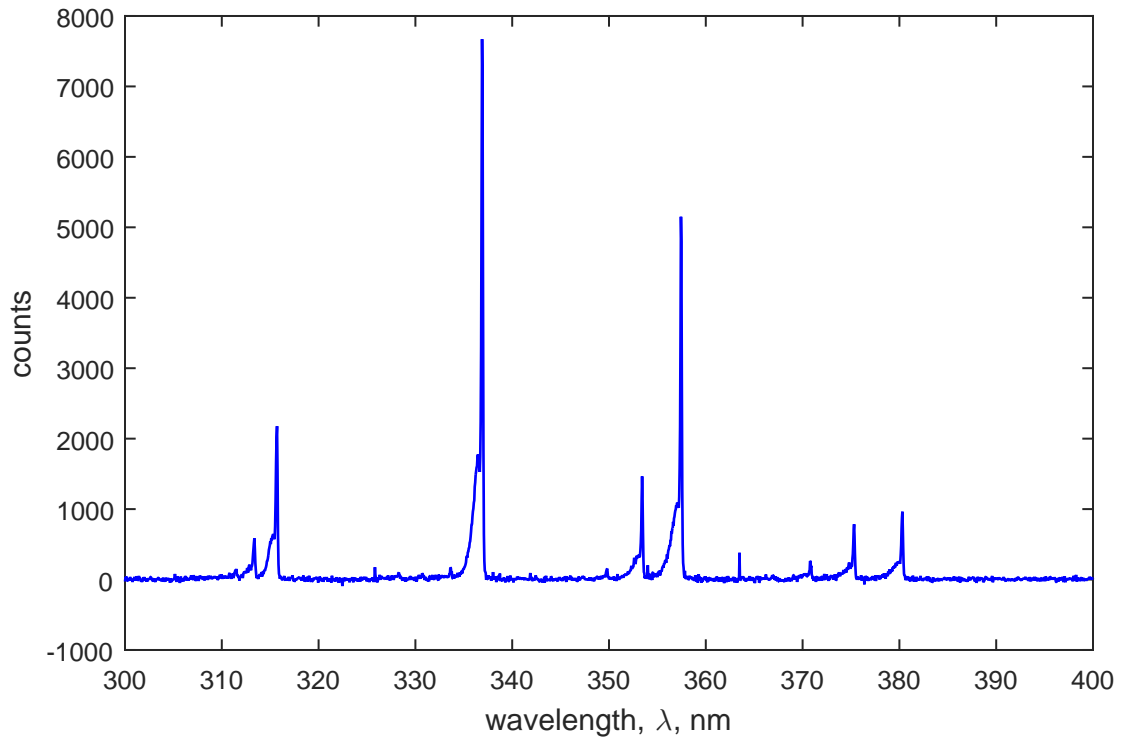
Figure 42: Sample emission spectrum for discharge with the vacuum at 40% (case 29)

The first column in Table 11 shows the computed electron temperatures. The average of the electron temperature across all runs computed in this manner is $T_e = 0.251eV$. Given the variety of possible influences on the quality and intensity of the spectral peaks, a formal determination of uncertainty is intractable. However, reference [8] indicates that for the relative line method an uncertainty of approximately 10% is typical.

The electron number density was estimated from these electron temperatures and the integrated photon intensity of the $N_{2(B-C,0-0)}$ transition peak at a wavelength of $336.9nm$ over a $\pm 2nm$ bandwidth as described in Chapter 2. The estimated electron number densities are shown in Table 11. The average of electron number density of these runs is $n_e = 76.9 \times 10^{-12} kmol/m^3$.

Table 11: Electron temperature and number density results, with mean $T_e = 0.251eV$ and $n_e = 76.9 \times 10^{-12} kmol/m^3$

run index	electron temperature	number density
22	$0.250eV$	$60.7 \times 10^{-12}\ kmol/m^3$
23	$0.255eV$	$54.7 \times 10^{-12}\ kmol/m^3$
24	$0.256eV$	$49.6 \times 10^{-12}\ kmol/m^3$
25	$0.242eV$	$57.4 \times 10^{-12}\ kmol/m^3$
26	$0.251eV$	$69.2 \times 10^{-12}\ kmol/m^3$
27	$0.252eV$	$73.3 \times 10^{-12}\ kmol/m^3$
28	$0.252eV$	$71.1 \times 10^{-12}\ kmol/m^3$
29	$0.251eV$	$68.4 \times 10^{-12}\ kmol/m^3$
30	$0.252eV$	$74.3 \times 10^{-12}\ kmol/m^3$
31	$0.253eV$	$76.7 \times 10^{-12}\ kmol/m^3$
32	$0.258eV$	$78.9 \times 10^{-12}\ kmol/m^3$
33	$0.247eV$	$78.2 \times 10^{-12}\ kmol/m^3$
34	$0.249eV$	$80.8 \times 10^{-12}\ kmol/m^3$
35	$0.256eV$	$80.9 \times 10^{-12}\ kmol/m^3$
36	$0.259eV$	$83.4 \times 10^{-12}\ kmol/m^3$
37	$0.250eV$	$83.5 \times 10^{-12}\ kmol/m^3$
39	$0.252eV$	$87.5 \times 10^{-12}\ kmol/m^3$
40	$0.246eV$	$87.7 \times 10^{-12}\ kmol/m^3$
41	$0.249eV$	$84.5 \times 10^{-12}\ kmol/m^3$
42	$0.248eV$	$88.4 \times 10^{-12}\ kmol/m^3$
43	$0.247eV$	$83.8 \times 10^{-12}\ kmol/m^3$
44	$0.249eV$	$88.8 \times 10^{-12}\ kmol/m^3$
45	$0.251eV$	$87.4 \times 10^{-12}\ kmol/m^3$
46	$0.248eV$	$85.8 \times 10^{-12}\ kmol/m^3$
47	$0.252eV$	$87.4 \times 10^{-12}\ kmol/m^3$
avg	$0.251eV$	$76.9 \times 10^{-12}\ kmol/m^3$

Chapter 8

Discussion of Results

8.1 Comparison of Experimental and Numerical Results

This section shows the comparisons between the numerical model and the experimental results. This comparison is shown for the experimental and predicted values of fluid structure velocity, electron temperature, electron number density, and plasma shape.

8.1.1 Fluid Structure Cross-Correlations

The fluid structure velocity represents the motion of larger flow structures within the full flow field. These structures are ascertained within the numerical model as the temperature variations, and within the shadowgraphs as light variations. These are comparable as the index of refraction of a gas is dependent on the density of the gas [10]. Pressure propagates acoustically, and while it would have an effect on the index of refraction of the gas, the time average will be close to zero deviation from the nominal pressure. Temperature, on the other hand, is more slowly transported by convection and diffusion mechanisms. Thus

temperature is a much closer metric for comparison of the large, non-acoustic structures that were observable in the shadowgraphs.

The displacement of the flow structures were computed in Chapters 5 and 7. The measured and predicted velocities compare well. The results are further processed into a scatter plot of velocities in Figure 43. This figure shows that the shadowgraph data exhibits higher resolution on the structure velocity. This is due to the comparatively long time between images. Since each frame is separated by $2ms$, the distance traveled by the structure is far longer covering many more pixels. This compares to the numerical results which were separated by a mere $0.3ms$. The shorter time window compared with coarser resolution causes the noticeably coarser binning of the model results. However, the calculated distributions are qualitatively similar in shape, and the mean velocities fall within the size of the bins of the numerical results. The experiment and model match with a relative error of 10.9% as computed by Equation 8.1.

$$error = 100\% \times \left| \frac{u_{experiment} - u_{model}}{u_{experiment}} \right| \tag{8.1}$$

8.1.2   Electron Temperature

The electron temperature also compared favorably between the experimental calculations and the numerical model. The numerical model's nominal electron temperature was evaluated as a weighted averageof the electron number density over a given peak. The results were originally given in Table 7, and are repeated here in Table 12. The experimental results are compiled in Table 11, and are repeated here in Table 14. The relative error between the mean electron temperature of the experiment and the numerical model is 12.4%. Given the typical experimental uncertainties associated with the relative line method of 10%, this would appear to be a reasonable first-order match.
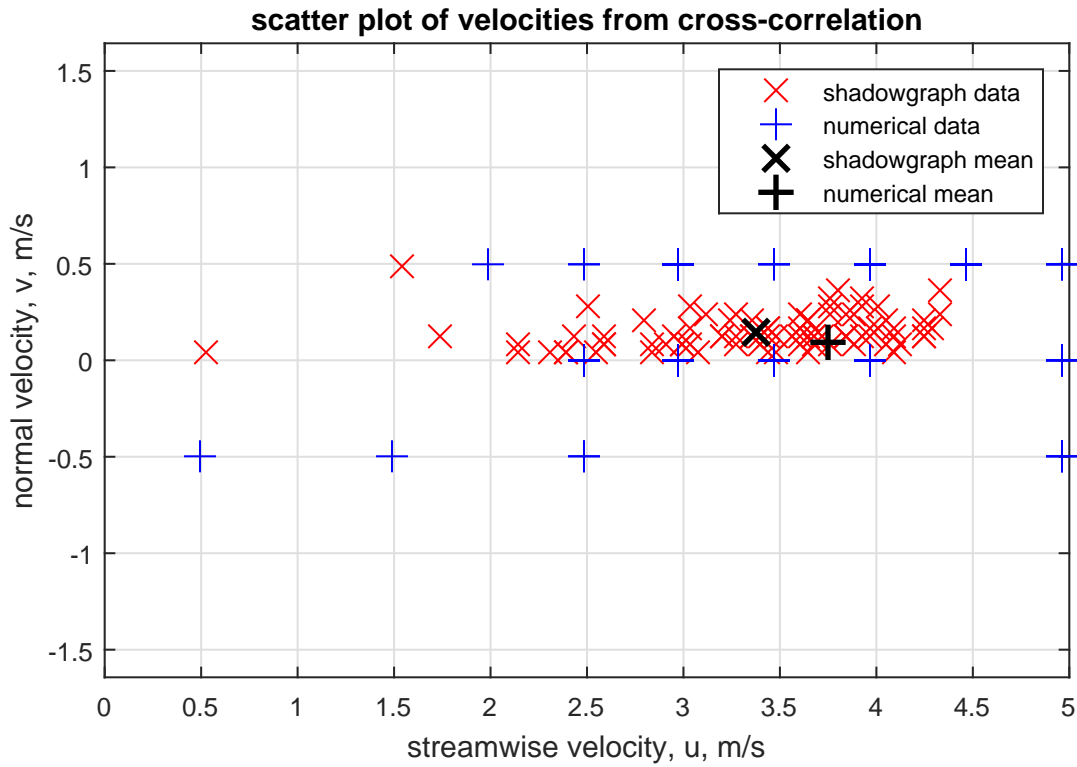
Figure 43: comparison of shadowgraph and numerical data cross-correlation results

Table 12: Pulse average electron temperature for the numerical model

Pulse index	electron temperature
1	0.236 eV
2	0.257 eV
3	0.350 eV
4	0.285 eV
avg	0.282 eV

Table 13: Pulse average electron number densities for the numerical model

Pulse index	number density
1	$63.1 \times 10^{-12} \ kmol/m^3$
2	$79.4 \times 10^{-12} \ kmol/m^3$
3	$56.2 \times 10^{-12} \ kmol/m^3$
4	$63.1 \times 10^{-12} \ kmol/m^3$
avg	$65.5 \times 10^{-12} \ kmol/m^3$

8.1.3 Electron Number Density

The measured electron number densities are comparable to the model predictions. The numerical model's electron number densities were evaluated at the mode of the distribution. The model results were originally given in Table 6, and are repeated here in Table 13. The experimental results were originally given in Table 11, and are repeated here in Table 14. The mean of the model number densities is lower than the measured values, but the distributions overlap. The experimental results fall close to the peak in the number density distribution shown in Figure 44. The relative error between the mean electron number densities of the experiment and the numerical model is 14.8%. Given the comparatively large uncertainties that come with the measured values of the transition probabilities and excitation cross sections [7], and that an absolute intensity method is less accurate than relative intensity measurements, this level of agreement is acceptable.

8.2 Plasma Shape

The plasma bubble shape predicted by the model matches well with long exposure photographic data. Figure 17 showed the predicted contours of ionization fraction, and is repeated here in Figure 45. This contour matches well with the long exposure photograph previously shown in Figure 34, and repeated here in Figure 46. Of particular interest is the qualitatively clean and uniform behavior of the two images, and that the model predicted the

Table 14: Electron number density and temperature results, with mean $T_e = 0.251eV$ and $n_e = 76.9 \times 10^{-12} kmol/m^3$

run index	electron temperature	number density
22	0.250eV	$60.7 \times 10^{-12} \ kmol/m^3$
23	0.255eV	$54.7 \times 10^{-12} \ kmol/m^3$
24	0.256eV	$49.6 \times 10^{-12} \ kmol/m^3$
25	0.242eV	$57.4 \times 10^{-12} \ kmol/m^3$
26	0.251eV	$69.2 \times 10^{-12} \ kmol/m^3$
27	0.252eV	$73.3 \times 10^{-12} \ kmol/m^3$
28	0.252eV	$71.1 \times 10^{-12} \ kmol/m^3$
29	0.251eV	$68.4 \times 10^{-12} \ kmol/m^3$
30	0.252eV	$74.3 \times 10^{-12} \ kmol/m^3$
31	0.253eV	$76.7 \times 10^{-12} \ kmol/m^3$
32	0.258eV	$78.9 \times 10^{-12} \ kmol/m^3$
33	0.247eV	$78.2 \times 10^{-12} \ kmol/m^3$
34	0.249eV	$80.8 \times 10^{-12} \ kmol/m^3$
35	0.256eV	$80.9 \times 10^{-12} \ kmol/m^3$
36	0.259eV	$83.4 \times 10^{-12} \ kmol/m^3$
37	0.250eV	$83.5 \times 10^{-12} \ kmol/m^3$
39	0.252eV	$87.5 \times 10^{-12} \ kmol/m^3$
40	0.246eV	$87.7 \times 10^{-12} \ kmol/m^3$
41	0.249eV	$84.5 \times 10^{-12} \ kmol/m^3$
42	0.248eV	$88.4 \times 10^{-12} \ kmol/m^3$
43	0.247eV	$83.8 \times 10^{-12} \ kmol/m^3$
44	0.249eV	$88.8 \times 10^{-12} \ kmol/m^3$
45	0.251eV	$87.4 \times 10^{-12} \ kmol/m^3$
46	0.248eV	$85.8 \times 10^{-12} \ kmol/m^3$
47	0.252eV	$87.4 \times 10^{-12} \ kmol/m^3$
avg	0.251eV	$76.9 \times 10^{-12} \ kmol/m^3$

Figure 44: Electron number density histogram. Data presented over middle 75% of four sequential pulses, and of the combined set. The first and third pulse are very similar to the fourth, and as such are obscured on the histogram. Of note is that each histogram peak falls between the observed minimum and maximum measured number densities
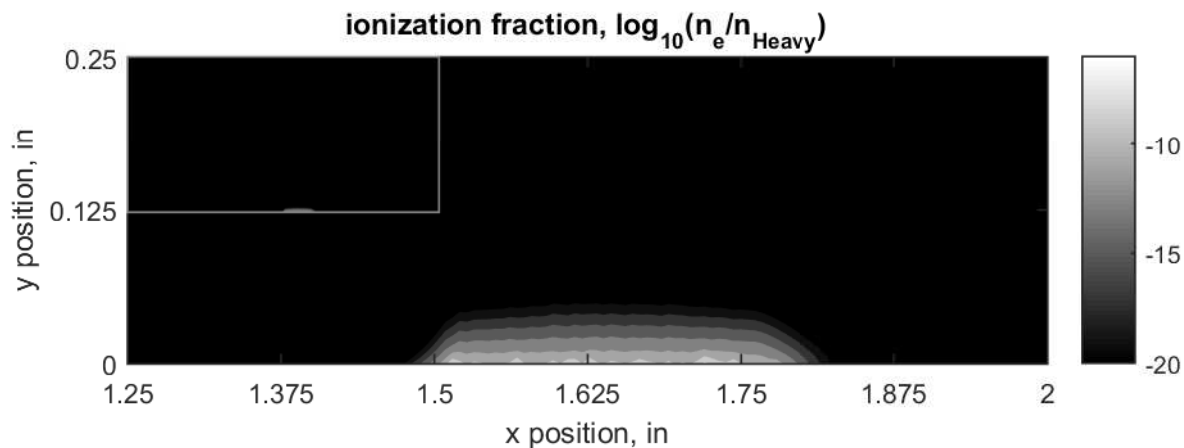
Figure 45: Example ionization fraction results for $5.0 kg/(m^2 - s)$ inflow at $60\mu s$. The inset axes show the full field whereas the main axes show the ionization fraction closer in.

plasma bubble extending somewhat beyond the trailing edge of the subsurface electrode.

8.3 Discussion of Model Results

The model produces a full first order description of the fluid behavior in the presence of an activated DBD flow control actuator. While this does produce some numerical artifacting (namely, numerical diffusion), the results do show the creation of large scale structures in the flow. These structures provide the mechanisms for flow control to occur, and do not rely solely on the direct application of force on the fluid. The modified cellular automata works well and allows easy improvements to the individual "rules" as work continues. Implementation of the model in more complex geometries would allow more study of the specific effects of these structures. Any myriad of analyses could be conducted on the emergent structures of interest, like the vorticity contours presented previously in Figure 22.
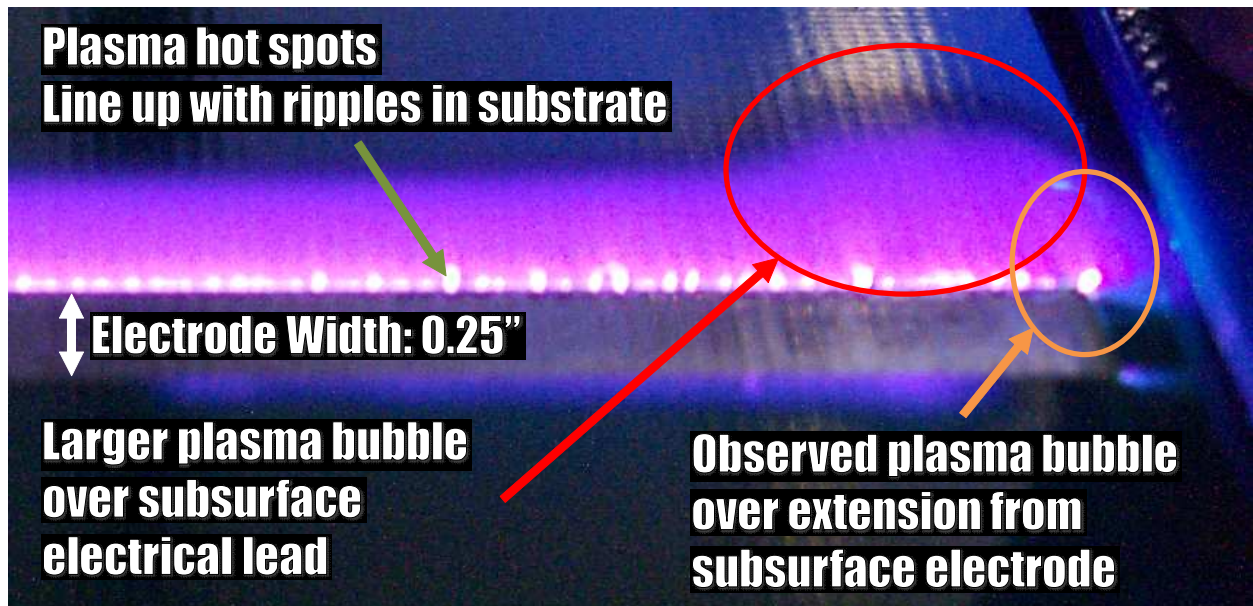
Figure 46: Long exposure photograph of actuator in operation. The plasma is very uniform, with some periodic "hot spots" along the actuator that coincide with ridges in the substrate that resulted from the manufacturing process.

Chapter 9

Conclusions and Opportunities

The objectives of this work were to:

- Develop a first-principles numerical model of a dielectric barrier discharge plasma actuator

- Experimentally validate the above model in channel flow

- Use results obtained from the validated model to explore and better understand the governing physics and emergent behaviors of dielectric barrier discharge plasma actuators

9.1   Fundamentals

An original plasma code based on first-principles was developed and tested. Experimental results substantiated numerical data obtained using a channel flow test case. *The plasma reaction chemistry model has been validated using known spectroscopic techniques, the transport model has been validated using the time-resolved shadowgraphy, and the extent and geometry of plasma formation has been validated using long exposure photography.* The model

demonstrates the capability of replicating emergent flow structures near a wall. *The model results support the hypothesis that actuators work by increasing vorticity near the wall by pressure changes brought on by heating and speciation.* These structures contribute to momentum transport that enhances the boundary layer's wall attachment and affect the flow in a manner that can be beneficial.

9.2   Actuator

This model permits studies to determine more effective shape, frequency, and magnitude of the applied voltage pulse. Additional studies regarding actuator architecture are also possible exploring dielectric thickness and electrode sizing. The sizing of the subsurface electrode is an important parameter with both the model and photographs showing the plasma bubble extending beyond the subsurface electrode in Figure 17 and Figure 34. *By adjusting the electrical and electrode parameters, the produced vorticity can be maximized to develop improved flow control.*

Further, the observation of the starting vortex in both the experimental and the numerical work indicates that the residual effects of the plasma's own induced electric field components shield and reduce the effects of the applied electric field. This is not unexpected given the presence of the charged particles, therefore this suggests that *the actuator improves pulse-to-pulse operation for comparatively short duty cycles at a given velocity.* This result supports observations in the literature that short duty cycle pulses are preferred [34, 38, 17]. This would be because a longer portion of the total cycle is given to allowing reaction products to convect out of the reaction zone near the actuator. However, to have improved effectiveness, higher pulse frequencies provide greater authority relative to any characteristic frequencies and time scales of the fluid [13]. *The present model allows the study and optimization of this trade-off for actuator design, effectiveness, and eventual use.*

In the case of an array of sequential actuators embedded in a surface, the model could be

employed to explore how best to arrange the actuators and time their relative activation to minimize the residual free charges left over by preceding pulses while maintaining higher apparent pulse rates. This investigation will require a three dimensional model. *Detailed analysis and comprehension of a variety of other excitation regimes, technologies, and conditions and their application will be made possible and can be studied directly from this work.*

The durability of dielectric barrier materials is a critical factor in the development of practical plasma actuators. The plasma discharges caused minor damage to the test article. A small amount of white powder on the board was caused by the plasma discharge. *Different materials should be investigated with the objective of understanding the durability of the dielectric barrier and understanding how material selection affects usability in each application.*

9.3 Experiment

Increased illumination and improved optics will significantly improve the precision of the shadowgraph measurements. Increased illumination can be achieved with the use of a laser built into the optics chain. The light coherence will permit a sharper image by minimizing the differential effect that any wavelength dependencies may have on the system. Upgrading the telescopes to a setup with parabolic mirrors would improve image quality by reducing the spherical aberration that occurs naturally near the edges of the image. Cameras with higher speed and higher resolution will enable shadowgraphs of higher flow speeds to be taken, allowing validation of the computational model at higher speeds at higher quality. Finally, image quality can be further improved by upgrading the shadowgraph system to a schlieren system. Both operate on the same principles of refracting flow structures, however schlieren systems are more sensitive to small changes in density. Thus it will provide more information about the flow.

Experimental efforts could be undertaken that would allow wider exploration of the model results. The model was run using dry air, but does have chemical mechanisms associated

with water built into it. The experiment was conducted in a laboratory with very low humidity and was treated as dry. *With control on the humidity level, experiments could be conducted that explore the performance variation of these actuators with respect to varying ambient humidity.*

9.4 Modelling

The computational model has many pieces; each could be enhanced. The fluid transport model should be upgraded to a second-order or higher model. This will mitigate the minor numerical diffusion and provide a more accurate fluid simulation. The addition of turbulence modelling will permit extension of this model into high speed regimes. The backwards Euler method is stable, but it occasionally exhibits convergence issues. A somewhat more sophisticated stiff solver would mitigate this issue. The use of an electrodynamics model would allow for a more accurate determination of the behavior and shape of the plasma volume.

A more flexible meshing system would allow computational efforts to be focused where more activity exists and thus permit greater accuracy for similar computational costs. Further, more flexible meshing would allow the application of the model to more complex geometries of further engineering interest. Overall, *more efficient algorithms would allow a longer simulation to be conducted, producing information on the quasi-steady operation of the device.*

Model runs can be used to explore different applied conditions. The model developed here can be used to study the effect of humidity on the actuator. The model was run using dry air, but has reaction mechanisms associated with water built into it. These explorations will help determine environmental effects on the flow control mechanisms. Additionally, inlet conditions (pressure, temperature, species, and velocity), can be investigated. *Studies of applied conditions would provide insight to actuator behavior in conditions that deviate further from ambient conditions than is readily achieved experimentally, and allow more*

comprehensive interrogation of expected flow structures and behaviors.

Bibliography

[1] P. H. Krupenie A. Lofthus. The spectrum of molecular nitrogen. *J. Phys. Chem. Ref. Data*, 6(1), 1977.

[2] T. C. Corke and M. L. Post. Overview of plasma flow control: Concepts, optimization, and applications. In 43rd *ASM*. AIAA, January 2005. Paper 2005-563.

[3] O. Eichwald, M. Yousfi, A. Hennad, and M. D. Benabdessadok. Coupling of chemical kinetics, gas dynamics, and charged particle kinetics models for the analysis of no reduction from flue gases. *J. Appl. Phys.*, 82(10):4781–4794, November 1997.

[4] J. Freidberg. *Plasma Physics and Fusion Energy*. Cambridge University Press, 2010.

[5] V. V. Golub, E. E. Son, A. S. Saveliev, V. A. Sechenov, and D. V. Tereshonok. Investigation of vortex structure near the surface of dbd-actuator. In 49th *ASM*. AIAA, January 2011. Paper 2011-154.

[6] United States Government. U.s. standard atmosphere, 1976. Technical Report NASA-TM-X-74335, National Oceanic and Atmospheric Adminstration, National Aeronautics and Space Administration, United States Air Force, 1976.

[7] H. R. Griem. *Plasma Spectroscopy*. McGraw Hill, United States, 1964.

[8] H. R. Griem. *Principles of Plasma Spectroscopy*. Cambridge University Press, Cambridge, 1997.

97

[9] E. P. Gyftopoulos and G. P. Beretta. *Thermodynamics: Foundations and Applications.* Dover Publications Inc., Mineola, NY, 2005.

[10] R. A. Freedman H. D. Young. *University Pysics.* Addison Wesley, United States, 11th edition, 2004.

[11] M. Hayashi. Recommended values of transport cross sections for elastic collision and total collisition cross section for electrons in atomic and molecular gasses. Technical Report IPPJ-AM-19, Institute of Plasma Physics, Nagoya University, Nagoya, Japan, 1981.

[12] W. C. Schneck III. Estimation of the real area of contact in sliding systems using thermal measurements. Master's thesis, Virginia Tech, 2009.

[13] W. C. Schneck III and W. F. O'Brien. Flow control over a circular cylinder using pulsed dbd actuators. *J. Turbo.*, 137, August 2014. Paper TURBO-14-1127.

[14] W. C. Schneck III and A. L. Winfrey. Model development for a dielectric barrier discharge plasma actuator for active flow control in immersed bodies. Presentation at PPPS 2013, 2013.

[15] S. Im, H. Do, and M. A. Cappelli. Plasma control of a turbulent boundary layer in an unstarting supersonic flow. In 49th *ASM*. AIAA, January 2011. Paper 2011-1143.

[16] J. D. Anderson Jr. *Computational Fluid Dynamics: The Basics with Applications.* McGraw-Hill, 1995.

[17] T. N. Jukes and K. Choi. Flow control around a circular cylinder using pulsed dielectric barrier discharge surface plasma. *Physics of Fluids*, (21), 2009. Paper 084103.

[18] A. J. Kotlar. The proper interpretation of the internal energy of formation used in thermodynamic equilibrium calculations. Technical Report BRL-MR-3985, U.S. Army Laboratory Command, Ballistic Research Laboratory, Aberdeen Proving Ground, MD, July 1992.

[19] D. Lam. Design of optical measurements for plasma actuators for the verification of quiescent and flow control simulations. Master's thesis, Virginia Polytechnic Institute and State University, Blacksburg, VA, 2015.

[20] J. B. Laten and R. P. LeBeau Jr. Examination of a plasma actuator model applied to dbd actuators for small aircraft applications. In 53rd *ASM*. AIAA, January 2015. Paper 2015-1732.

[21] L. Léger, E. Moreau, and G. G. Touchard. Effect of a dc corona electrical discharge on the airflow along a flate plate. *IEEE Transactions on Industry Applications*, 38(6):1478–1485, 2002.

[22] L. Léger, E. Moreau, and G. G. Touchard. Electrohydrodynamic airflow control along a flat plate by a dc surface corona discharge - velocity profile and wall pressure measurements. In 1st *Flow Control Conference*. AIAA, "June" 2002. Paper 2002-2833.

[23] A. V. Likhanskii. Particle-in-cell modeling of the pulsed dbd plasma actuator. In 40th *Fluid Dynamics Conference and Exhibit*. AIAA, July 2010. Paper 2010-5101.

[24] A. V. Likhanskii and V. V. Semak. The role of the photoionization in the numerical modeling of the dbd plasma actuator. In 47th *ASM*. AIAA, January 2009. Paper 2009-841.

[25] A. V. Likhanskii, M. N. Shneider, D. F. Opaits, R. B. Miles, and S. O. Macheret. Numerical modeling of dbd plasma actuators and the induced air flow. In 38th *Plasmadynamics and Lasers Conference*. AIAA, January 2007. Paper 2007-4533.

[26] W. K. Lord, D. G. MacMartin, and T. G. Tillman. Flow control opportunities in gas turbine engines. In *Fluids 2000*. AIAA, June 2000. Paper 2000-2234.

[27] G. V. Marr. *Plasma Spectroscopy*. Elsevier, Great Yarmouth, 1968.

[28] T. Matsuno, K. Ota, T. Kanatani, and H. Kawazoe. Parameter design optimization of plasma actuator configuration for separation control. In 5th *Flow Control Conference*. AIAA, "June" 2010. Paper 2010-4983.

[29] B. E. Mertz and T. C. Corke. Single-dielectric barrier discharge plasma actuator modelling and validation. *J. Fluid Mech.*, 669:557–583, 2011.

[30] H. Bahre P. Awakowicz V. Schulz-von der Gathen N. Bibinov, N. Knake. Spectroscopic characterization of an atmospheric pressure u jet plasma source. *J. Phys. D: Appl. Phys.*, 44(345204):12pp, August 2011.

[31] M. Nishihara, K. Takashima, J. W. Rich, and I. V. Adamovich. Mach 5 bow shock control by a nanosecond pulse surface dbd. In 49th *ASM*. AIAA, January 2011. Paper 2011-1144.

[32] National Institute of Standards and Technology. Nist chemistry webbook, 2015.

[33] D. E. Beasley R. S. Figliola. *Theory and Design for Mechanical Measurements*. John Wiley and Sons, 4th edition, 2006.

[34] C. Rethmel, J. Little, K. Takashima, A. Sinha, I. Adamovich, and M. Samimy. Flow separation control over an airfoil with nanosecond pulse driven dbd plasma actuators. In 49th *ASM*. AIAA, January 2011. Paper 2011-487.

[35] M. Richard, D. Dunn-Rankin, F. Weinberg, and F. Carleton. Maximizing ion-driven gas flows. *Journal of Electrostatics*, (64):368–376, 2006.

[36] S. Roy, K. P. Singh, and D. V. Gaitonde. Air plasma actuators for effective flow control. In 45th *ASM*. AIAA, January 2007. Paper 2007-184.

[37] D. Tafti. *Course Notes for ME/AOE 6434: Computational Fluid Dynamics*. Virginia Tech, Blacksburg, 2010.

[38] K. Takashima, Y. Zuzeek, W. R. Lempert, and I. V. Adamovich. Characterization of a surface dielectric barrier discharge plasma sustained by repetitive nanosecond pulses. In 41st *AIAA Plasmadynamics and Lasers Conference.* AIAA, June 2010. Paper 2010-4764.

[39] A. C. Thompson. Investigation and simulation of ion flow control over a flat plate and compressor cascade. Master's thesis, Virginia Tech, 2009.

[40] B. Vick. Multi-physics modeling using cellular automata. *Complex Systems*, 17:65–78, 2007.

[41] C. C. Wang and S. Roy. Geometry effects of dielectric barrier discharge on a flat surface. In 49th *ASM.* AIAA, January 2011. Paper 2011-732.

[42] S. Yamada, K. Shibata, H. Ishikawa, S. Honami, and M. Motoske. Flow behavior behind a circular cylinder by dbd plasma actuators in low reynolds number. In 48th *ASM.* AIAA, January 2010. Paper 2010-549.

Appendix A

Simulation Initial Conditions

This appendix presents the initial conditions for the presented numerical model: Figure 47 shows the x-momentum, Figure 48 shows the y-momentum, Figure 49 shows the centerline static pressure, and Figure 50 shows the centerline total number density. The static pressure and total number density show no significant variation in the wall normal direction, thus the centerline traces are shown. The initial temperature is uniform at $300K$.
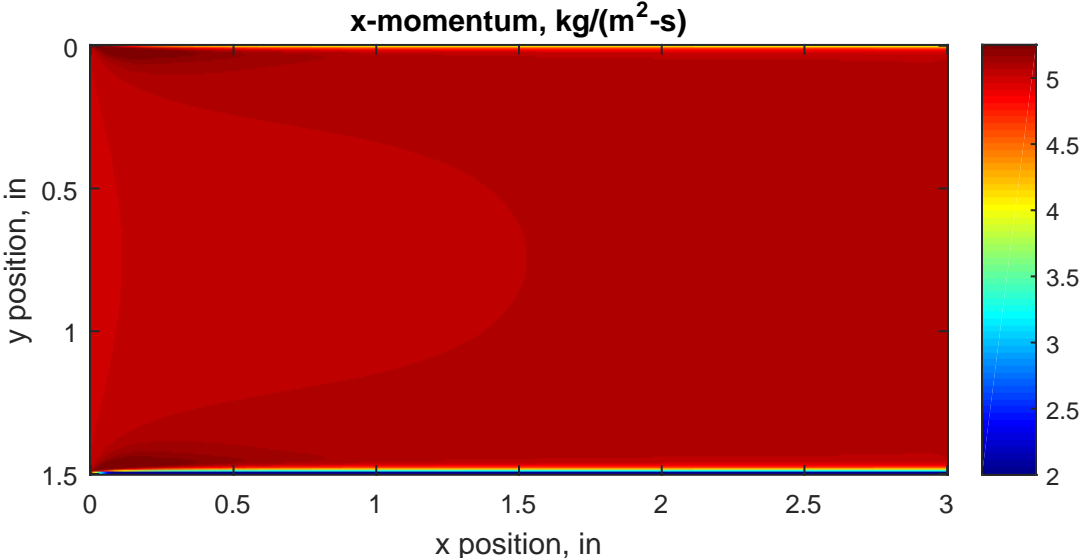
Figure 47: Initial condition for the x-momentum
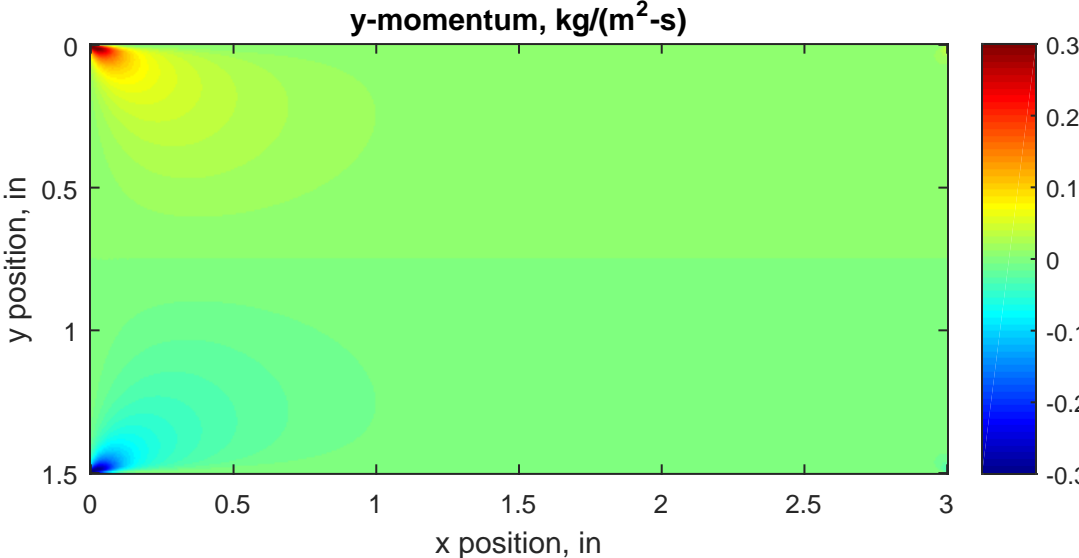
Figure 48: Initial condition for the y-momentum
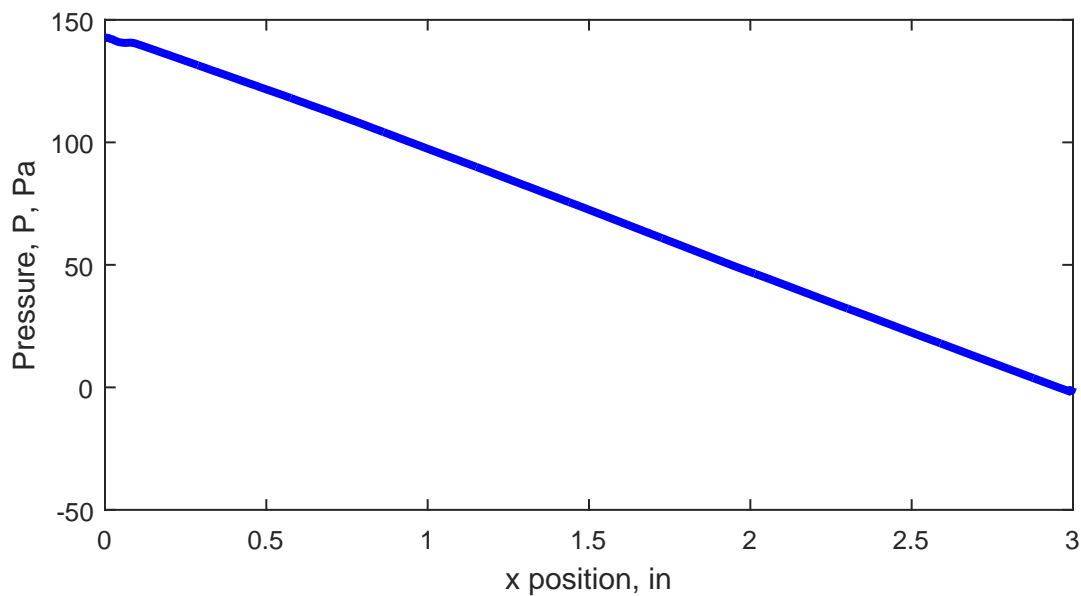
Figure 49: Initial condition for the static pressure
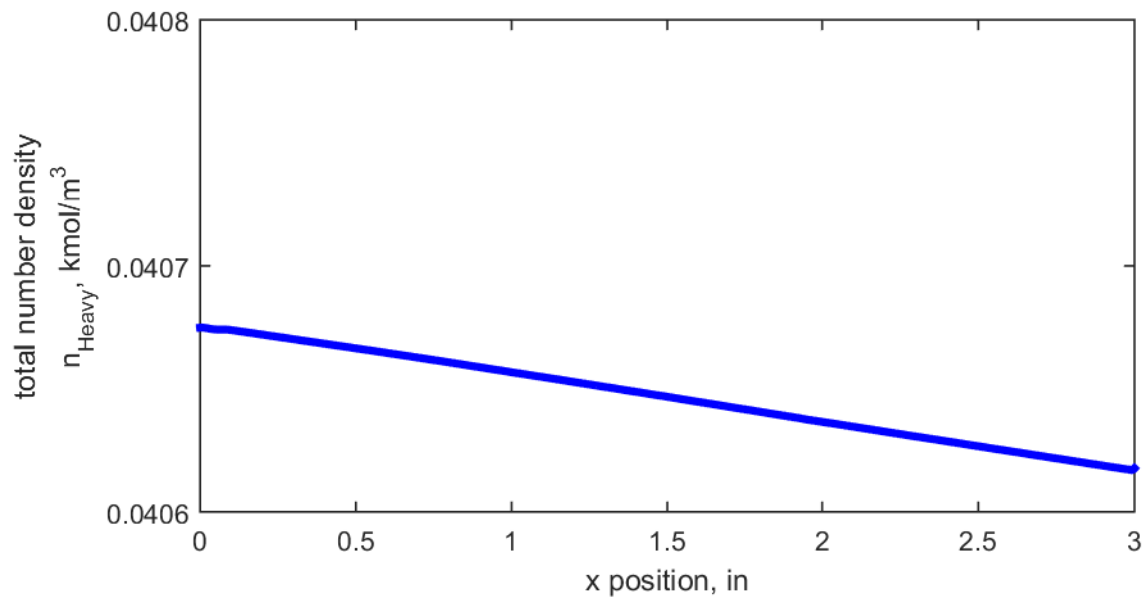
Figure 50: Initial condition for the total number density

Appendix B

Reference [13]: Dielectric Barrier Discharge Flow Effects Experiments at Virginia Tech

This work published in the ASME Journal of Turbomachinery [13] laid the foundations for the development of the model and the selection of the desired validation data.

Flow Control Over a Circular Cylinder Using Pulsed Dielectric Barrier Discharge Actuators

William C. Schneck, III[1]

Turbomachinery and Propulsion Laboratory,
Department of Mechanical Engineering,
Virginia Tech,
Blacksburg, VA 24061
e-mail: wschneck3@gmail.com

Walter F. O'Brien

J. Bernard Jones Professor of Mechanical
Engineering,
Turbomachinery and Propulsion Laboratory,
Department of Mechanical Engineering,
Virginia Tech,
Blacksburg, VA 24061
e-mail: walto@vt.edu

Immersed bodies such as struts, vanes, and instrumentation probes in gas turbine flow systems will, except at the lowest of flow velocities, shed separated wakes. These wakes can have both upstream and downstream effects on the surrounding flow. In most applications, surrounding components are designed to be in the presence of a quasi-steady or at least nonvariant flow field. The presence of unsteady wakes has both aerodynamic and structural consequences. Active flow control of wake generation can therefore be very valuable. One means to implement active flow control is by the use of plasma actuation. Plasma actuation is the use of strong electric fields to generate ionized gas that can be actuated and controlled using the electric fields. The controlling device can be based on AC, DC, or pulsed-DC actuation. The present research was conducted using pulsed-DC from a capacitive discharge power supply. The study demonstrates the applicability of, specifically, pulsed-DC plasma flow control of the flow on a circular cylinder at high Reynolds numbers. The circular cylinder was selected because its flow characteristics are related to gas turbine flowpath phenomena, and are well characterized. Further, the associated pressure gradients are some of the most severe encountered in fluid applications. The development of effective plasma actuators at high Reynolds numbers under the influence of severe pressure gradients is a necessary step toward developing useful actuators for gas turbine applications beyond laboratory use. The reported experiments were run at Reynolds numbers varying from 50,000 to 97,000, and utilizing various pulse frequencies. Further the observed performance differences with varying electric field strengths are discussed for these Reynolds numbers. The results show that flow behaviors at high Reynolds numbers can be influenced by these types of actuators. The actuators were able to demonstrate a reduction in both wake width and momentum deficit.
[DOI: 10.1115/1.4028236]

Introduction

Flow Control. Within a gas turbine, a wide variety of speeds, temperatures, and flow conditions exist. These can all potentially benefit from some form of applied flow control. Example applications can include: low pressure turbines with low Re flows, combustor flame control, blade tip leakage, inlets, interturbine ducts, nacelles, nozzles, and vanes. Indeed, anywhere boundary layer losses exist, flow control can potentially be leveraged to reduce the losses [1].

Plasma flow control methods are one means of achieving active flow control. One type of actuator utilizes a pulsed high voltage DC dielectric barrier discharge (DBD) actuator to create the plasma for control. The motivation for the present research is to understand the capabilities of this technology with regard to the control of separating flow over a cylinder in crossflow. The current work demonstrates effective separation and wake control of a cylinder in crossflow over an increased range of Reynolds numbers relative to previous work. Additionally, it seeks to develop understanding of the effect of pulse frequency on this actuator type. Thus, the selected range for this research was from Re $= 50,000 \rightarrow 97,000$ and $f^+ = 0.32 \rightarrow 1.0$. This includes velocities up to $U_\infty = 25$ m/s.

Ion Flow Control Principles. Fundamentally, plasma control methods create locally ionized gas that can be manipulated electromagnetically to induce changes in flow conditions. Among advantages of plasma flow control methods is that they contain no moving parts. This makes mechanical failure highly unlikely. Additionally, unlike methods such as vortex generators, these actuators are flush with the flow surface, and thus lack the significant increase in skin friction losses associated with flow protrusions. Further, they are active systems and can be turned off when not needed to save power. Finally, the actuators themselves are lightweight. Any significant weight growth comes from power supply requirements.

Topics to be addressed by plasma flow control research include that, as an active system, it must consume power. Thus, the value of the improvement in flow character must outweigh the power consumed. Additionally, as an active system, there are multiple failure modes, and thus more opportunities for failure, such as dielectric breakdown, power supply failure, or electrode corrosion and erosion. Further, there may be significant electromagnetic (EMI) issues if the actuators are used extensively in an unshielded system. This could interfere with other electrical systems associated with the engine. Finally, the power supply brings with it weight growth, if no high capacity high voltage line exists in the system already. This is more an issue for aero turbines, but could be important for ground based turbines as well.

Review of Related Previous Work. Plasma flow control techniques have been actively studied in many flow regimes and situations. These include potential applications in struts, airfoils [2], inlets [3], and various low Reynolds number flows [4].

Immersed bodies create wakes. The velocity deficit associated with wakes is a source of drag. For circular cylinders, subcritical flow exists below Re $= 130,000$. This entails laminar separation,

which occurs at approximately 80 deg from the leading edge. Circular cylinders in subcritical flow regimes preferentially shed vortices at a reduced frequency of approximately $f^+ = 0.21$ [5].

One type of plasma actuator utilizes surface mounted electrodes to achieve an "ion wind" type actuation. Studies of such actuators have been undertaken by several authors [6–9]. These actuators utilize a high voltage DC corona. These have claims of a larger effective region; however, they have demonstrated sensitivity to ambient conditions and to the quality of manufacture. The actuators produce changes in the boundary layer through a body force acting on the momentum of the flow. Research efforts have focused mostly on flat plate architectures.

Another type of plasma actuator utilizes a DBD actuator excited with a high frequency and high voltage AC power source. These utilize voltages frequently on the order of 10 s of kV and frequencies on the order of up to 10 s of kHz. Most of these are modeled through body force terms in the momentum equation as well. They have been studied on many geometries, but have typically utilized rather low speeds ($U_\infty < 12\text{m/s}$) on cylinders [10], and higher speeds ($U_\infty = 30\,\text{m/s}$) on airfoils [11].

A similar type of actuator to the AC-DBD is a DBD actuator that uses a pulsed high voltage DC power supply. These use pulse widths on the order of 10 s to 100 s of ns [12], utilizing pulse frequencies from 100 Hz–10 kHz [13]. It has been proposed that the physical mechanism, instead of coupling through the momentum of the flow, couples through a propagating density wave due to local rapid heating near the actuator [12]. Results on the wake have been demonstrated on cylinders at Re = 15,000, with a speed $U_\infty = 4.6\,\text{m/s}$ [13]. Further, pulse frequencies near the shedding frequency have shown to induce shedding lock on to the pulse frequency and increase drag [13]. Additionally, bow shock control has been demonstrated with remarkable success [14]. Reattachment using this method has further been demonstrated on airfoils with $U_\infty = 93\,\text{m/s}$ [2]. Further, quiescent studies regarding the induced flow by both AC-DBD and pulsed-DBD actuators have been undertaken [12,15]

Experiment Arrangement

Tunnel. The present experiments were conducted using a low speed wind tunnel, driven by a large centrifugal fan with variable inlet vanes. These inlet vanes allowed for changes in the flow velocity approaching the cylinder. The construction of the tunnel includes a large diverging–converging flow conditioning section immediately downstream of the fan [16]. The maximum area portion of the tunnel is a 4 ft × 4 ft (1.22 m × 1.22 m) plenum with a static pressure tap. From this, it converges down to the test section which is a 1 ft × 1 ft × 2 ft (30.5 cm × 30.5 cm × 61.0 cm) section with mounting hardware for the cylinder located 1 ft (30.5 cm) upstream of the outlet. Mounted to the test section is a 21 cm traverse to which instrumentation can be mounted to plunge through the wake. A photograph of this apparatus can be seen in Fig. 1, and a schematic seen in Fig. 2.

Test Article. The cylinder used for these experiments was 6 cm in diameter. DBD actuators were placed at ± 80 deg and ± 150 deg from the leading edge. The forward locations were selected as the anticipated separation locations for laminar flow on a cylinder [5]. The aft locations were selected to study the effect of actuation in the separated region of the cylinder. The effect of the aft actuators will be detailed in a future paper discussing turbulence intensity in the wake region. The actuators were installed over the middle 6 in. (15.2 cm) of the span of the cylinder. Photos of the cylinder can be seen in Fig. 3.

The actuators themselves were hand-manufactured using 1/4 in. (6.35 mm) wide, 0.0035 in. (0.0889 mm) thick adhesive backed copper strip, and 0.005 in. (0.127 mm) thick Kapton® sheet. They were manufactured with the submerged electrode downstream and adjacent to the surface electrode, as seen in Fig. 4. The actuators
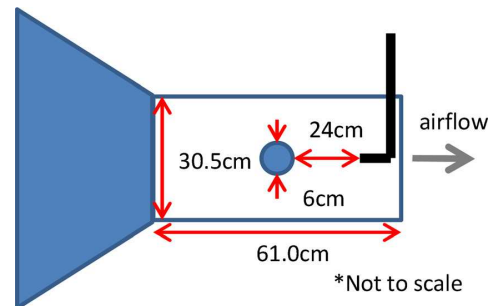

Fig. 1   Data collection apparatus

Fig. 2   Tunnel schematic

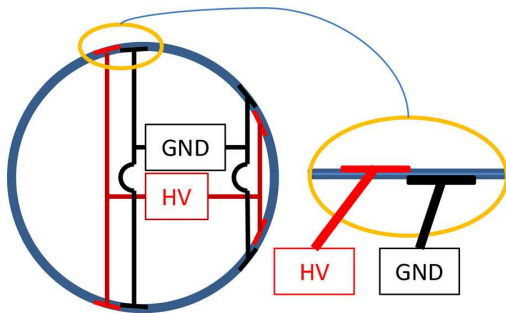Fig. 3   Close up photos of the cylinder actuators

107

Fig. 4 Electrical and positioning schematic of the cylinder electrodes. The red electrodes are at high voltage, and the black ones are grounded.

were wired with the surface electrodes at the ± 80 deg actuators connected to the positive output of the high voltage source, and with the surface electrodes at the ± 150 deg grounded. The electrical connections can be seen in Fig. 4 as well.

Article/Test Section Discussion. The area blockage of the wind tunnel test section by the cylinder is relatively large, with approximately 20% of the flow blocked. This large cylinder size was selected in order to fit four actuators and to increase the Reynolds number of the cylinder. This results in some interaction between the walls and the cylinder, and this is observed in the data. Because only the flow speed and pulse frequency were changed, comparisons between different data sets are still valid, but are not directly equivalent to a cylinder in a true open-flow system. As a means of comparison of the data, the Reynolds numbers are computed using the upstream tunnel velocity as computed by Eq. (1),

$$U_\infty = \sqrt{\frac{2P_\text{plenum}}{\rho\left(\left(C_\text{D}\dfrac{d \times L}{A_\text{exit}}\right) + 1 - \left(\dfrac{A_\text{exit}}{A_\text{plenum}}\right)^2\right)}} \qquad (1)$$

High Voltage (HV) Pulse Generation Hardware. The high voltage pulses were generated using a commercial-off-the-shelf capacitive discharge ignition system for automotive applications. This capacitive discharge ignition (CDI) unit was then connected to a high performance automotive ignition coil, which was connected to the cylinder test article. The CDI module was gated using a B&K 4030 pulse generator. The pulse generator had a variable pulse rate that was tuned to achieve the pulse frequencies used in the data collection and analysis. The electrical system is shown in Fig. 5.

Instrumentation. A pitot-static probe was attached to the traverse on the test section to collect the data for this experiment. The pitot-static probe was traversed across the wake at a distance four diameters downstream of the trailing edge of the cylinder. Attached to the pitot-static probe was a proportional current output model 616-3 Dwyer transducer that measured the dynamic pressure. The current output was routed through a resistor of measured impedance of $R = 464\Omega$. The voltage drop across the resistor was measured by an NI-6259 16-bit USB multifunction data acquisition card. The data were acquired at 100 samples/s for 5 s for time averaging. The plenum static pressure was also measured to calculate the flowrate through the tunnel, using a 10in-H2O 422-10 Dwyer inclined manometer. A schematic of the instrumentation setup is shown in Fig. 6.

Test Matrix. As this experiment sought to determine the behavior of the wake at different speeds under the influence of the
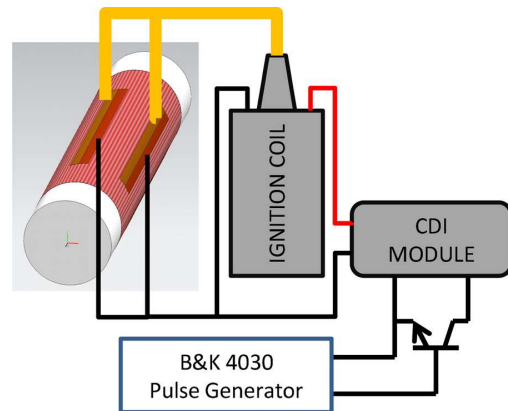
Fig. 5 Power supply schematic
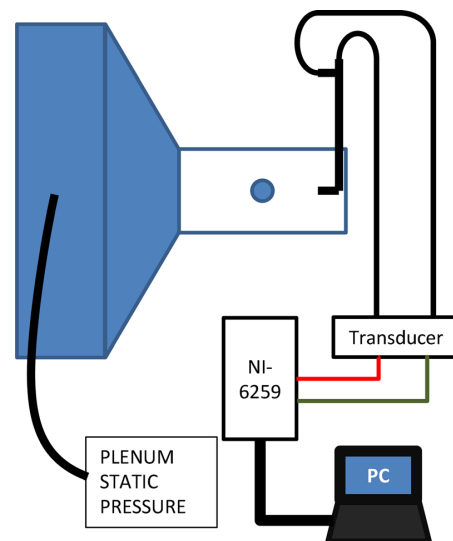
Fig. 6 Schematic of the instrumentation setup

pulsed-DC action, a set of Reynolds numbers and pulse frequencies was selected. The frequencies were nondimensionalized as $f^+ = fd/U_\infty$, where f is the gate frequency of the B&K 4030 pulse generator, and thus the pulse frequency of the CDI module. Those selections can be seen in Table 1. As mentioned above, since pulse frequencies near the shedding frequency have been shown to increase the drag [13], high frequencies were desired for this series of tests. The maximum f^+ attainable by the power supply was 1.0. We used this reduced frequency, and two other lower ones for comparison, to show the effect of varying f^+. Since there was only one model of cylinder manufactured for this experiment, the Reynolds number was varied by changing the velocity and the reduced frequency was selected by changing the frequency of the pulse generator. The selected velocities and frequencies are also presented in the table.

Uncertainty/Sensitivity Analysis. In order to determine the accuracy of the data, an uncertainty and sensitivity analysis was performed. The uncertainty for the dynamic pressure measurements was computed using Eq. (2), and the uncertainty for the plenum static pressure was computed using Eq. (3). These calculated

Table 1 Experiment test matrix

Re = 50,000 $f^+ = 0.32$ $U_\infty = 12.9\,\text{m/s}$ $f = 69\,\text{Hz}$	Re = 68,000 $f^+ = 0.32$ $U_\infty = 17.6\,\text{m/s}$ $f = 94\,\text{Hz}$	Re = 97,000 $f^+ = 0.32$ $U_\infty = 25.2\,\text{m/s}$ $f = 138\,\text{Hz}$
Re = 50,000 $f^+ = 0.57$ $U_\infty = 12.9\,\text{m/s}$ $f = 122\,\text{Hz}$	Re = 68,000 $f^+ = 0.57$ $U_\infty = 17.6\,\text{m/s}$ $f = 166\,\text{Hz}$	Re = 97,000 $f^+ = 0.57$ $U_\infty = 25.2\,\text{m/s}$ $f = 243\,\text{Hz}$
Re = 50,000 $f^+ = 1.0$ $U_\infty = 12.9\,\text{m/s}$ $f = 217\,\text{Hz}$	Re = 68,000 $f^+ = 1.0$ $U_\infty = 17.6\,\text{m/s}$ $f = 296\,\text{Hz}$	Re = 97,000 $f^+ = 1.0$ $U_\infty = 25.2\,\text{m/s}$ $f = 434\,\text{Hz}$

results were used in a sensitivity analysis of the velocity profiles. The sensitivities of the velocity profiles were computed using a root of the sum of the squares method with the coefficients from the Taylor expansion shown in Eq. (4). The magnitudes of these sensitivities are shown later in Fig. 7.

$$\Delta P_{\text{probe}} = \sqrt{\left((\Delta P_{\text{xducer}})^2 + (\Delta P_{\text{card}})^2\right)} = \pm 6.22\,\text{Pa} \qquad (2)$$

$$\Delta P_{\text{plenum}} = \Delta P_{\text{manometer}} = \pm 1.24\,\text{Pa} \qquad (3)$$

$$\Delta \frac{u}{U_\infty} = \sqrt{\left(\frac{\partial(u/U_\infty)}{\partial P_{\text{probe}}}\Delta P_{\text{probe}}\right)^2 + \left(\frac{\partial(u/U_\infty)}{\partial P_{\text{plenum}}}\Delta P_{\text{plenum}}\right)^2} \qquad (4)$$

Experiment Results and Discussion

Calculation of Velocity From Pitot-Static Probe Data. The data were collected across the wake in 0.5 cm steps. Each time the probe was moved, the dynamic pressure was measured first with the actuators turned off, and then with the actuators turned on. At

the beginning of each sweep, the speed of the tunnel was set by use of the inclined manometer, with the plenum static pressure recorded. Local barometric pressure and temperature were measured and recorded. Once the conditions were known, the pulse frequency was set on the pulse generator, and then the sweep commenced.

The measured velocity profiles are presented below in Fig. 7. The data have been shifted to have the y-axis centered on the minimum value of the unaltered wake. The data are presented with the x-axis being the velocity profile normalized against the bulk flow velocity, with these velocities computed as shown in Eq. (5) and the y-axis being the position of the probe normalized against the cylinder diameter

$$u = \sqrt{\frac{2P_{\text{probe}}}{\rho}} \qquad (5)$$

The velocity profiles of the cylinder with the actuators turned off are shown with the blue line. The velocity profiles of the cylinder with the actuators turned on are shown by the red line. These profiles demonstrate reductions in wake depth and width by the actuator for all cases. The error bars indicate the estimated uncertainty in the results. Particularly at higher speeds, the relative size of the error is decreased significantly. Additionally, one can see in these results that the cylinder wakes exhibit some offset. This observed pitch deviation of the wake from the horizontal plane was likely caused by a combination of inaccurate positioning of the electrodes on the cylinder surface, and error in aligning the neutral axis of the cylinder in the wind tunnel.

Calculation of Half-Wake Parameters and Their Improvements

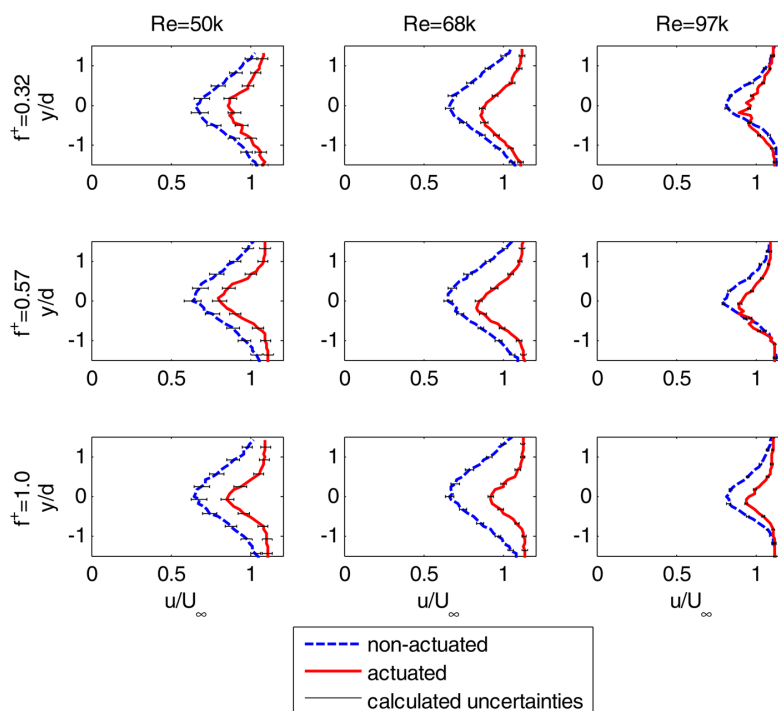*Depth.* A simple, nondimensional metric for the depth of the wake is desired. For this data, the depth was computed as

Fig. 7 Measured velocity profiles at different Reynolds numbers and reduced frequencies

Table 2 Computed wake depths

Wake depth	Re = 50,000		Re = 68,000		Re = 97,000	
	Uncontrolled	Controlled	Uncontrolled	Controlled	Uncontrolled	Controlled
$f^+ = 0.32$	0.400	0.231	0.407	0.244	0.285	0.202
$f^+ = 0.57$	0.412	0.284	0.419	0.269	0.306	0.205
$f^+ = 1.0$	0.401	0.231	0.405	0.196	0.277	0.163

Table 3 Percent reduction in wake depth with flow control

Wake depth reduction	Re = 50,000	Re = 68,000	Re = 97,000
$f^+ = 0.32$	42.3%	40.2%	29.1%
$f^+ = 0.57$	31.0%	35.8%	32.9%
$f^+ = 1.0$	42.5%	51.7%	40.9%

Table 5 Percent reduction in wake width with flow control

Wake width reduction	Re = 50,000	Re = 68,000	Re = 97,000
$f^+ = 0.32$	21.3%	37.2%	−11.2%
$f^+ = 0.57$	47.9%	48.4%	10.9%
$f^+ = 1.0$	61.8%	64.8%	39.3%

$$\text{depth} = \frac{\max(u) - \min(u)}{U_\infty} \qquad (6)$$

This is a nondimensional representation of the largest deficit in velocity that the wake exhibits. If the wake depth were zero, the implication would be that the wake had been entirely removed. Thus, smaller values are desirable. This calculation was run for all cases and is presented in Table 2.

The reduction in wake depths is shown in Table 3. The reductions are all very large, being on the order of almost 30% or greater, however, varying relationships with reduced frequency or Reynolds number is evident in this data, having scattered ups and downs. More data will be required to determine the firm relationships with this characteristic. Although trends cannot be confirmed, in all cases, the depth was significantly reduced.

Width. A simple, nondimensional metric for the width of the wake is also desired. For the collected data, it was computed using

$$\text{width} = \frac{2w}{d} \qquad (7)$$

The wake width was computed between the centerline of the wake and one end due to the limitations of the length of the probe. This required the assumption of a symmetric wake to compute the full wake width. The effect of this assumption is discussed later. As with the wake depth, small values are desirable. The wake widths were generally reduced except in one case. Only the Re = 97,000, $f^+ = 0.32$ case exhibited an increase in wake width, for unknown causes. These widths are presented in Table 4.

The reduction in wake widths is shown in Table 5. These reductions show a strong dependence on reduced frequency, with decreasing width for increased frequency. Again, the wake can be seen to increase in its width in the Re = 97,000, $f^+ = 0.32$ case. There is insufficient evidence in this data to suggest any correlated dependence on the Reynolds number for the wake width reduction. However, wake width reduction for all Re = 97,000 cases

was lower than the other two Reynolds numbers for similar reduced frequency.

Wake "Intensity". A mathematical tool for comparing wakes involving both extent and depth is desired here. Due to its broad usage, and the qualitatively similar profile shapes, the procedure of the SAE Aerospace Recommended Practice ARP1420 was selected. This will give a mathematically familiar sense of the velocity deficit developed by the wake. The expressions that generate the intensity values are shown as follows:

$$u_{\text{ave}} = \frac{1}{y_n - \text{CL}} \int_{\text{CL}}^{y_n} u \, dy$$

$$u_{\text{ave}_{\text{low}}} = \frac{1}{\delta - \text{CL}} \int_{\text{CL}}^{\delta} u \, dy \qquad (8)$$

$$\text{intensity} = \frac{u_{\text{ave}} - u_{\text{ave}_{\text{low}}}}{u_{\text{ave}}}$$

Again, these equations were cast in a form assuming symmetry across the wake. The intensities are presented in Table 6. One can see that the distortion intensity is reduced by the flow control in all cases.

The reductions in wake intensity are shown in Table 7. In general, the wake intensity reductions are large, with the Re = 50,000, $f^+ = 0.57$ case seeming largely out of line with the other data. There seems to be no strong relationship between the intensity reduction and the Reynolds number or the reduced frequency.

Momentum. Next, a nondimensional metric for the increase in the momentum of the flow behind the cylinder was computed using

$$\text{momentum increase} = \frac{\int_{\text{CL}}^{y_n} \left(u_{\text{on}}^2 - u_{\text{off}}^2 \right) dy}{\int_{\text{CL}}^{y_n} u_{\text{off}}^2 \, dy} \qquad (9)$$

Larger values of momentum increase indicate greater flow control. The calculated values are presented in Table 8. For the lower

Table 4 Computed wake widths

Wake width	Re = 50,000		Re = 68,000		Re = 97,000	
	Uncontrolled	Controlled	Uncontrolled	Controlled	Uncontrolled	Controlled
$f^+ = 0.32$	3.23	2.54	2.87	1.80	1.31	1.46
$f^+ = 0.57$	3.01	1.57	2.66	1.37	1.52	1.35
$f^+ = 1.0$	3.14	1.20	2.72	0.956	1.59	0.966

Table 6   Computed wake intensities

Wake intensity	Re = 50,000		Re = 68,000		Re = 97,000	
	Uncontrolled	Controlled	Uncontrolled	Controlled	Uncontrolled	Controlled
$f^+ = 0.32$	0.167	0.0889	0.167	0.0955	0.125	0.0677
$f^+ = 0.57$	0.152	0.134	0.173	0.122	0.133	0.0897
$f^+ = 1.0$	0.168	0.0993	0.165	0.0927	0.122	0.0750

Table 7   Percent reduction in wake intensity with flow control

Intensity reduction	Re = 50,000	Re = 68,000	Re = 97,000
$f^+ = 0.32$	46.9%	42.9%	45.8%
$f^+ = 0.57$	12.2%	29.8%	32.7%
$f^+ = 1.0$	41.0%	43.7%	38.7%

Table 8   Percent increase in wake momentum with flow control

Momentum increase	Re = 50,000	Re = 68,000	Re = 97,000
$f^+ = 0.32$	19.5%	24.3%	2.46%
$f^+ = 0.57$	19.4%	24.9%	4.69%
$f^+ = 1.0$	28.6%	32.1%	9.87%

Table 9   Percent reduction in wake momentum deficits with flow control

Momentum deficit reduction	Re = 50,000	Re = 68,000	Re = 97,000
$f^+ = 0.32$	45.2%	59.7%	18.2%
$f^+ = 0.57$	50.1%	65.5%	28.3%
$f^+ = 1.0$	67.2%	84.4%	57.2%

Table 10   Percent increase in wake KE with flow control

KE increase	Re = 50,000	Re = 68,000	Re = 97,000
$f^+ = 0.32$	27.3%	34.6%	2.81%
$f^+ = 0.57$	28.4%	35.9%	6.20%
$f^+ = 1.0$	42.0%	47.4%	13.8%

Table 11   Percent reduction in KE deficit with flow control

KE deficit reduction	Re = 50,000	Re = 68,000	Re = 97,000
$f^+ = 0.32$	42.0%	57.5%	14.7%
$f^+ = 0.57$	48.6%	64.2%	26.1%
$f^+ = 1.0$	65.2%	83.8%	55.4%

two Reynolds numbers, performance was very good, ranging from approximately 20%–30% improvement in the wake momentum. There was a significant reduction in performance comparatively for all of the Re = 97,000 cases. There does seem to be some dependence on f^+ in the data, with the momentum improvement increasing as the reduced frequency is increased.

Alternatively, the data were used to calculate the reduction in the momentum deficit. It shows the same trends, but a value of 100% would be where the cylinder ceases to be a drag body and becomes a thrust body. The method used to compute these values is shown as

$$\text{momentum deficit reduction} = \frac{\int_{\text{CL}}^{y_n} \left(u_{\text{on}}^2 - u_{\text{off}}^2 \right) dy}{\int_{\text{CL}}^{y_n} \left(U_{\text{open}}^2 - u_{\text{off}}^2 \right) dy} \qquad (10)$$

The results are tabulated in Table 9. This presentation of the data shows more strongly a relationship between reduced frequency and amount of flow control achieved. Additionally, while the performance at Re = 97,000 is still depressed, the high reduced frequency case shows significant flow control relative to the deficit. Further, the Reynolds number data are suggestive of some peaking behavior; however, again, there is an insufficient number of Reynolds numbers investigated to suggest an actual relationship.

Kinetic Energy (KE). Finally, a similar metric to that used for momentum was also computed for the KE increase of the wake. This was computed by

$$\text{KE increase} = \frac{\int_{\text{CL}}^{y_n} \left(u_{\text{on}}^3 - u_{\text{off}}^3 \right) dy}{\int_{\text{CL}}^{y_n} u_{\text{off}}^3 \, dy} \qquad (11)$$

Large values are desirable here as well. The results are presented in Table 10. Considering the form of the equation, the trends the results exhibit will be similar to the momentum metrics. That said, the relationship of the flow control performance with the reduced frequency is even more pronounced in the energy

metrics. The higher frequency data show even greater energy increase fractionally than the momentum increases exhibited.

As with the momentum metrics, the KE increase can be represented as a change relative to the KE deficit. This is computed by Eq. (12) in a similar fashion

$$\text{KE deficit reduction} = \frac{\int_{\text{CL}}^{y_n} \left(u_{\text{on}}^3 - u_{\text{off}}^3 \right) dy}{\int_{\text{CL}}^{y_n} \left(U_{\text{open}}^3 - u_{\text{off}}^3 \right) dy} \qquad (12)$$

These metrics are computed and tabulated in Table 11. These data show remarkable reductions in the KE deficit of the flow. This would equate to the reduction in the energy required to move this cylinder through the air. Again, the trends are similar to those of the momentum.

Comparison With Full-Wake Data for Re = 97,000. The half-wake data here are compared with the full wake data for Re = 97,000. The data collected at Re = 97,000 had a narrow enough physical wake that it was possible to obtain full wake data with the available flow probe. Thus, in this case, it could be compared to the half-wake computed data. This comparison is presented in Table 12. For some metrics, there was very good agreement. Wake intensity had the closest agreement between the half-wake and full-wake data. This would indicate that it is actually a very robust method of determining some of the wake character. For the other parameters, the momentum and KE methods showed good agreement at the higher pulse frequencies. There was weaker agreement for the low pulse frequency and for the

Table 12 Comparison between full-wake calculations and half-wake calculations

frequency	Width		Intensity		Momentum deficit		KE deficit	
	Half	Full	Half	Full	Half	Full	Half	Full
$f^+ = 0.32$	−11.2%	−3.19%	45.8%	42.0%	18.2%	24.7%	14.7%	21.6%
$f^+ = 0.57$	10.9%	15.5%	32.7%	31.7%	28.3%	27.0%	26.1%	24.9%
$f^+ = 1.0$	39.3%	47.5%	38.7%	38.8%	57.2%	58.1%	55.4%	56.4%

wake width. However, they still exhibited similar behaviors. This supports the use of the half-wake data in the above analyses.

Conclusions and Recommendations

The overall performance of the actuators on this cylinder clearly demonstrated strong wake control effects. These experiments were conducted at flow speeds that are generally higher than reported in the literature, and approach possible gas turbine applications. Achieving this kind of flow control at higher flow speeds has potential applications for the reduction of the flow losses for components such as struts, vanes, and instrument protuberances. The data presented here are as yet insufficient to determine the exact relationship between flow control and Reynolds number, and there is an observed reduction in performance at $Re = 97,000$. The data does show a distinct improvement in flow control with increased frequency. This improved performance with increased pulse frequency is consistent with findings in the literature [13]. Additional models and experiments have shown significant wake reduction in both wake width and depth, particularly for low speed flows [4,10,13,17,18].

Further experiments should be conducted at additional and higher Reynolds numbers to gain a better understanding of the relationship between Reynolds number and amount of flow control. Additionally, data should be collected at higher nondimensional frequencies to determine where increased frequency may no longer be beneficial. Further data of interest would be the relationship of turbulence intensity to these parameters. Thus, a time accurate measurement of the wake should be undertaken.

Additionally, more complex architectures should be explored to determine other means of enhancing the flow. This could include serpentine actuators [19,20] and "sliding discharge" actuators [21].

As a means of determining the efficiency of the actuation technique, the coil output voltage (with a HV probe) and the coil output current (with a Hall effect sensor) should be measured. This would provide knowledge of the instantaneous voltage and current drawn by the actuator and would enable the calculation of the instantaneous power draw and the mean power draw. These results can then be compared to the absolute change in KE of the wake to determine an overall system performance factor.

Acknowledgment

Nomenclature

A_{exit} = cross sectional area of the exit of the tunnel
A_{plenum} = cross sectional area of the plenum
C_D = coefficient of drag of the cylinder in crossflow
CL = centerline of the wake where u/U_∞ is minimum
d = cylinder diameter
f = frequency
f^+ = reduced (nondimensional) frequency
L = span of the cylinder
P_{plenum} = static pressure in the plenum of the wind tunnel
P_{probe} = dynamic pressure of the pitot-static probe
Re = Reynolds number (always computed based on the cylinder diameter)
u = local velocity
U_{open} = unblocked tunnel flow velocity for the same plenum static pressure ($C_D = 0$).
U_∞ = flow velocity approaching the cylinder
w = distance from the centerline to where $u/U_{open} = 0.95$
y_n = Point sufficiently outside the uncontrolled wake to function as a numerical integration limit
δ = position where $u = u_{ave}$
ρ = density of air

References

[1] Lord, W. K., MacMartin, D. G., and Tillman, T. G., 2000, "Flow Control Opportunities in Gas Turbine Engines," AIAA Paper No. 2000-2234.
[2] Rethmel, C., Little, J., Takashima, K., Sinha, A., Adamovich, I., and Samimy, M., 2011, "Flow Separation Control Over an Airfoil With Nanosecond Pulse Driven DBD Plasma Actuators," AIAA Paper No. 2011-487.
[3] Im, S., Do, H., and Cappelli, M. A., 2011, "Plasma Control of a Turbulent Boundary Layer in an Unstarting Supersonic Flow," AIAA Paper No. 2011-1143.
[4] Yamada, S., Shibata, K., Ishikawa, H., Honami, S., and Motoske, M., 2010, "Flow Behavior Behind a Circular Cylinder by DBD Plasma Actuators in Low Reynolds Number," AIAA Paper No. 2010-549.
[5] Schlichting, H., and Gersten, K., 2003, Boundary Layer Theory, 8th ed., Springer-Verlag, Berlin.
[6] Thompson, A. C., 2009, "Investigation and Simulation of Ion Flow Control Over a Flat Plate and Compressor Cascade," Master's thesis, Virginia Tech, Blacksburg, VA.
[7] Richard, M., Dunn-Rankin, D., Weinberg, F., and Carleton, F., 2006, "Maximizing Ion-Driven Gas Flows," J. Electrostat., 64(6), pp. 368–376.
[8] Léger, L., Moreau, E., and Touchard, G. G., 2002, "Effect of a DC Corona Electrical Discharge on the Airflow Along a Flate Plate," IEEE Trans. Ind. Appl., 38(6), pp. 1478–1485.
[9] Léger, L., Moreau, E., and Touchard, G. G., 2002, "Electrohydrodynamic Airflow Control Along a Flat Plate by a DC Surface Corona Discharge—Velocity Profile and Wall Pressure Measurements," AIAA Paper No. 2002-2833.
[10] Matsuno, T., Ota, K., Kanatani, T., and Kawazoe, H., 2010, "Parameter Design Optimization of Plasma Actuator Configuration for Separation Control," AIAA Paper No. 2010-4983.
[11] Corke, T. C., and Post, M. L., 2005, "Overview of Plasma Flow Control: Concepts, Optimization, and Applications," AIAA Paper No. 2005-563.
[12] Takashima, K., Zuzeek, Y., Lempert, W. R., and Adamovich, I. V., 2010, "Characterization of a Surface Dielectric Barrier Discharge Plasma Sustained by Repetitive Nanosecond Pulses," AIAA Paper No. 2010-4764.
[13] Jukes, T. N., and Choi, K., 2009, "Flow Control Around a Circular Cylinder Using Pulsed Dielectric Barrier Discharge Surface Plasma," Phys. Fluids, 21(8), p. 084103.
[14] Nishihara, M., Takashima, K., Rich, J. W., and Adamovich, I. V., 2011, "Mach 5 Bow Shock Control by a Nanosecond Pulse Surface DBD," AIAA Paper No. 2011-1144.
[15] Golub, V. V., Son, E. E., Saveliev, A. S., Sechenov, V. A., and Tereshonok, D. V., 2011, "Investigation of Vortex Structure Near the Surface of DBD-Actuator," AIAA Paper No. 2011-154.
[16] Tkacik, P. T., 1980, "Cascade Perfomance of Double Circular Arc Compressor Blades at High Angles of Attack," Master's thesis, Virginia Tech, Blacksburg, VA.
[17] Gregory, J. W., Porter, C. O., and McLaughlin, T. E., 2008, "Circular Cylinder Wake Control Using Spatially Distributed Plasma Forcing," AIAA Paper No. 2008-4198.
[18] Mertz, B. E., and Corke, T. C., 2011, "Single-Dielectric Barrier Discharge Plasma Actuator Modelling and Validation," J. Fluid Mech., 669(2), pp. 557–583.
[19] Durscher, R., and Roy, S., 2011, "Induced Flow From Serpentine Plasma Actuators Acting in Quiescent Air," AIAA Paper No. 2011-957.
[20] Wang, C. C., and Roy, S., 2011, "Geometry Effects of Dielectric Barrier Discharge on a Flat Surface," AIAA Paper No. 2011-732.
[21] Moreau, E., Sosa, R., and Artana, G., 2008, "Electric Wind Produced by Surface Plasma Actuators: A New Dielectric Barrier Discharge Based on a Three-Electrode Geometry," J. Phys. D: Appl. Phys., 41(11), p. 115204.